NORTHWESTERN UNIVERSITY

Harnessing Nonlinearity and Asymmetry for Built-in Control in Mechanical and Fluid Systems

A DISSERTATION

SUBMITTED TO THE GRADUATE SCHOOL

IN PARTIAL FULFILLMENT OF THE REQUIREMENTS

for the degree

DOCTOR OF PHILOSOPHY

Field of Physics

By

Daniel J. Case

EVANSTON, ILLINOIS

September 2019

ABSTRACT

Harnessing Nonlinearity and Asymmetry for Built-in Control in Mechanical and Fluid Systems

Daniel J. Case

Nonlinear systems with many interacting components often exhibit behaviors that cannot be anticipated, even in principle, by only knowing the properties of the constituent parts and thereby emerge as a result of interactions between the parts. Examples of such systems range from power grids and financial markets to food networks and physical materials. Beyond merely understanding the emergent properties of these systems lie the dual goals of developing strategies to control them as well as designing new systems that manifest pre-specified behaviors. In this thesis, we focus on both of these goals. First, we develop an approach for designing microfluidic networks that exhibit an array of programmable flow behaviors. Flows through microfluidic systems typically respond linearly to pressure changes, which hinders the ability to implement built-in flow control mechanisms and results in their dependence on external control devices (e.g., computer-operated pumps). We design microfluidic networks that exhibit a nonlinear relation between the flow rate and applied driving pressure and demonstrate how an array of useful dynamics, such as flow rate oscillations, switching, bistability, and signal amplification may be systematically implemented into larger networks. In another context of

harnessing nonlinear effects in a fluid system, we present a new form of dynamical levitation of heavy particles. In this scenario, particles much denser than the fluid can be captured by interacting vortices and, remarkably, be carried against the direction of both the flow and gravity.

As a second part of this thesis, we propose new roles for introducing asymmetry into a system. We show new instantiations of the general phenomenon asymmetry-induced symmetry, whereby the stability of the symmetric state(s) of a system is reliant on an asymmetric structure of the system. Specifically, we demonstrate how instabilities that arise in classic mechanical and fluid systems by way of spontaneous symmetry breaking events may be avoided through the systematic introduction of physical system asymmetries. The two particular contexts we consider are optimizing the shape of a column to increase its maximum supported load and suppressing the formation of waves on the surface of a vibrated fluid (i.e., Faraday waves).

The results of this thesis present a framework in which systems are designed to exhibit targeted dynamics that arise as emergent phenomena and, thus, provide a new approach for the design of built-in control mechanisms.

Acknowledgements

I wish to thank the many people that made significant contributions to the work presented in this thesis. First and foremost, I am grateful for the time and attention my advisor, Prof. Adilson Motter, provided to me throughout my time as a graduate student. Without his guidance and ideas, I would not have had the opportunity to pursue the variety of intriguing scientific questions explored here. I also give great thanks to Prof. Jean-Régis Angilella, who provided to me critically important technical training and guidance in fluid dynamics, starting in my first year of graduate school and continuing throughout. I also thank Prof. István Kiss and Yifan Liu at Saint Louis University, who performed extensive experimental work as part of a fantastic long-term collaboration. In addition, I express my great thanks to our other collaborators: Zachary Nicolaou, Ernest van der Wee, and Prof. Michelle Driscoll. I give special thanks to Erisa Apantaku for providing substantial administrative support over the last several years. Finally, I am grateful for the contributions of my thesis committee: Profs. Adilson Motter, Erik Luijten, Monica Olvera de la Cruz, Michelle Driscoll, and Michael Schmitt. Their combined scientific expertise was critical for the evaluation of the results in this thesis.

The work presented here was supported by the National Science Foundation, the U.S. Army Research Office, and Northwestern University through a Presidential Fellowship. I am thankful to each of these institutions for providing to me the opportunity to perform this research.

Table of Contents

List of Tables

List of Figures

CHAPTER 1

Introduction

Systems that are composed of many individual parts and exhibit behavior that depends critically on the nature of the interactions between the parts are generally referred to as complex systems. Research that falls under the umbrella of complex systems spans the disciplines of sociology and economics to biology and physics. Such research is not necessarily connected through the shared study of the same systems or even a common set of analytic tools. Rather, there exists a mutual appreciation for emergent phenomena across systems of different origin and scale. Classes of systems that have traditionally garnered attention from complex systems researchers include social networks, ecosystems, urban infrastructure, and physical or biological materials [**1, 2**]. While it may seem from this description that almost all topics of study could be classified as complex systems, the field was not generally recognized until the mid to late 20th century. Its emergence marked a transition from the reductionist approach to science (or thinking) to an approach in which it is recognized that entirely new, unanticipated behaviors emerge when elementary units are aggregated.

The stable structures of large biomolecules [**3**], cascading failures in financial markets or electric power grids [**4**], synchronization among coupled oscillators [**5**], and pattern formation in uniformly driven homogenous system [**6**] are all examples of emergent properties that arise in complex systems. A common source of these properties is nonlinear effects in the systems. The dynamics of individual units of a system may be nonlinear as well as the interactions between units. The presence of nonlinearity has the dual effect of greatly increasing the possible states

of a system and amplifying perturbations to a system. Indeed, much work has been done in understanding the impactful dynamics and state transitions in critical systems, such as cascading failures [**7, 8**], which often arise from relatively small initial perturbations. Another surprising effect of nonlinearity is spontaneous ordering or self-organization, as observed, for example, through emergent patterns or synchronization in the dynamics of individual units throughout a system [**9, 10**].

The research ideas and results in this thesis were both conceived and developed within the framework of complex systems. A major theme of this work is exploiting emergent behaviors as a mechanism of built-in control in a system. We focus not only on understanding the behavior of a system, but also on how systems may be designed to exhibit desired behaviors. Rather than designing the control input to stimulate a system to behave in a specific way, as done in classical control approaches, the targeted behavior instead arises inherently. The first class of systems for which we develop this approach is microfluidic networks.

Microfluidics typically encompasses the study of fluid behavior when the working volume of the fluid is on the order of nanoliters and the characteristic length scale is ten to one-hundred microns [**11**]. Microfluidics is distinguished from the study of fluids at the macroscopic scale primarily because fluids behave very differently when confined to small volumes than what our intuition leads us to expect from our everyday experiences, such as water coming from a faucet. This behavioral change results from a scaling effect and is predicted from the Navier-Stokes equations, which generally describe fluid motion [**12**]. In practice, microfluidics typically refers to miniaturized networks of channels that transport and process fluids. The channels generally have a width on the order of 10-1000 microns and the entire network is embedded within a polymer chip a few centimeters in width. Ever since the invention of microfluidic systems,

the potential of the technology has been recognized, and yet, a major theme of contemporary microfluidics literature is that this potential has still not been fully realized [**13, 14, 15**]. Microfluidics have promising applications across the fields of physics, chemistry, biology, and medicine – given that they can be used to isolate systems within a microenvironment with the added benefit of being able to actively manipulate that environment. Examples of such applications include trapping single cells within different media, precisely combining small quantities of chemical reagents, investigating the effects of drug candidates on different cell types, and performing point-of-care diagnostic testing [**16**].

A common property of microfluidic systems is that the flows through the channels are laminar — viscous damping typically dominates fluid inertia effects. Therefore, many of the nonlinear behaviors commonly associated with fluids, like turbulence, are not present in microfluidics. The advantage of this simplified behavior is that flows through microfluidic networks are predictable and easily modeled in similar fashion to currents in electronic circuits [**17, 18**]. However, the lack of nonlinear effects leads to the reliance of microfluidics on external control devices in order to produce complex flow patterns in the network. For example, simple control capabilities, such as switching the direction of flow through specific channels or amplifying changes in flow rates, generally require actuation from multiple external pumps, which are themselves operated by computers. This dependence on external devices much larger than the microfluidic network itself, thus, inhibits the potential scalability and portability of the technology [**19, 15**].

Efforts to develop built-in flow control mechanisms in microfluidics have been on-going over the past 20 years. The most common approach is to construct microfluidic networks from flexible materials that deform under pressure [**20, 21, 22, 23**]. Then, nonlinear fluid-structure

interactions are utilized as flow control mechanisms. Generally, two partially over-lapping networks separated by a thin membrane are used. One network transports the working fluid, while the other is pressurized with air, which deflects the membrane and manipulates the working fluid flow. Nonetheless, these networks still rely on external actuation of the control layer network and have other drawbacks originating from the flexible materials used. These materials: i) have high variability in their stiffness, and thus networks are difficult to replicate; ii) cannot withstand high driving pressures; and iii) may not be chemically compatible with the desired working fluid [**13**]. For these reasons, microfluidic systems are still primarily restricted to use in a laboratory setting, which contrasts with the original vision of the 'lab-on-a-chip' technology.

In this thesis, we first demonstrate a new way of designing microfluidic networks with built-in flow control mechanisms that do not rely on external actuation nor on flexible components. By recognizing the critical role of nonlinearity in existing control approaches (e.g., nonlinear pump actuation or elastic effects), we develop strategies to enhance nonlinear fluid dynamical effects in laminar flows. We do so by designing the geometry of the network so as to amplify fluid inertia effects, which are the general source of nonlinear behavior in incompressible fluids. We then demonstrate how these nonlinear effects can be harnessed so as to manipulate flows throughout the network. For example, we show how the direction of flow through a pre-specified internal channel in a network can be switched solely by changing the single driving pressure and provide a systematic approach to scaling this behavior to large, complex networks. We also design networks in which bistable flow states emerge and give rise to spontaneous flow rate oscillations, hysteresis, signal amplification, and negative conductance transitions. All of these behaviors directly result from nonlinear fluid mechanical phenomena, which themselves manifest from interactions between flows through different channel segments of the network. In

contrast to the modular design of microfluidics (which is the approach used for microelectronic circuits), our work illustrates how desired behaviors can emerge in the dynamics of the system as a whole.

We also establish a fluid analog of Braess's paradox in microfluidic networks. Braess's paradox is an apparent paradox first discovered in the context of traffic networks, in which Dietrich Braess found that under certain conditions traffic flow through a network of roads can be increased by, counter-intuitively, removing specific roads in the network [**24, 25**]. Since then, this phenomenon has been realized in real traffic grids, and analogs of it have been found in economic, electronic, and mechanical systems [**26, 27, 28, 29**]. Here, we show that the flow rate driven through a microfluidic network by a fixed pressure difference can be increased by removing a channel from the network. This behavior arises as a direct consequence of the nonlinear fluid mechanical effects mentioned above. Although instantiations of Braess's paradox in fluid networks have been previously suggested [**30, 31**], we show the first realization supported by the combination of theory, simulations, and direct experiments.

In another context of harnessing nonlinear dynamics in a fluid system, we present a new form of particle levitation. Generally speaking, particles that are denser than a fluid move in the direction gravity or in the general direction of the fluid flow. We discover a system in which heavy particles that are 10–1000 times denser than the fluid may be levitated against both the force of gravity and the direction of the flow. In this new form of fluid dynamical levitation, the dynamics of interacting vortices can trap particles within the fluid and transport them in any direction. This behavior arises as a result of the nonlinear interaction between the vortices as well as the nonlinear motion of the particles in the flow. The particles have finite size and mass and therefore behave as inertial particles in that they do not necessarily follow the streamlines of

the flow [**32**], which facilitates the capture of the particles by the vortices. Indeed, increasing the gravitational force on the particle has the counter-intuitive effect of increasing the probability of the particle being captured and levitated by the vortices. The discovery of this phenomena may be used to understand the transport of ocean sediment and sea sprays as well as have potential application in industrial filtering processes.

The research topics discussed thus far have focused on exploiting nonlinear effects to design systems that exhibit specific behaviors. As another part of this thesis, we investigate how the symmetry of a system can also be manipulated to induce desired properties. This work is inspired by the phenomenon of asymmetry-induced symmetry (AIS), which was first characterized in the Motter research group in 2016 [**33**]. A system is said to exhibit AIS if the structure of the system that stabilizes the system state (i.e., dynamics), must have less symmetry than that of the state. In other words, the symmetric state of a system is only stable if the system structure is asymmetric. The context AIS was first formulated in was coupled oscillator networks, in which the synchronized state of the system (i.e., symmetric dynamics of all oscillators) of symmetrically coupled oscillators was only stable if each oscillator had different internal parameters [**34, 35, 36**].

Another way to view AIS is as the converse of spontaneous symmetry breaking. Spontaneous symmetry breaking events underlie a vast array of phenomena across physics and occur when a system suddenly transitions to a new state that no longer possesses the symmetries of the laws governing the system [**37, 38, 39**]. In other words, the stable solution to the dynamical equations of a system are less symmetric than the equations themselves. Here, we present new scenarios of AIS in continuous systems by demonstrating how spontaneous symmetry breaking events may be avoided (or delayed) by introducing physical system asymmetries. We consider

two classical classes of instabilities: the formation of waves on the surface of a vibrated fluid and the buckling transition of a loaded column.

The formation of waves on the surface of a fluid that undergoes vertical oscillatory driving is a classic example of parametric resonance. Although the fluid system is uniformly driven, at critical amplitude and frequency combinations, the symmetric (i.e., flat surface) state becomes unstable and standing waves with a characteristic wavelength form on the surface of the fluid [**40, 41**]. This is one example of spontaneous symmetry breaking. We show how this instability can be suppressed by altering the substrate of the fluid container. By making the substrate periodic (or random) instead of flat, regions of the driving frequency-amplitude parameter space that were previously unstable become stable. That is, by breaking the symmetric system structure (i.e., using a non-flat substrate) the symmetric flat surface state is stabilized.

A second system that exhibits a classic example of spontaneous symmetry breaking is a loaded column. Columns are structures made to support externally applied loads as well as their own weight. From everyday experience we know that applying too large of a load on a column can cause it to buckle. A cylindrical column is a system with infinite rotational symmetry that experiences uniform compression from external loading. When it buckles, the column transitions to a new state that does not reflect either its initial symmetry or the symmetry of the loading. Thus, buckling is another manifestation of spontaneous symmetry breaking. The maximum load a column can withstand before buckling is the so-called critical buckling load, which is a function of the geometry and material properties of the column. Previous research has shown that for a column of fixed length and volume, the optimal distribution of mass along the column axis is not uniform [**42, 43**]. For example, columns that have clamped endpoints can support larger loads if they are thicker in the center and tapered towards the ends. Here we

explore how reducing the symmetry of the shape of the column cross section can increase the critical buckling load. Under certain constrained conditions, the optimal cross-sectional shape does not possess any rotational symmetries. Therefore, we demonstrate how the symmetric, unbuckled state of the column can be stabilized for previously unstable loads by systematically introducing asymmetry into the column structure. Finally, we show how this mechanism of AIS may be exploited in natural structures in the context of botanical morphologies.

The structure of this thesis follows that of the introduction. Chapters 2 through 4 focus on microfluidic networks, Chapter 5 presents our results on dynamical particle levitation, and Chapters 6 and 7 describe new findings of AIS in continuous systems. We conclude the thesis in Chapter 8 with an outlook on potential future lines of research inspired by the results presented here.

CHAPTER 2

Braess's paradox and programmable behavior in microfluidic networks

Microfluidic systems are now being designed with precision to execute increasingly complex tasks. However, their operation often requires numerous external control devices due to the typically linear nature of microscale flows, which has hampered the development of integrated control mechanisms. We address this difficulty by designing microfluidic networks that exhibit a nonlinear relation between applied pressure and flow rate, which can be harnessed to switch the direction of internal flows solely by manipulating input/output pressures. We show that these networks exhibit an experimentally-supported fluid analog of Braess's paradox, in which closing an intermediate channel results in a higher, rather than lower, total flow rate. The harnessed behavior is scalable and can be used to implement flow routing with multiple switches. These findings have the potential to advance development of built-in control mechanisms in microfluidic networks, thereby facilitating the creation of portable systems that may one day be as controllable as microelectronic circuits. This research was conducted in collaboration with Yifan Liu, Jean-Régis Angilella, István Kiss, and Adilson E. Motter [**44**].

2.1. Motivation

Microfluidics' promise to operate as autonomous microscale networks where fluids can be transported, mixed, reacted, separated, and processed is no longer limited by experimental fabrication challenges but instead by difficulties to create built-in controls [**45, 19, 18**]. The development of the modern microelectronics that form the basis of computer microprocessors was

ultimately determined by the creation of integrated circuits, with all components fabricated on the same substrate. Microfluidics have already reached a level of integration in which networks with thousands of components, including control devices, are built on a single compact chip. However, in contrast with electronic integrated circuits, existing on-chip fluid control devices still need to be actuated externally. For example, microfluidic circuits fabricated from flexible polydimethylsiloxane (PDMS) can now incorporate a large number of control valves, which nevertheless have to be operated using a control fluid through a control layer that lays on top of the working fluid network [**21, 46**]. As a result, microfluidics are still predominantly controlled by external hardware despite significant efforts over the past twenty years to develop systems with new control schemes [**23, 47, 48, 49, 50**]. The construction of systems that forgo the current reliance on external hardware is crucial to further the development of portable microfluidic systems for pressing applications, ranging from point-of-care diagnostics and health monitoring wearables to analysis kits for field research [**51, 52, 53, 16**]. To achieve this goal, we need to develop next-generation integrated circuits in which not only the control devices but also the operation of those devices is integrated on-chip. The development of such a level of integration has been fundamentally limited by the fact that, at the microscale, fluid flows tend to respond linearly to pressure changes and thus cannot be easily amplified or switched.

Here, we explore new physics that emerges by combining network theory and fluid mechanics to induce nonlinear behavior in microfluidics and effectively create a passive two-terminal flow-switch device that is entirely operated on-chip, directly by the working fluid. Previous work that has achieved built-in control capabilities (often externally actuated), including oscillatory flows [**22, 14, 54, 55**] and flow rate regulation [**56, 57**], generally relied on flexible membranes and surfaces. Microfluidics with such flexible components require flows with very

low Reynolds numbers—a regime in which the fluid inertia, and thus the only nonlinear term of the Navier-Stokes equation for incompressible fluids, becomes negligible. This has led researchers to often discount the potential effects of fluid inertia on the flows (as reviewed, for example, in Refs. [**58, 11**]). Recent work has shown, however, that inertial forces can serve as a powerful on-chip tool to manipulate microfluidic dynamics *locally* [**59, 60**], including shaping streamlines [**61, 62**], mixing fluids [**63**], and directing particles [**64, 65**]. Here, we present a built-in mechanism to direct flows that: i) does not require any flexible components, and is thus suitable for flows at moderate Reynolds numbers (at which fluid inertia is non-negligible); ii) is designed to amplify inertial effects by incorporating properties of porous media; iii) can be used for *non-local* fluid routing and manipulation of output patterns. Our construction is suitable for implementation using rigid materials because the system-level response to input/output pressures can be programmed into the network structure by combining fluid inertia effects with network design.

Figure 2.1a shows a schematic representation of a microfluidic system with the fundamental network structure we consider. It consists of five segments arranged as two parallel channels connected by a linking channel, where the inlets are kept at a common pressure P_{in} and the outlets are held at a common lower pressure P_{out}. One of the outlet channels is modified to generate a nonlinear pressure-flow relationship, which is achieved by introducing an array of cylindrical obstacles. Our principal results are supported by theory, simulations, and experiments, and they show that we can: 1) induce a flow direction *switch* through the linking channel solely by varying the pressure difference between the inlets and outlets; 2) identify a pressure difference above which the total flow between the inlets and outlets *increases* upon closing the linking channel; 3) predict a *negative conductance* transition in the system when the linking channel is equipped

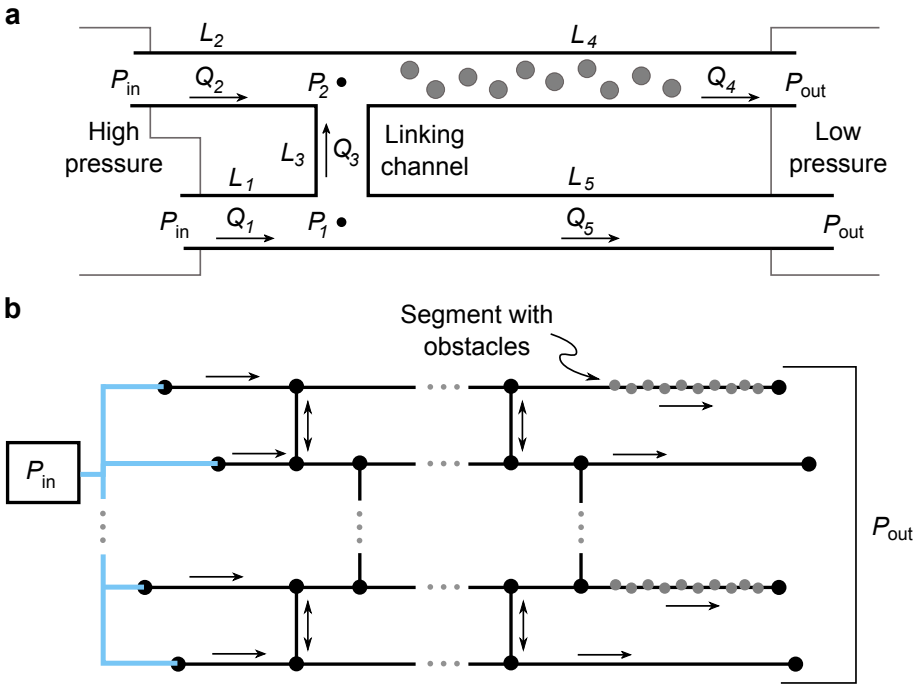

Figure 2.1. **Microfluidic system schematics. a**, Microfluidic network consisting of two parallel channels, joined by a linking channel, that connect high- and low-pressure fluid reservoirs. Solid gray circles represent stationary cylindrical obstacles. The labels denote pressures (P), channel lengths (L), and flow rates (Q), with arrows indicating the positive flow direction. **b**, Generic multiswitch microfluidic network consisting of an array of parallel channels interconnected by multiple linking channels. A subset of channel segments contain cylindrical obstacles. Flow is driven through the network by a single pressure difference ($P_{\text{in}} - P_{\text{out}}$).

with an offset fluidic diode. For the behavior described in (3), an increase (decrease) in pressure leads to a discontinuous decrease (increase) in the flow rate between terminals, which is a property that has been sought using flexible diaphragm valves [**66**] and is analogous to negative compressibility transitions previously observed in certain classes of engineered materials [**28**]. The counter-intuitive behavior described in (2), on the other hand, is formally equivalent to the so-called Braess paradox originally established for traffic networks [**24, 25**], where closing a shortcut road has the possible effect of increasing net traffic flow. Our system can be interpreted

as a passive device, in which the flow switch described in (1) is controlled through pressures on the working fluid itself, thereby facilitating integration. We demonstrate such integration by considering larger microfluidic networks, as illustrated in Fig. 2.1b, which incorporate multiple linking channels and are thus capable of exhibiting multiple flow switches. Flows through these networks are driven by a single pressure difference and yet can be designed to exhibit a variety of flow states by programming the pressure at which each flow switch occurs. We consider a network with multiple flow switches to be programmable if the channel dimensions can be chosen so that each individual flow switch occurs at a predefined driving pressure.

2.2. System design and nonlinearity

We consider conditions under which all channel segments have the same width w, the working fluid is water, and all surfaces (including obstacles) have no-slip boundaries. We assume, without loss of generality, that the pressure P_{out} at the outlets is zero, and consider two conditions for the driving pressure P_{in} at the system inlets. Under one condition, total pressure is controlled and the two inlets open directly into the high-pressure reservoir. Under the other condition, static pressure is controlled and the inlets are connected to the reservoir by pressure regulators. Total pressure is the sum of static pressure and dynamic pressure, where dynamic pressure is defined as $\frac{1}{2}\rho v^2$ for a fluid with density ρ and velocity v. The distinction between these boundary conditions is often neglected in the microfluidics literature when the Reynolds number is less than one [**17**], but it can become important for larger Reynolds numbers (even though the flow remains laminar) [**67**]. We examine two network configurations of the system in Fig. 2.1a: the *connected configuration*, in which the two parallel channels are allowed to exchange fluid through the linking channel; and the *disconnected configuration*, in which the

linking channel is closed or removed. In our theoretical analysis and simulations, the flows are assumed to be two dimensional, yet the main results carry over to three dimensions, as verified in our experiments.

For a straight microfluidic channel, with no obstacles, of length $L \gg w$, a plane Poiseuille flow is an excellent approximation to the steady-state solution of the Navier-Stokes equations in two dimensions. The Poiseuille flow yields a linear relation between the total volumetric flow rate per unit depth Q and the pressure drop ΔP along the channel,

$$-\Delta P = \frac{12\mu L}{w^3} Q, \tag{2.1}$$

where μ is the dynamic viscosity of the fluid. To induce deviations from this linear regime, we consider the effect of introducing multiple stationary obstacles in the channel. Figure 2.2a,b shows simulations of the Navier-Stokes equations for a channel with ten cylindrical obstacles of radius $r = w/5$ placed non-uniformly and separated by a distance of approximately $6r$ (Appendix A). We observe recirculation regions forming near the obstacles for sufficiently large Reynolds number $Re \equiv 2\rho Q/\mu$. No unsteady flow due to vortex shedding is observed for Re of up to 400, as expected for systems with highly confined obstacles [**68**]. The recirculation regions first appear for Re of order 10 and their number and size depend on Re. These localized structures are hallmarks of fluid inertia effects (and thereby of nonlinearity). We investigate how fluid inertia effects compound to impact the total flow rate by performing simulations across moderate values of Re when different numbers of obstacles are present. We find that a nonlinear relation between the pressure drop ΔP and flow rate $Q = \mu Re/2\rho$ emerges as soon as obstacles are introduced and that the nonlinearity becomes more pronounced as the number of obstacles is increased (further details provided in section 3.4 and Fig. 3.6a).

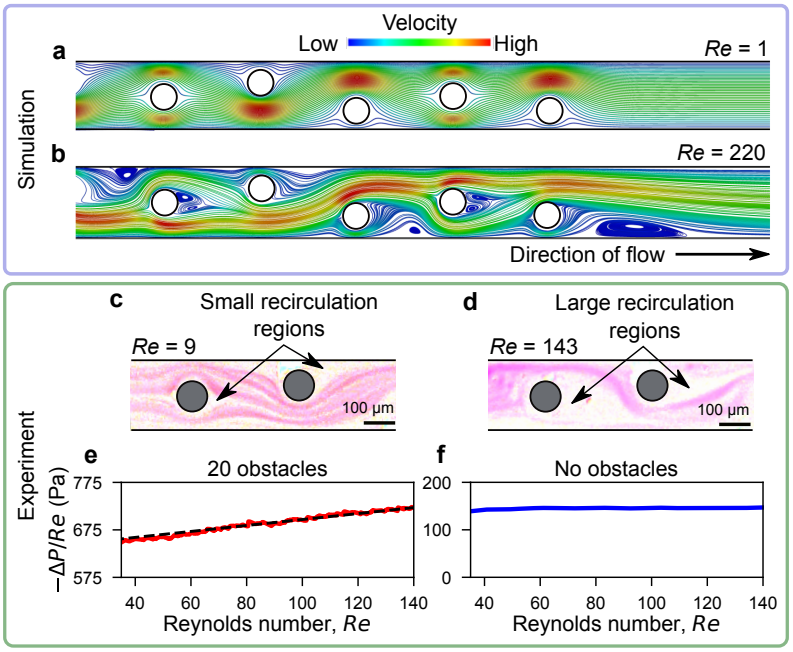

Figure 2.2. **Development of nonlinear flow. a**, **b**, Simulated flow in a channel with obstacles (white circles), showing no recirculation for low Re (**a**) and significant recirculation near the obstacles for larger Re (**b**). **c**, **d**, Experimentally observed flows around the obstacles (grey circles), visualized using pictures of fluorescent particles (shown in pink). The particle tracks trace the underlying flow structure, confirming the development of recirculation regions (white areas) as Re is increased from low (**c**) to moderate values (**d**). **e**, **f**, Experimentally measured relation between pressure loss and Re for a channel with (**e**, red curve) and without (**f**, blue curve) obstacles. The dashed line in **e** is a reference to guide the eye and indicates an approximately quadratic relation between pressure loss and flow rate.

The nonlinearity we observe in the relation between ΔP and Q conforms to the well-known Forchheimer effect in porous media, which characterizes flow through many interconnected microchannels where local inertial effects at the points of interconnection are non-negligible, even for creeping flow [**69, 70, 71**]. This relation takes the form $-\Delta P = \alpha\mu LV + \beta\rho LV^2$, where α is the reciprocal permeability and β is the non-Darcy flow coefficient, both depending solely on the system geometry, and V is the average fluid velocity. In two dimensions, $V =$

Q/w and the Forchheimer equation can be written as

$$-\Delta P = \frac{\alpha\mu^2 L}{2\rho w} Re + \frac{\beta\mu^2 L}{4\rho w^2} Re^2. \tag{2.2}$$

Porous-like structures have been used both to study non-inertial effects in microfluidics, such as droplet formation [**72**] and viscous fingering [**73**], and to study inertial effects in larger systems [**74**]. It is interesting that, in our system, inertial effects arise at the microfluidic scale even for a much smaller number of obstacles than the typical number in porous-like materials. Indeed, in agreement with the nonlinear relation in equation (2.2), we find an excellent linear fit between $-\Delta P/Re$ and Re for a channel with ten obstacles, and we validate the fit by predicting flows through the same channel for a fluid with a different viscosity (further details provided in section 3.4 and Fig. 3.6b).

The physical mechanism giving rise to this nonlinearity is the increase in flow recirculation and velocity gradients for larger Re, as evidenced in Fig. 2.2a,b for $Re = 1$ and 220. To test the impact of the inertial effects in realistic systems, we perform experiments using microchannels fabricated from stiff PDMS (hardened by curing), which were designed to have approximately square cross-sections to minimize deformation (Appendix A). Figure 2.2c,d shows experimental evidence of the increase in the number and size of the recirculation regions with Re, in agreement with our simulations. An approximately linear relation between $-\Delta P/Re$ and Re and thus an approximately quadratic relation between $-\Delta P$ and Q for a channel containing twenty obstacles is shown in Fig. 2.2e, which contrasts with the constant relation measured for a channel without obstacles in Fig. 2.2f. Through additional experiments we confirmed that

similar relations hold for channels constructed from materials with both higher rigidity (SU-8 photoresist) and lower rigidity (Flexdym) than the stiff PDMS (further details provided in section 3.6 and Fig. 3.8).

2.3. Switching and Braess's paradox

We incorporate the channel segment with obstacles characterized above into a network by considering the microfluidic system presented in Fig. 2.1a. We take the common static pressure P_{in} at the inlets to be the controlled variable in the system. The total flow rate through the network is now simply the sum of the flows at the outlets ($Q_4 + Q_5$). In Fig. 2.3, we present results for this system from direct simulations of the steady-state solutions of the Navier-Stokes equations. As P_{in} is increased from zero, the flow rate through the linking channel Q_3 is initially positive before changing direction and becoming negative once a critical pressure, defined as P_{in}^*, is reached (Fig. 2.3a). This flow switch results from the nonlinear change in pressure loss along the channel segment containing obstacles, which causes a change in the sign of the pressure difference along the linking channel ΔP_{21} (approximately $P_2 - P_1$) as the flow rate through the system increases with P_{in}. We define Q_C to be the total flow rate for the connected system configuration and Q_D to be the total flow rate for the disconnected system configuration, where both are regarded as functions of P_{in}. All data in Fig. 2.3a is expressed as a percentage of Q_C.

Figure 2.3a shows $\Delta\mathcal{Q} \equiv Q_C - Q_D$ for a range of applied pressures P_{in}. Intuition may suggest that $\Delta\mathcal{Q}$ is positive for all values of P_{in} because the linking channel in the disconnected system can be considered to have an infinite fluidic resistance, while for the connected system configuration the resistance of the linking channel is finite. Hence, reducing the resistance of

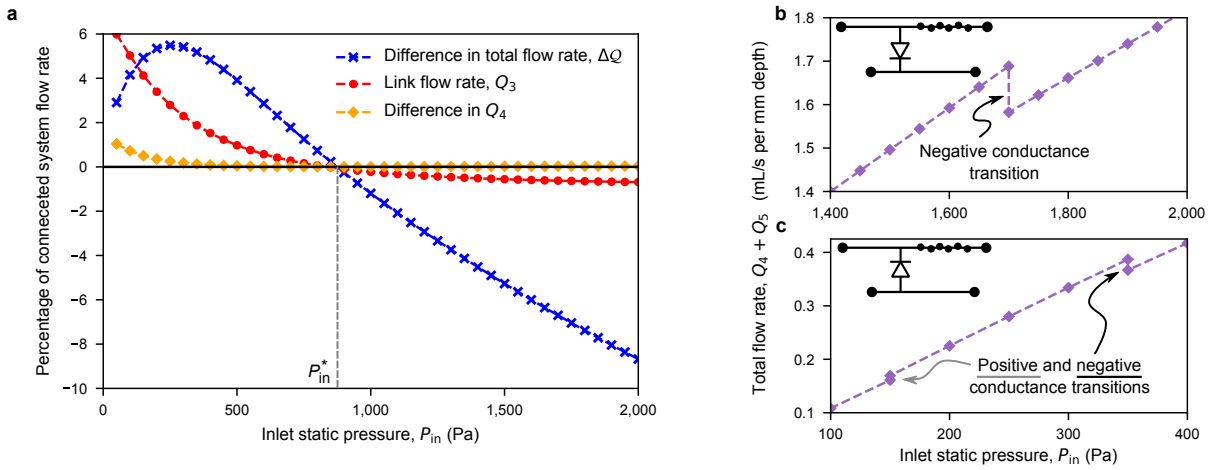

Figure 2.3. **Braess's paradox, flow switch, and negative conductance transitions.** **a**, Simulation results for the connected and disconnected configurations of the system for a range of inlet pressures P_{in}. The flow rates are presented as a percentage of the total flow rate through the connected system, Q_C, where we adopt the sign convention for the flow directions as defined in Fig. 2.1a. The flow through the linking channel switches direction at the critical pressure $P_{\text{in}} = P^*_{\text{in}}$, which coincides with the onset of negative $\Delta\mathcal{Q}$ that marks the occurrence of Braess's paradox. **b**, **c**, Simulation results for the system with an offset fluidic diode incorporated into the linking channel, where the polarity of the diode is indicated in the inset network schematics. As the pressure ΔP_{21} passes a threshold value (positive in **b** and negative in **c**), the system passively transitions from the connected to the disconnected configuration. For one polarity of the diode, this results in a negative conductance transition for $P_{\text{in}} > P^*_{\text{in}}$ (**b**), whereas for the opposite polarity it results in a positive and a negative conductance transition for $P_{\text{in}} < P^*_{\text{in}}$ (**c**).

any component of the system may seem to imply that the total flow rate should increase for fixed P_{in}. We observe, however, that $\Delta\mathcal{Q}$ becomes negative for P_{in} above the critical pressure that marks the flow switch, P^*_{in}, meaning that an open linking channel between the parallel channels results in a *lower* total flow rate. Figure 2.3a also shows that the flow rate through the channel segment with obstacles, Q_4, remains largely unchanged between the two configurations. Therefore, the difference in the total flow rate exists primarily in the difference in Q_5, and Q_3 acts as a controlling variable of Q_5.

The observation of a lower total flow rate for the connected configuration compared to the disconnected configuration for fixed P_{in} is a manifestation of a fluid analog of Braess's paradox. Indeed, if we consider the disconnected system driven by an inlet pressure $P_{\text{in}} > P_{\text{in}}^*$, the addition of the linking channel can result in a significant *decrease* in the total steady-state flow rate (as large as 10% in our simulations). The value of the critical pressure P_{in}^* depends, of course, on the dimensions of the channels, but we find that the onset of Braess's paradox and the flow switch always occur at the same pressure for the range of parameters investigated. We obtain similar results for Braess's paradox and flow switching when instead the total pressure is controlled at the inlets (further details provided in section 3.3).

Our observation of Braess's paradox and flow switching has the potential to lead to additional control features when existing microfluidic components are integrated into our system. For example, consider an offset fluidic diode [**75**], which can be idealized as closed for pressure differences below a predefined threshold and open above the threshold. Figure 2.3b,c shows results from simulations that incorporate one such diode with each of the two polarizations into the linking channel, where the state of the diode (open/closed) is governed by the pressure difference ΔP_{21}. In both cases, controlling the driving pressure can induce negative fluidic conductance transitions, where an *increase* in P_{in} leads to an abrupt *decrease* in the total flow rate (and a decrease in P_{in} leads to an abrupt increase in flow rate). A negative conductance transition is predicted for any positive diode threshold (Fig. 2.3b) and another one is predicted for a negative diode threshold between zero and the observed minimum of ΔP_{21} (Fig. 2.3c). In the latter case, a small positive conductance transition is also predicted, which follows from the non-monotonic behavior of the flow rate Q_3 (and thus of ΔP_{21}); the flow rate Q_3 initially increases and then decreases (i.e., ΔP_{21} passes through a minimum) as P_{in} is increased from

0 to P_{in}^{*} (Fig. 3.3). Note that the pressure difference ΔP_{21}, and thus the opening and closing of the diode, is indirectly controlled by varying P_{in}. These transitions can be seen as a consequence of flow switching and Braess's paradox, in which the transition from the connected to the disconnected configuration is passive.

2.4. Experimental results

We performed experiments to validate our predictions of flow switching and Braess's paradox in a network with dimensions typical of microfluidics. A schematic of the experimental apparatus is presented in Fig. 2.4a, where an open/close valve is used to implement the addition/removal of the linking channel (Appendix A). To visualize the switch in flow direction through the linking channel, we drive red- and blue-dyed water into the two inlets using a common pressure source. With the valve open, a flow switch is observed at a critical driving pressure P_{in}^{*} in the range of 5–10 kPa, as demonstrated in Fig. 2.4a by images of the flows through the channel junctions at the end points of this pressure range. (The switching behavior has no reliance on the valve, as explicitly shown in Fig. 3.9, but this setup is convenient for allowing us to study flow switching and Braess's paradox using the same chip.)

A confirmation of Braess's paradox in this system is shown in Fig. 2.4b for driving pressures above P_{in}^{*}, as observed in our simulations. The measured total flow rate is higher when the linking channel valve is closed than when it is open, thus demonstrating the paradox, and the magnitude of the paradox is observed to be larger for higher driving pressures. A break down of how the flow rate changes in channel segments 4 and 5 individually is shown in Fig. 2.4c,d. Closing the valve causes the flow rates through both channels to increase, which is in agreement with direct simulations and is yet another striking aspect of Braess's paradox in this system,

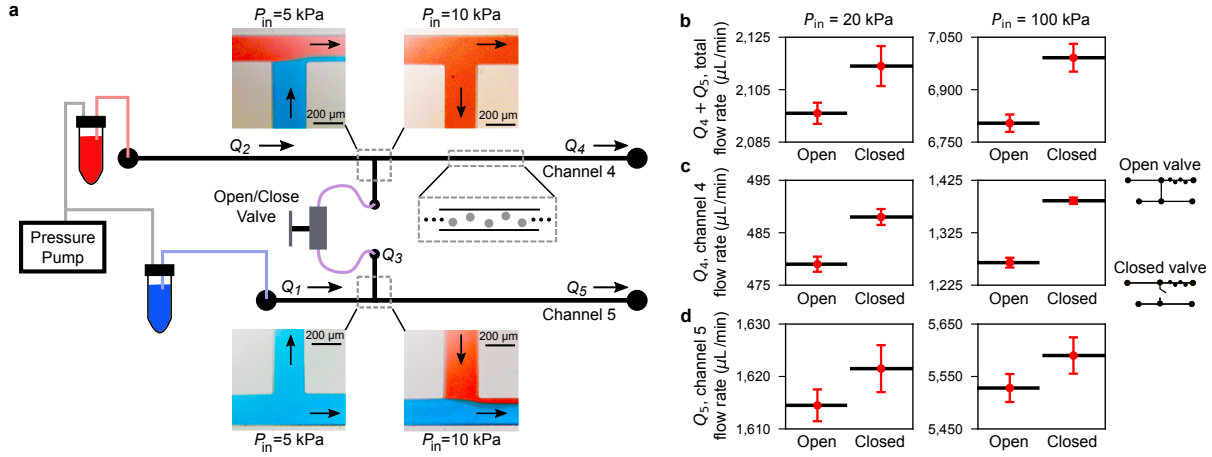

Figure 2.4. **Experimental observation of flow switch and Braess's paradox.** **a**, Experimental setup of the system presented in Fig. 2.1a and flow tracking images at the junctions. An air-pressure pump is used to equally pressurize two vials containing red and blue dyed water, respectively, where each vial is connected to one of the system inlets. The linking channel is equipped with an open/close valve and channel 4 contains 20 obstacles. Images of the dyed flows through the junctions are shown for P_{in} below (5 kPa) and above (10 kPa) the flow switching pressure P^*_{in}, where the flow directions are indicated by the arrows. **b**, Total flow rate ($Q_4 + Q_5$) when the linking channel valve is "Open" and "Closed" for two different driving pressures above P^*_{in}. **c**, **d**, Break down of the total flow rate into Q_4 (**c**) and Q_5 (**d**) for the two states of the valve. The plotted flow rates are averages derived from time series data, and the error bars indicate one standard deviation. The observed increase in the total flow rate when the valve is closed is direct evidence of Braess's paradox.

since it is at first intuitive to expect that Q_5 would decrease when the in-flow from the linking channel is switched off. Time series of the flow rates measured as the linking channel is sequentially opened and closed further illustrate the transitions underlying the paradox (as shown in Fig. 3.10).

Our experiments correspond to scenarios in which the total pressure is controlled at the inlets. The experimental results are in full qualitative agreement with simulations performed under the same pressure boundary conditions (further details provided in section 3.3). This illustrates the robustness of the phenomenon, given that our simulations are in two dimensions

and three-dimensional effects are expected to be significant in the experiments. Thus, our report of Braess's paradox in microfluidic networks is consistently supported by both simulations of the Navier-Stokes equations and direct experiments. We note that different aspects of the paradox have been considered in fluid networks, but only for macroscopic (i.e., non-microfluidic) systems and while modeled by ad hoc flow equations [**30, 76, 31**]. Analogs of the paradox have also been studied in several other areas, including electrical, mechanical, biological, and contemporary traffic networks [**26, 27, 29, 77**]. These examples show that Braess's paradox is a potentially general network phenomenon, which has remained unexplored in microfluidic networks.

2.5. Network model

We now characterize the microfluidic system in Fig. 2.1a with an analytic model that captures the flow properties observed in our simulations and experiments. The model is constructed as follows: (i) we consider the pressure at the inlets P_{in} to be in the vicinity of P_{in}^*; (ii) we approximate the pressure-flow relation through the linking channel as $Q_3 = \kappa(\gamma P_1 - P_2)$, where κ is the channel conductivity and γ is a free parameter allowing for an effective pressure difference; (iii) the flow equation for each other channel segment without obstacles is written as in equation (2.1), where $-\Delta P$ is the pressure drop along the segment and L is the segment length; (iv) for the channel segment with obstacles, we take the flow equation to be in the form of equation (2.2) (with Re expressed as $2\rho Q/\mu$); (v) we include the most dominant term resulting from minor pressure losses at the channel junctions [**78, 79**]. We model the contribution of the latter as an additive term $K(Q_3/Q_1)f(Q_5)$ to the equation of channel segment 5, where the scaling factor f and the coefficient K are increasing functions for $P_{\text{in}} \geq 0$ such that $f(0) = K(0) = 0$.

Therefore, the model consists of five pressure-flow relations, in addition to two flow conservation equations at the junctions: $Q_3 + Q_2 - Q_4 = 0$ and $Q_3 + Q_5 - Q_1 = 0$. When the static pressure is controlled at the inlets, the only nonlinearity that exists in the model comes from the Forchheimer term due to the presence of obstacles and the minor loss term. The model can also be adapted for when total pressure is controlled by taking the static pressure at each inlet to be $P_{\text{in}} - \rho Q^2/2w^2$, where P_{in} now denotes total pressure. However, the dynamic pressure term $\rho Q^2/2w^2$ is often negligible in real microfluidic systems because of the high pressures needed to drive fluid though the channels. Indeed, in our experiments, the dynamic pressure near P_{in}^* was smaller than the static pressure by two orders of magnitude and smaller than the pressure loss due to the Forchheimer effect by one order of magnitude. This can also be seen in Fig. 2.2f, where a constant relation between Re and $\Delta P/Re$ is measured. Details of the model are presented in section 3.1.

Several results are obtained from this model for $P_{\text{in}} > 0$, as assumed here. First, if $\beta = 0$ (i.e., the quadratic term is zero in equation (2.2)) when the static pressure is controlled or the dynamic pressure is negligible, then flow switching does not occur, in agreement with direct simulations (further details provided in section 3.5). Second, when $\beta > 0$, a steady-state solution can be found satisfying $Q_3 = 0$ provided a geometric condition is satisfied, which for $\gamma = 1$ simplifies to

$$L_1 < \frac{12 L_2 L_5}{\alpha w^2 L_4} = L^*. \tag{2.3}$$

This solution identifies the critical pressure P_{in}^*. Third, for flow rates in the linking channel, the model predicts that a variation δQ_3 is negatively related to a variation δP_{in} around P_{in}^*. This indicates that P_{in} above (below) P_{in}^* results in a negative (positive) flow rate through the linking

channel. The first result implies that, in our experiments, the Forchheimer effect is necessary to achieve a flow switch. The second and third results, which hold even for when dynamic pressure is non-negligible, show that this model captures the flow switching behavior observed in the simulations and experiments.

Figure 2.5 shows the model prediction in equation (2.3) validated against direct simulations of the Navier-Stokes equations. The pressure at which the flow switch occurs tends to 0 as L_1/L^* approaches 1 from below, and Q_3 is negative for any positive inlet pressure when $L_1/L^* > 1$. This result is found both when the static (Fig. 2.5a) and when the total (Fig. 2.5b) pressure is controlled and shows that the analytic model agrees quantitatively with our findings above. In predicting the precise pressure at which the flow switch occurs, the conductivity of the linking channel, κ, is inconsequential. However, the prediction is sensitive to the parameter γ. Thus, we treat γ as a fitting parameter to predict the pressure at which the flow switch occurs, as indicated by vertical lines in the figure. The resulting predictions are in excellent agreement with simulations when static pressure is controlled (Fig. 2.5a). The predictions when total pressure is controlled are less accurate (Fig. 2.5b), likely as a result of not including entrance length effects in the model, which would account for the development of the parabolic velocity profile characteristic of a Poiseuille flow.

The model also predicts Braess's paradox as observed in our experiments and simulations. Specifically, under the condition that equation (2.3) is satisfied and dynamic pressure is small (or static pressure is controlled), the model predicts the paradox to occur for $\delta P_{\text{in}} > 0$ if and only if

$$K'(0)\beta f\left(\frac{a}{\beta}\right) > c, \tag{2.4}$$

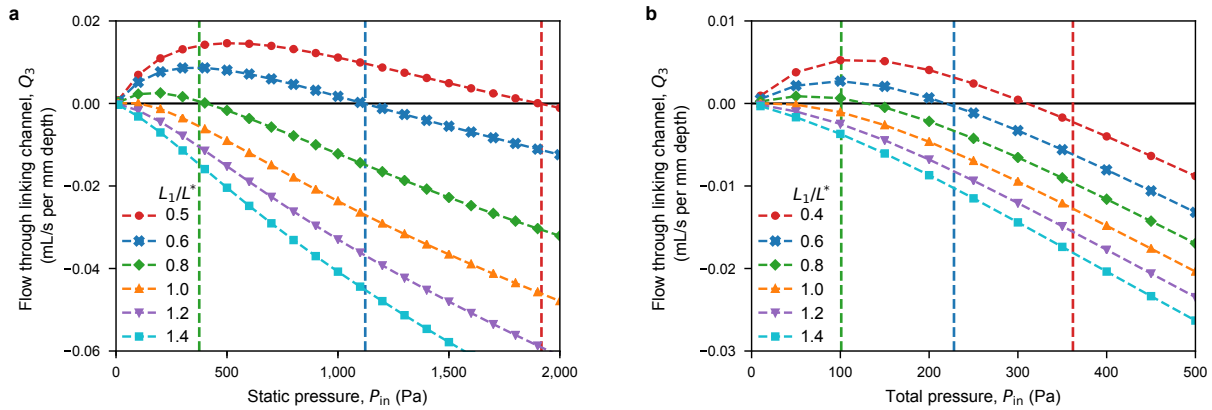

Figure 2.5. **Model prediction of flow switching.** **a**, **b**, Simulated flow rate through the linking channel (symbols) for different values of L_1 when controlling static pressure (**a**) and total pressure (**b**). In agreement with the prediction in equation (2.3), a flow switch occurs only when $L_1/L^* < 1$. The vertical lines indicate the model prediction of P_{in}^* for the curves with corresponding color. The values of the free parameter γ used for the static and total pressure controlled cases are 1.02 and 0.99, respectively.

where a and c are positive parameters and prime denotes derivative. If total pressure is controlled and dynamic pressure terms are included, the paradox is also predicted for $\delta P_{\text{in}} > 0$ provided that a relation similar to equation (2.4) is satisfied (details for both cases are presented in section 3.2). The dependence of condition (2.4) on β and $K'(0)$ underlines the crucial role of nonlinearity and minor losses in giving rise to Braess's paradox in our experiments, and shows in particular that minor losses have to be sufficiently large. Indeed, if the effect of minor losses is neglected, a form of Braess's paradox is still predicted to occur, but only for $\delta P_{\text{in}} < 0$, which is inconsistent with our simulations and experiments; moreover, the predicted relative magnitude of the effect would then be two orders of magnitude smaller than the one we observe in our experiments and simulations (further details provided in section 3.2).

The result in equation (2.4) also highlights a fundamental difference between microfluidic and electronic circuits, namely that minor losses (i.e., significant energy losses associated with

interactions between circuit components) do not have direct analogs in common electronics. Given the central role played by such losses in equation (2.4), we posit that this difference might be the reason why no equivalent of the Braess paradox effect we present has been observed in electronic networks, even though aspects of it have [**26**]. Motivated by this realization, we further investigated the impact of interactions between channel segments by varying the junction angles to show that the paradox can be further enhanced by manipulating the minor losses (further details provided in section 3.3).

2.6. Networks with multiple programmed switches

The system considered thus far can be generalized to create larger microfluidic networks with multiple flow switches. That is, networks with multiple disjoint channel segments in which the flow initially in one direction can be individually "switched" to move in the opposite direction through the manipulation of one driving pressure alone. In our design, the linking channel plays the role of a switch (and can be referred to as such). Figure 2.1b shows the multiswitch generalization of the network in Fig. 2.1a, which incorporates multiple linking channels and a subset of channel segments with obstacles. We experimentally demonstrate an instantiation of a six-switch network that exhibits flow switching in all linking channels (as presented in section 3.8). Multiswitch networks can be designed by extending the network model presented above.

One such network with ten linking channels is presented in Fig. 2.6a. By marking each inlet flow with a different color, we show that a variety of patterns can form in the outlet flows (colored circles in Fig. 2.6). The specific pattern at an outlet depends on the order in which the flow switches occur as P_{in} is varied. The network model for larger systems is constructed

by combining pressure-flow relations for each channel segment with flow rate conservation equations for each junction. For a given set of channel dimensions, the value of P_{in} for which a specific flow switch occurs can be determined through the addition of a constraint to the model that enforces the flow through the corresponding linking channel to be zero. Then, the design of a network for which each flow switch occurs near a target value of P_{in} can be achieved through optimization of a chosen subset of channel segment dimensions. Depending on which dimensions are allowed to be adjusted in the optimization procedure, the desired relative order of the switches can be achieved exactly, and the final set of switching pressures can be very close to the target ones (often $< 5\%$ difference), where the former is expected to be more important in applications. Further details on the design of multiswitch networks are presented in section 3.7.

As illustrated in Fig. 2.6, eleven different internal flow states and seventeen unique color combinations at the outlets are possible for the switching sequence realized in Fig. 2.6b. Figure 2.6c,d shows the agreement between the model predictions of these internal flow states (and thus the corresponding output patterns) and results from direct simulations of the Navier-Stokes equations for the flow rates through the linking channels as P_{in} is varied. This variety of states and outputs is achieved with only three channel segments containing obstacles and is parameterized by a single control variable—the driving pressure P_{in}. Moreover, the switching is implemented solely through the working fluid, which differs from existing approaches that rely on flexible valves and additional control flows [**22**]. Thus, multiswitch networks exhibit several properties exploitable in the design of new controllable microfluidic systems.

More generally, for a multiswitch network with n_c horizontal channels interconnected by n_l linking channels, the number of possible internal flow states is $n_l + 1$ if each linking channel exhibits a flow switch. In addition, the possible number of unique color combinations in

the outlet flows is $n_c(n_c + 1)/2$ if each inlet flow is marked with a different color. All color combinations can be realized over the set of all switching sequences, provided that there exists flow paths allowing mixing of every set of k adjacent colors for k ranging from 1 to n_c. The myriad of states possible in such multiswitch networks underlies their ability to process inputs into multiple outputs and thus to support various applications.

These applications may include implementing different mixing orders of chemical reagents and devising schemes for the parallel generation of mixtures with tunable concentrations. We also expect other functionalities to arise when time-dependent flows are considered in the networks we present. While dynamic flows were not explored here, previous work has demonstrated how other nonlinear interactions can be harnessed in microfluidic networks to produce oscillatory flows and perform on-chip processing [**54, 55**]. In particular, multiswitch networks could be coupled in series with oscillatory pressure and/or flow sources and used, for example, to synthesize complex time-dependent output flow compositions.

2.7. Discussion

The flow switch, negative conductance, and Braess paradox established in this study are all emergent behaviors of common origin resulting from interactions between different parts of the system. The most important interaction takes place between the nonlinear channel and the linking channel. Here, the nonlinearity is directly determined by the fluid inertia effects that give rise to velocity gradients in the obstacle wakes. This nonlinearity, which we model as a Forchheimer effect in a porous media, can be enhanced and manipulated through the placement of obstacles and has the advantage of not being reliant on flexible components, fluid compressibility, or dedicated control flows. However, nonlinearity arising though other physical means,

such as flow-induced deformation of flexible channels [**80, 81**], may also be potentially used to achieve (or enhance) the above phenomena and can be explored using our network model by incorporating alternative nonlinear equations. The onset of Braess's paradox is marked by the flow switching pressure, above which the increased resistance of the nonlinear channel causes the flow to be routed in the negative direction through the linking channel. The negative conductance transition is also determined by (and always possible in the presence of) a continuous switch of flow directions. Thus, these fluid dynamical effects can be harnessed to build flow control mechanisms that are coded into the network structure.

Here, we considered the scenario in which the inlets and the outlets are (separately) held at the same pressure, rendering the network a two-terminal system in all cases, since this is the most stringent scenario for flow manipulation. If a multi-terminal system is configured by allowing the pressures at each of the inlets (and/or outlets) to be varied independently, then the effects we presented may be further enhanced. In this work, we showed how nonlinear channels can be positioned in microfluidic networks to program a series of flow switches that generate multiple flow states. Our results demonstrate an approach for routing and switching in microfluidic networks that only relies on fluid dynamical mechanisms, thus responding to the call for design strategies that allow diverse microfluidic systems to be assembled from a small set of core components [**19, 82**].

Finally, while we focused on boundary conditions in which the inlet pressures are controlled, it would be natural to explore in future research the scenario in which the controlled variables are the inlet flow rates. We anticipate, for example, that the negative conductance transitions are then converted into pressure amplification (pressure release) transitions in which the inlet-outlet pressure difference increases (decreases) abruptly at the transition point; in particular, an

increase in the driving flow rate can result in abrupt reduction in pressure loss. Accordingly, the Braess paradox is also expected to take a complementary form in which closing the linking channel causes the inlet-outlet pressure difference to drop. Incidentally, it is this complementary form of Braess's paradox that has been previously established for electric circuits [**26**], thus suggesting a new correspondence between electronic and microfluidic circuits.

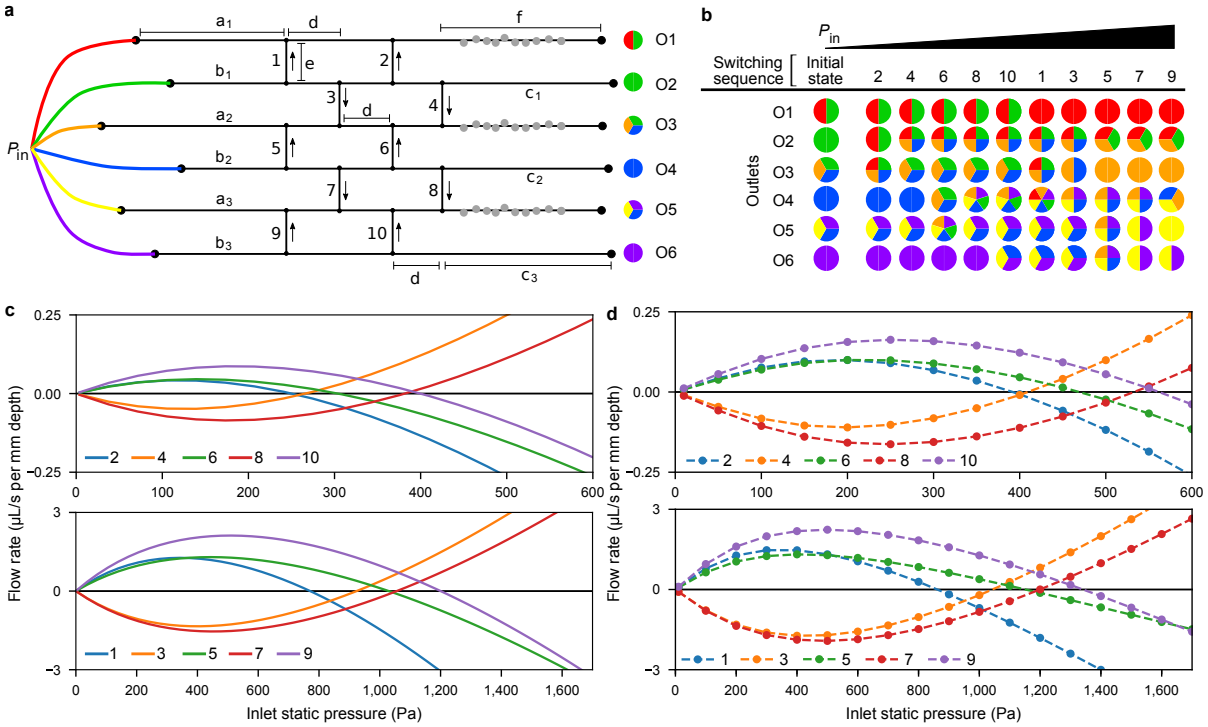

Figure 2.6. **Flow patterns in a multiswitch network.** **a**, Schematic of ten-switch network. Fluids of different colors are driven to each inlet by a common static pressure source, P_{in}. The outlets are labeled by O1–O6 and the linking channels by 1–10. The arrows indicate the flow direction through each linking channel and multicolored circles schematically indicate the fluid composition at each outlet for an initially low P_{in}. The segment lengths are denoted by $a_i, b_i, c_i, d, e,$ and f, where the segments with obstacles are marked with gray circles. **b**, Patterns of outlet flows for the network programmed with a chosen switching sequence as P_{in} is increased. Each column of colored circles denotes the outlet flows after the corresponding flow switch occurs, where mixing between different colored fluids is assumed to occur when passing through the same channel segment. **c,d**, Model predictions (**c**) and simulation results of the Navier-Stokes equations (**d**) for the flow rate through each linking channel for a network designed to exhibit the switching sequence in **b**. The flow rates are labeled according to the channels in **a** and are divided into two sets (top and bottom panels) for clarity. Positive flow rates correspond to flow in the upward direction in **a**, and each flow switch occurs when the corresponding curve crosses the horizontal axis. The segment dimensions that give rise to the particular switching order in **b**-**d** are reported in Table 3.1. All twenty-one possible outlet flow color combinations are realized between the switching sequence presented here and those in Fig. 3.11.

CHAPTER 3

Theory and experiments for microfluidic networks

Here, we present the details of the theoretical model used in the previous chapter to predict Braess's paradox and switching in microfluidic networks. We also show additional experimental demonstrations of nonlinear flow behavior, Braess's paradox, and multiswitch networks. This research was conducted in collaboration with Yifan Liu, Jean-Régis Angilella, István Kiss, and Adilson E. Motter [**44**].

3.1. Model of fluid system

A network schematic of the system in Fig. 2.1a is shown in Fig. 3.1. The inlets are driven by a pressure $P_{\rm in}$ relative to a constant static pressure $P_{\rm out}$ at the outlets, which is taken to be zero without loss of generality. The system includes two internal channel junctions, corresponding to pressures P_1 and P_2. All channels have width w, and the length of each segment is denoted by L. The pressure loss along the linking channel is considered below (minor pressure losses due to the internal junctions are considered in section 3.2). For all other obstacle-free channels, the pressure loss will be approximated by the Poiseuille law in two-dimensions:

$$\frac{-\Delta P}{L} = \frac{12\mu}{w^3} Q, \tag{3.1}$$

where μ is the dynamic viscosity. For the channel segment with obstacles, we make use of the Forchheimer equation:

$$\frac{P_2 - P_{\text{out}}}{L_4} = \frac{\alpha\mu}{w} Q_4 + \frac{\beta\rho}{w^2} Q_4^2, \tag{3.2}$$

where ρ is the fluid density, and α and β are parameters determined using direct numerical simulations.

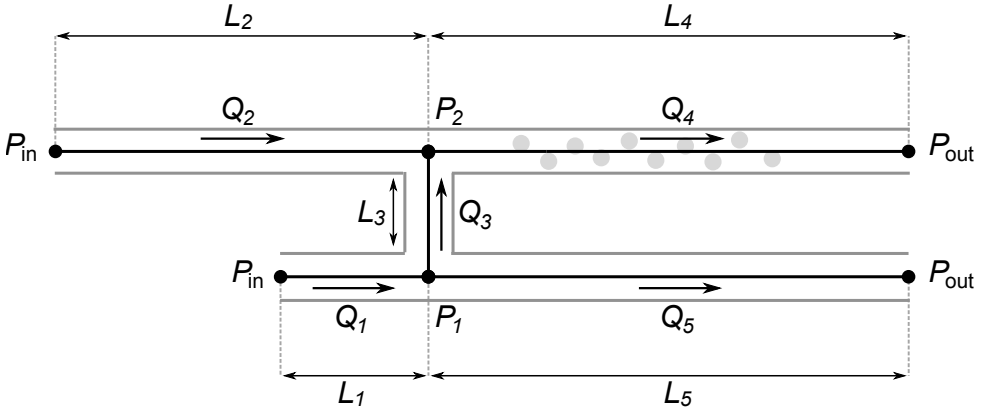

Figure 3.1. **Network representation of the system in Fig. 2.1a.** The flow rate through each segment is indicated by Q, the channel lengths by L, the pressures by P, and the positive flow directions by arrows.

In order to simplify the equations used to describe this system, we first define the non-dimensional pressure $\overline{P}$, flow rate $\overline{Q}$, and channel length $\overline{L}$ as

$$\overline{P} = \frac{P}{\rho\nu^2/w^2},\ \overline{Q} = \frac{Q}{\nu},\ \overline{L} = 12\frac{L}{w}, \tag{3.3}$$

where $\nu = \mu/\rho$ is the kinematic viscosity. Here, we used that Q has the dimensions of ν in two-dimensional flows. The pressure loss equations then take the simpler form

$$-\Delta\overline{P} = \overline{L}\,\overline{Q} \tag{3.4}$$

in obstacle-free channels, and the form

$$\overline{P}_2 - \overline{P}_{\text{out}} = \frac{1}{12}\overline{L}_4(\overline{\alpha}\overline{Q}_4 + \overline{\beta}\,\overline{Q}_4^2) \tag{3.5}$$

for $\overline{\alpha} = \alpha w^2$ and $\overline{\beta} = \beta w$ in the channel with obstacles.

Going forward, all variables are considered to be non-dimensional, unless stated otherwise. The bars over the non-dimensional variables will be omitted for brevity. We use index i to indicate $1, 2, 3, 4, 5$ and, in the case of P, to also indicate *in* and *out*. Moreover, we focus on solutions for with $P_{\text{in}} > 0$ (for both the static and the total pressure at the inlets).

Flow switching under controlled static pressure. When the static pressure is the controlled variable at the inlets, all P_i are taken to be static pressure values. The non-dimensional model is composed of the pressure loss equations for the five channel segments together with the flow rate conservation equations at the two internal junctions. The resulting set of equations reads

$$P_{\text{in}} - P_1 - L_1 Q_1 = 0, \tag{3.6}$$

$$P_{\text{in}} - P_2 - L_2 Q_2 = 0, \tag{3.7}$$

$$P_1 - P_{\text{out}} - L_5 Q_5 = 0, \tag{3.8}$$

$$P_2 - P_{\text{out}} - \frac{1}{12}L_4(\alpha Q_4 + \beta Q_4^2) = 0, \tag{3.9}$$

$$Q_3 - \kappa(\gamma P_1 - P_2) = 0, \tag{3.10}$$

$$Q_3 + Q_2 - Q_4 = 0, \tag{3.11}$$

$$Q_3 + Q_5 - Q_1 = 0, \tag{3.12}$$

where the parameter κ in equation (3.10) is the hydraulic conductivity of the linking channel and the parameter γ allows for an effective pressure difference that governs Q_3. Given the comparatively short length and wide width of the linking channel, κ may deviate from $1/L_3$ and will generally depend on the dimensions of the linking channel. Similarly, γ may deviate from 1 because the magnitude and direction of the flow through the linking channel may be offset from those predicted by the point pressures (P_1 and P_2) due to the finite size of the junctions. As shown in Fig. 3.1, we consider the static pressure at the inlets P_{in} to be equal (and assumed to be tunable). Similarly, the outlets are connected to a common low-pressure reservoir ($P_{\text{out}} = 0$, as noted above).

By setting $\mathbf{X} = (P_1, P_2, Q_1, Q_2, Q_3, Q_4, Q_5)^T$, equations (3.6)-(3.12) take the form

$$\mathbf{G}(\mathbf{X}, P_{\text{in}}) = \mathbf{0}, \tag{3.13}$$

where $\mathbf{G} : \mathbf{R}^7 \times \mathbf{R} \to \mathbf{R}^7$. By adding the constraint $\gamma P_1 = P_2$ (equivalent to setting $Q_3 = 0$) to the system $\mathbf{G}$, we can determine the critical value $P_{\text{in}} = P_{\text{in}}^*$ at which the flow switch through the linking channel occurs. In Fig. 2.5, we used γ to fit the model prediction of P_{in}^* to simulation results. For all discussion that follows, we take $\gamma = 1$ to simplify the analysis. In solving for the flow switching point, we note that zero for all variables is always a solution, but this solution is trivial in that it corresponds to no flows through the system. A solution for $P_{\text{in}}^* > 0$, and thus $X_j > 0$ for all $j \neq 5$ ($X_5 = Q_3 = 0$), can be found only if

$$L_1 < \frac{12 L_2 L_5}{\alpha L_4}. \tag{3.14}$$

Equation (3.14) is the non-dimensional counterpart to equation (2.3) and provides a geometric restriction on the system that must be satisfied in order to observe a switch in the flow direction

through the linking channel for a strictly positive driving pressure P_{in}. Otherwise, the flow rate Q_3 is negative for all $P_{\text{in}} > 0$. When the condition in equation (3.14) is satisfied, the expression for P_{in}^* takes the form

$$P_{\text{in}}^* = \frac{F_1(\alpha)}{\beta}, \tag{3.15}$$

and the total flow rate at P_{in}^* is

$$Q_1 + Q_2 = Q_4 + Q_5 = \frac{F_2(\alpha)}{\beta}, \tag{3.16}$$

where $F_1(\alpha)$ and $F_2(\alpha)$ are polynomial functions of α with coefficients that depend on the channel segment lengths, and β is a property of the channel segment containing obstacles. This dependence on β highlights the importance of the Forchheimer effect for flow switching in the linking channel (see the coefficient of the quadratic term in equation (3.9)).

To analyze the flows through the system near the flow switching point, we consider a small deviation from the critical pressure by setting $P_{\text{in}} = P_{\text{in}}^* + \delta P_{\text{in}}$. We then linearize the system by writing $\mathbf{X} = \mathbf{X}^* + \delta\mathbf{X}$, where $\mathbf{X}^*$ is the solution of $\mathbf{G}(\mathbf{X}^*, P_{\text{in}}^*) = 0$ and $\delta\mathbf{X}$ is a small deviation. This leads to

$$\mathrm{D}\mathbf{G}^* \cdot \delta\mathbf{X} + \left.\frac{\partial \mathbf{G}}{\partial P_{\text{in}}}\right|_{(\mathbf{X}^*, P_{\text{in}}^*)} \delta P_{\text{in}} = \mathbf{0}, \tag{3.17}$$

where the quadratic terms in $\delta\mathbf{X}$ and δP_{in} have been removed and $\mathrm{D}\mathbf{G}^*$ is the Jacobian matrix of $\mathbf{G}$ evaluated at $(\mathbf{X}^*, P_{\text{in}}^*)$. The derivative of $\mathbf{G}$ with respect to pressure P_{in} is simply given by $\frac{\partial \mathbf{G}}{\partial P_{\text{in}}} = \mathbf{e}_1 + \mathbf{e}_2$, where $\mathbf{e}_j$ is the j-th coordinate unit vector. To verify that the flow through the linking channel indeed switches directions at $(\mathbf{X}^*, P_{\text{in}}^*)$, we solve equation (3.17) for the

variation in Q_3:

$$\delta Q_3 = -\mathbf{e}_5^T \mathrm{D}\mathbf{G}^{*-1}(\mathbf{e}_1 + \mathbf{e}_2)\, \delta P_{\mathrm{in}}, \tag{3.18}$$

where $\mathrm{D}\mathbf{G}^*$ is verified to be invertible for the parameters we simulate. Explicit calculation of equation (3.18) yields

$$\delta Q_3 = -\frac{A(\alpha)\kappa}{B(\alpha)\kappa + C(\alpha)}\, \delta P_{\mathrm{in}}, \tag{3.19}$$

where $A(\alpha)$, $B(\alpha)$, and $C(\alpha)$ are polynomial functions of α with coefficients that only depend on the lengths of the channel segments. It can be shown that A, B, and C are strictly positive if equation (3.14) is satisfied. We therefore observe that increasing the inlet pressure above the critical point P_{in}^* forces the fluid to flow in the negative direction ($\delta Q_3 < 0$), whereas for $P_{\mathrm{in}} < P_{\mathrm{in}}^*$, the flow rate through the linking channel is positive, which indicates a switch in the direction of flow through the linking channel at P_{in}^*.

Flow switching under controlled total pressure. When the total pressure is controlled at the inlets, we can consider the inlets of the system in Fig. 3.1 to be directly connected to a common pressurized reservoir. We now take P_{in} to be the pressure of the reservoir and thus the total pressure at the inlets. Then, the non-dimensional static pressure at the inlet of channel segment 1 can be expressed as $P_{\mathrm{in}} - \frac{1}{2}Q_1^2$ and the static pressure at the inlet of channel segment 2 as

$P_{\text{in}} - \frac{1}{2}Q_2^2$. Now, the model near the flow switching point can be written as in equations (3.6)-(3.12), but with equations (3.6)-(3.7) replaced by

$$P_{\text{in}} - \frac{1}{2}Q_1^2 - P_1 - L_1 Q_1 = 0, \tag{3.20}$$

$$P_{\text{in}} - \frac{1}{2}Q_2^2 - P_2 - L_2 Q_2 = 0. \tag{3.21}$$

We perform analysis similar to that done above and recover the same condition established in equation (3.14) for the existence of a (physical) solution for $P_{\text{in}}^* > 0$, which is now the total pressure at which a flow switch occurs. We also find the variation in Q_3 around P_{in}^* to be

$$\delta Q_3 = -\frac{\kappa}{\widetilde{A}\,\kappa + \widetilde{B}}\,\delta P_{\text{in}}, \tag{3.22}$$

where $\widetilde{A}$ and $\widetilde{B}$ are functions that depend on α, β, and the channel segment lengths, but are both positive for the range of parameters we use. Therefore, we see that the flow through the linking channel changes direction at the critical point $(\mathbf{X}^*, P_{\text{in}}^*)$, which is analogous to the result from equation (3.19) for the static pressure controlled case.

3.2. Accounting for minor losses

The Reynolds number of the flows through the microfluidic system in Fig. 3.1 can be of the order of 100 to 1000 under the conditions of our study. Fluid inertia effects are therefore expected to be present, and additional pressure losses at channel junctions, also called *minor* losses, should be considered. The flow rates through channel segments 1 and 5 are an order of magnitude higher than flow rates through the other channels and an extra loss term should be added to equation (3.8) to account for minor losses in segment 5 due to the junction with the linking channel. This minor loss is expected to scale linearly with the average flow velocity

(Q_5/w in dimensional values) at low Re and quadratically at high Re. Here, we use a general formulation to model the minor losses in segment 5, where the coefficient of the scaling factor (usually found empirically) depends on the ratio of the combining or diverging flows[**78**]. The pressure loss equation for channel segment 5, now including a minor loss term, is

$$\frac{P_1 - P_{\text{out}}}{L_5} = Q_5 - K\left(\frac{Q_3}{Q_1}\right) f(Q_5), \tag{3.23}$$

where the scaling factor $f(Q_5)$ and the coefficient $K(Q_3/Q_1)$ are increasing functions for $P_{\text{in}} \geq 0$ such that $f(0) = K(0) = 0$. The latter is consistent with the physical condition of having no minor losses when there is no flow through the linking channel. The inclusion of this minor loss term in equation (3.8) does not alter the condition in equation (3.14) for $P_{\text{in}}^* > 0$ and the associated flow switch. But minor losses are determinant for the emergence of Braess's paradox, as shown next, both when the static pressure and when the total pressure is controlled at the inlets.

Condition for Braess's paradox under controlled static pressure. We modify our model for the static pressure controlled case by replacing equation (3.8) with equation (3.23). Now, the function $\mathbf{G}$ used to define our model in equation (3.13) takes the form

$$\mathbf{G}(\mathbf{X}, P_{\text{in}}) = \mathbf{A}\mathbf{X} + \mathbf{B} - \frac{1}{12} L_4 \beta X_6^2 \, \mathbf{e}_4 + L_5 K\left(\frac{X_5}{X_3}\right) f(X_7) \, \mathbf{e}_3, \tag{3.24}$$

where $\mathbf{A}$ is the matrix containing the coefficients of the linear terms in equations (3.6)-(3.7), equation (3.23), and equations (3.9)-(3.12), and $\mathbf{B} = (P_{\text{in}}, P_{\text{in}}, -P_{\text{out}}, -P_{\text{out}}, 0, 0, 0)^T$ is a vector containing the imposed static pressures at the inlets and outlets.

The Jacobian of $\mathbf{G}$ at any point $\mathbf{X}$, with quadratic terms removed, reads

$$\begin{aligned} \mathrm{D}\mathbf{G} = \mathbf{A} - \frac{1}{6} L_4 \beta X_6 \, \mathbf{e}_4 \otimes \mathbf{e}_6 + L_5 K\left(\frac{X_5}{X_3}\right) f'(X_7) \, \mathbf{e}_3 \otimes \mathbf{e}_7 \\ - L_5 \frac{X_5}{X_3^2} K'\left(\frac{X_5}{X_3}\right) f(X_7) \, \mathbf{e}_3 \otimes \mathbf{e}_3 + \frac{L_5}{X_3} K'\left(\frac{X_5}{X_3}\right) f(X_7) \, \mathbf{e}_3 \otimes \mathbf{e}_5, \end{aligned} \tag{3.25}$$

where $\mathbf{v} \otimes \mathbf{u} \equiv \mathbf{v}\mathbf{u}^T$ indicates the outer product of $\mathbf{v}$ and $\mathbf{u}$, and primes denote derivatives. At the critical point $(\mathbf{X}^*, P_{\text{in}}^*)$, by construction, $Q_3 = X_5 = 0$ and $K(0) = 0$, and thus the Jacobian reads

$$\mathrm{D}\mathbf{G}^* = \mathbf{A} - \frac{1}{6} L_4 \beta X_6^* \, \mathbf{e}_4 \otimes \mathbf{e}_6 + \frac{L_5}{X_3^*} K'(0) f(X_7^*) \, \mathbf{e}_3 \otimes \mathbf{e}_5. \tag{3.26}$$

We have checked that this matrix is non-singular for the range of parameters used here.

We use $\Delta\mathcal{Q} = Q_C - Q_D$ to denote the difference between the total flow rates $(Q_4 + Q_5)$ for the connected (Q_C) and disconnected (Q_D) system configurations. Similarly, we designate the difference in individual channel flow rates between the two configurations by $\Delta Q_i = Q_{i,C} - Q_{i,D}$. Under a small variation δP_{in} around the flow switching point P_{in}^*, at which $Q_C = Q_D$ and $Q_{i,C} = Q_{i,D}$, we have

$$\Delta\mathcal{Q} = \delta Q_C - \delta Q_D, \tag{3.27}$$

$$\Delta Q_i = \delta Q_{i,C} - \delta Q_{i,D}. \tag{3.28}$$

To find $\Delta\mathcal{Q}$, we use the fact that $\delta Q_C = \delta Q_{4,C} + \delta Q_{5,C}$ and that δQ_D can be calculated by taking the limit of δQ_C when $\kappa \to 0$ (i.e., the limit of infinite resistance for the linking channel). After

explicit calculation using equation (3.26), we find

$$\Delta\mathcal{Q} = \kappa\delta P_{\text{in}} \frac{b_1(\alpha) - b_2(\alpha)\, K'(0)\beta f(\frac{a_1(\alpha)}{\beta})}{a_2(\alpha) + a_3(\alpha)\kappa + a_4(\alpha)\kappa K'(0)\beta f(\frac{a_1(\alpha)}{\beta})}, \tag{3.29}$$

where the $a_i(\alpha)$ and $b_i(\alpha)$ are polynomials of α with coefficients that only depend on the channel segment lengths and are positive when equation (3.14) is satisfied. We therefore conclude that, when equation (3.14) is satisfied, Braess's paradox occurs for $\delta P_{\text{in}} > 0$, as observed in our Navier-Stokes simulations and experiments, if and only if

$$K'(0)\beta f\left(\frac{a_1}{\beta}\right) > \frac{b_1}{b_2}, \tag{3.30}$$

where the presence of β and $K'(0)$ highlight the crucial role of nonlinearity and minor losses. Equation (3.30) indicates that if Q_5 is sensitive enough to the flow through the linking channel (i.e., $K'(0)$ is large enough), then the paradox will manifest itself. The compound interaction between the nonlinearity arising from the obstacles and minor losses is further illustrated by the relative magnitude of $\Delta\mathcal{Q}/Q_C$ near P_{in}^*, where $Q_C = F_2(\alpha)/\beta$ from equation (3.16).

The difference in the total flow rate, $\Delta\mathcal{Q}$, can also be broken down into the differences in Q_4 and Q_5. We find

$$\Delta Q_4 = -\kappa\delta P_{\text{in}} \frac{c_1(\alpha)}{c_2(\alpha) + c_3(\alpha)\kappa + c_4(\alpha)\kappa K'(0)\beta f(\frac{a_1(\alpha)}{\beta})}, \tag{3.31}$$

$$\Delta Q_5 = \kappa\delta P_{\text{in}} \frac{g_1(\alpha) - g_2(\alpha)K'(0)\beta f(\frac{a_1(\alpha)}{\beta})}{g_3(\alpha) + g_4(\alpha)\kappa + g_5(\alpha)\kappa K'(0)\beta f(\frac{a_1(\alpha)}{\beta})}, \tag{3.32}$$

where, similarly, the $c_i(\alpha)$ and $g_i(\alpha)$ are polynomials of α with coefficients that only depend on the channel segment lengths and are positive when equation (3.14) is satisfied. Equations (3.31)-(3.32) show how minor losses impact the flow rates at each of system outlets (as discussed in section 3.2).

Condition for Braess's paradox under controlled total pressure. For the scenario in which total pressure is controlled at the inlets, we again substitute equation (3.23) for equation (3.8) to define our model in equation (3.13) with $\mathbf{G}$ now in the form

$$\mathbf{G}(\mathbf{X}, P_{\text{in}}) = \widetilde{\mathbf{A}}\mathbf{X} + \widetilde{\mathbf{B}} - \frac{1}{12}L_4\beta X_6^2\,\mathbf{e}_4 - \frac{1}{2}X_3^2\,\mathbf{e}_1 - \frac{1}{2}X_4^2\,\mathbf{e}_2 + L_5K\left(\frac{X_5}{X_3}\right)f(X_7)\,\mathbf{e}_3, \tag{3.33}$$

where matrix $\widetilde{\mathbf{A}} = \mathbf{A}$ includes the coefficients of the linear terms in equations (3.20)-(3.21), equation (3.23), and equations (3.9)-(3.12), and vector $\widetilde{\mathbf{B}} = (P_{\text{in}}, P_{\text{in}}, -P_{\text{out}}, -P_{\text{out}}, 0, 0, 0)^T$ accounts for the total pressure at the inlets and static pressure at the outlets.

At the critical point $(\mathbf{X}^*, P_{\text{in}}^*)$, again $K(0) = 0$, and the Jacobian reads

$$\mathrm{D}\mathbf{G}^* = \widetilde{\mathbf{A}} - \frac{1}{6}L_4\beta X_6^*\,\mathbf{e}_4 \otimes \mathbf{e}_6 - X_3^*\,\mathbf{e}_1 \otimes \mathbf{e}_3 - X_4^*\,\mathbf{e}_2 \otimes \mathbf{e}_4 + \frac{L_5}{X_3^*}K'(0)f(X_7^*)\,\mathbf{e}_3 \otimes \mathbf{e}_5. \tag{3.34}$$

Performing similar analysis to that done above, we find

$$\Delta\mathcal{Q} = \kappa\delta P_{\text{in}}\frac{\widetilde{b}_1 - \widetilde{b}_2\,K'(0)f(\widetilde{a}_1)}{\widetilde{a}_2 + \widetilde{a}_3\kappa + \widetilde{a}_4\kappa K'(0)f(\widetilde{a}_1)}, \tag{3.35}$$

where $\widetilde{a}_i$ and $\widetilde{b}_i$ are functions that can depend on channel lengths L_i, parameter α, and parameter β, and they are positive for the range of parameters we consider. We therefore conclude that

Braess's paradox occurs for $\delta P_{\text{in}} > 0$ if

$$K'(0) f(\widetilde{a}_1) > \frac{\widetilde{b}_1}{\widetilde{b}_2}, \tag{3.36}$$

similarly to the case when static pressure is controlled.

Prediction of Braess's paradox in model without minor losses. We now elaborate on the need to account for minor losses in order to predict Braess's paradox as observed in our experiments and simulations. The model prediction of Braess's paradox near P_{in}^*, while neglecting minor losses and under static pressure control, can be found directly from equation (3.29) by removing the minor loss terms. Specifically, we have

$$\Delta \mathcal{Q} = \kappa \delta P_{\text{in}} \frac{b_1(\alpha)}{a_2(\alpha) + a_3(\alpha)\kappa}. \tag{3.37}$$

Therefore, the paradox is predicted to exist for $\delta P_{\text{in}} < 0$. We show in Fig. 3.2a the predictions of Q_3 and $\Delta \mathcal{Q}$ for the network used in Fig. 2.3a when minor losses are not included in the model by numerically solving equations (3.6)-(3.12). Braess's paradox is predicted to occur at P_{in} below P_{in}^* with a relative magnitude of less than 0.1%. We also show in Fig. 3.2b the predicted difference in each Q_4 and Q_5 between the connected and disconnected systems. Above P_{in}^*, removing the linking channel results in a small increase in Q_4 and a slightly larger decrease in Q_5, thus resulting in a small net decrease in the total flow rate $(Q_4 + Q_5)$. This directly contrasts with the simulation results in Fig. 2.3a, where the paradox is observed for P_{in} above P_{in}^* in which the removal of the linking channel results in a significant *increase* in Q_5.

To further determine how the inclusion of minor losses in the model alters the prediction of the paradox occurring above or below P_{in}^*, we consider the difference in Q_4 and Q_5, individually, between the connected and disconnected system configurations near P_{in}^*. By removing minor

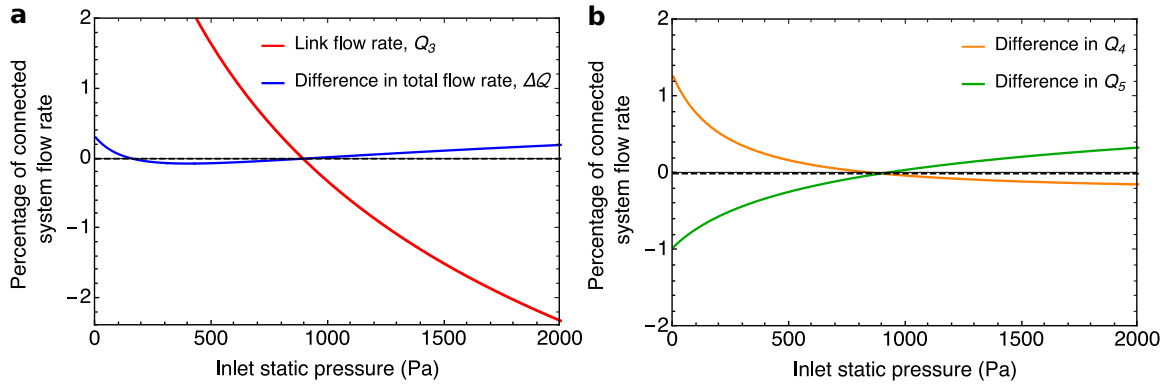

Figure 3.2. **Model prediction of Braess's paradox without minor losses. a**, Flow rate through the linking channel Q_3 and difference in total flow rate $\Delta\mathcal{Q} = Q_C - Q_D$ between the connected and disconnected system configurations as a percentage of Q_C. Braess's paradox is only predicted for a range of P_{in} below P_{in}^* (specifically, the range where $\Delta\mathcal{Q}$ is negative). **b**, Differences in Q_4 and Q_5 between the connected and disconnected configurations. Positive values indicate that the quantity is larger for the connected system configuration. Above P_{in}^*, removing the linking channel causes Q_4 to increase by a small amount and Q_5 to decrease by a slightly larger amount. Hence, Braess's paradox is not predicted for $P_{\text{in}} > P_{\text{in}}^*$. The dimensions of the channels used here are the same as those used in Fig. 2.3. For the linking channel, we estimate the hydraulic resistance as $12\mu L_3/w^3$ and take $\gamma = 1.03$.

loss terms from equations (3.31)-(3.32), we find

$$\Delta Q_4 = -\kappa\delta P_{\text{in}}\frac{c_1(\alpha)}{c_2(\alpha) + c_3(\alpha)\kappa}, \tag{3.38}$$

$$\Delta Q_5 = \kappa\delta P_{\text{in}}\frac{g_1(\alpha)}{g_3(\alpha) + g_4(\alpha)\kappa}. \tag{3.39}$$

Several conclusions follow immediately from equations (3.38)-(3.39). First, for a small increase in the driving pressure above P_{in}^* (i.e., $\delta P_{\text{in}} > 0$), we predict ΔQ_4 to be negative whether minor losses are accounted for or not. This implies that removing the linking channel at P_{in} slightly above P_{in}^*, leads to an increase in Q_4. Second, with minor loss terms neglected, we expect

ΔQ_5 to be positive for $\delta P_{\text{in}} > 0$. This is in accordance with Fig. 3.2b, in which removing the linking channel at $P_{\text{in}} > P_{\text{in}}^*$ results in a decrease in Q_5. However, this contrasts with the result in equation (3.32), where we see that ΔQ_5 is negative for $\delta P_{\text{in}} > 0$ if $K'(0)\beta f(\frac{a_1(\alpha)}{\beta}) > g_1(\alpha)/g_2(\alpha)$. That is, if minor losses are large enough, removing the linking channel (and thus removing the minor losses themselves) can result in an increase in both Q_4 and Q_5 for $P_{\text{in}} > P_{\text{in}}^*$, which is consistent with our simulation and experimental results.

3.3. Supplemental simulation results for Braess's paradox

Flows under controlled static pressure. In analyzing the extent of Braess's paradox as a function of P_{in}, two representations of the data are natural. One is the representation adopted in Fig. 2.3a, in which the flow rates are shown as percentages of the total flow rate for the connected system configuration, Q_C. This accommodates the fact that the total flow rate varies significantly with pressure, and therefore expresses the relative magnitude of the paradox. In Fig. 3.3, we visualize the same data in dimensional values of the flow rates. This representation is useful, for example, for confirming that Q_3 initially increases as a function of P_{in}, which is not directly evident from Fig. 2.3a.

We also consider how the geometry of the linking channel may influence the extent of Braess's paradox in the system presented in Fig. 2.1a. In Fig. 3.4, we show the difference in the total flow rate through the connected and disconnected system configurations for networks in which the linking channel joins the parallel channels at different angles. This geometric change to the system slightly shifts the critical switching pressure P_{in}^* (which may be accounted for in the model by adjusting the value of γ in equation (3.10)), but does not alter the emergence of

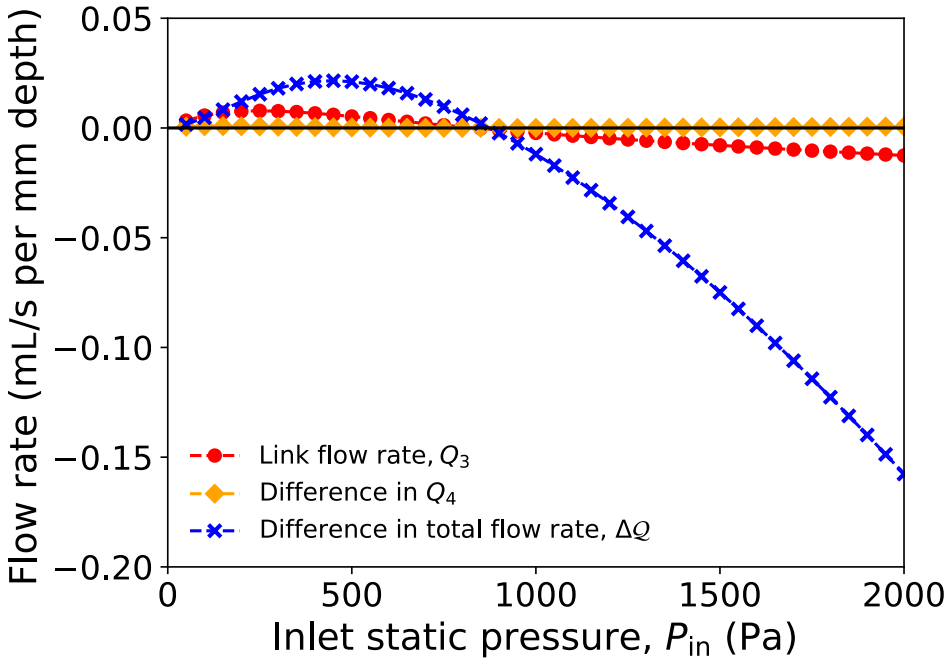

Figure 3.3. **Braess's paradox under controlled static pressure.** Simulation results for the connected and disconnected system configurations in dimensional form. This figure corresponds to Fig. 2.3a, which shows the same data plotted as a percentage of the total flow rate Q_C.

the paradox near P_{in}^*. Moreover, at higher pressures, the magnitude of the paradox may even be enhanced when the junctions with the linking channel deviate from a straight T-junction.

Flows under controlled total pressure. In the previous chapter, the discussion on the simulation results focuses mainly on the scenario in which a common static pressure is controlled at the inlets. This is physically achievable by connecting a pressure regulator to each inlet and then connecting the system to a pressurized reservoir. In our experiments, the system channels directly connect to the pressurized reservoir without intermediate pressure regulators. In this case, the total pressure at the inlets is being controlled and is indeed equal to the pressure of the reservoir. Our simulations show that the results carry over, as shown in Fig. 2.5 for the occurrence of flow switching both when static pressure is controlled and when total pressure is

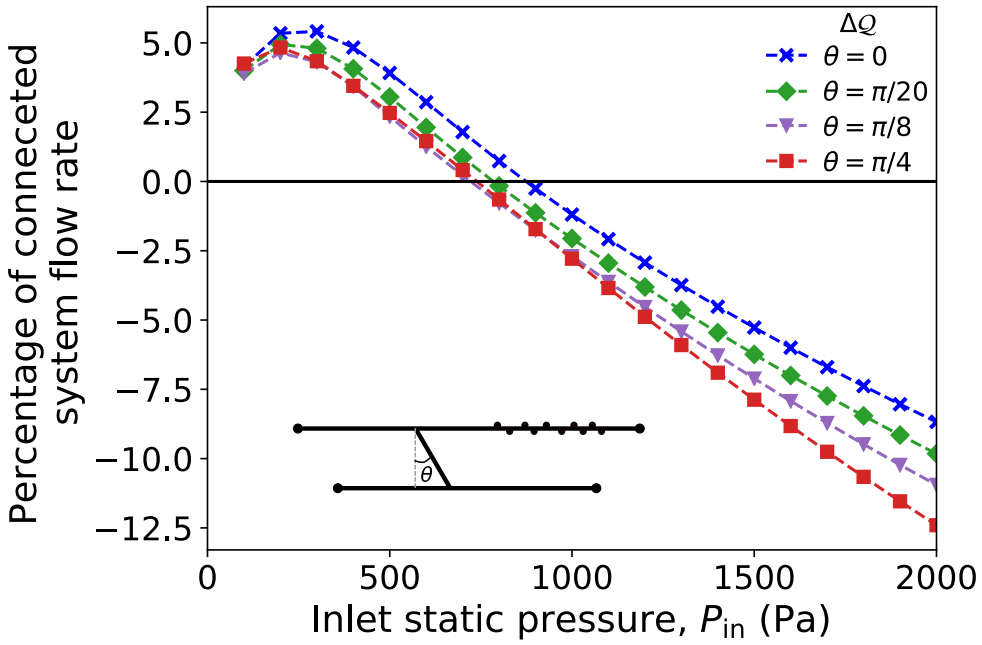

Figure 3.4. **Braess's paradox for different linking channel geometries.** Comparison of flows between the connected and disconnected system configurations for controlled static pressure when the linking channel connects the two parallel channels at different angles. The inset schematic illustrates the network structure and defines the angle θ. Crossing points on the x-axis were verified to correspond to the critical switching pressure for flow through the linking channel (not shown). The case $\theta = 0$ is the same system as in Fig. 2.3a, and the lengths of the channel segments L_1, L_2, L_4, and L_5 are the same for each θ. The length of the linking channel is $(0.1/\cos\theta)$ cm.

controlled. We performed additional simulations to verify that the same holds true for Braess's paradox itself. Figure 3.5 confirms that the paradox persists in the total pressure controlled case and that the onset of the paradox occurs at the flow switching point P^*_{in}, just as was seen in the static pressure controlled case. In addition, there do exist some specific differences between the static and total pressure controlled scenarios. When static pressure is controlled, there is little difference in the flow rate through the channel with obstacles, Q_4, between the cases in which the linking channel is open and closed. However, when total pressure is controlled, Q_4 and Q_5 increase in approximately equal magnitude when the linking channel is closed for $P_{\text{in}} > P^*_{\text{in}}$,

as was observed in our experiments (Fig. 2.4c,d). Also, as a percentage of Q_C, the flow rate through the linking channel is significantly larger and the magnitude of the paradox is smaller when total pressure is controlled than when static pressure is controlled (Fig. 3.5a). The latter point makes our conclusions stronger, since our experiments verified the predicted Braess paradox effect for the pressure boundary conditions under which the effect is weaker.

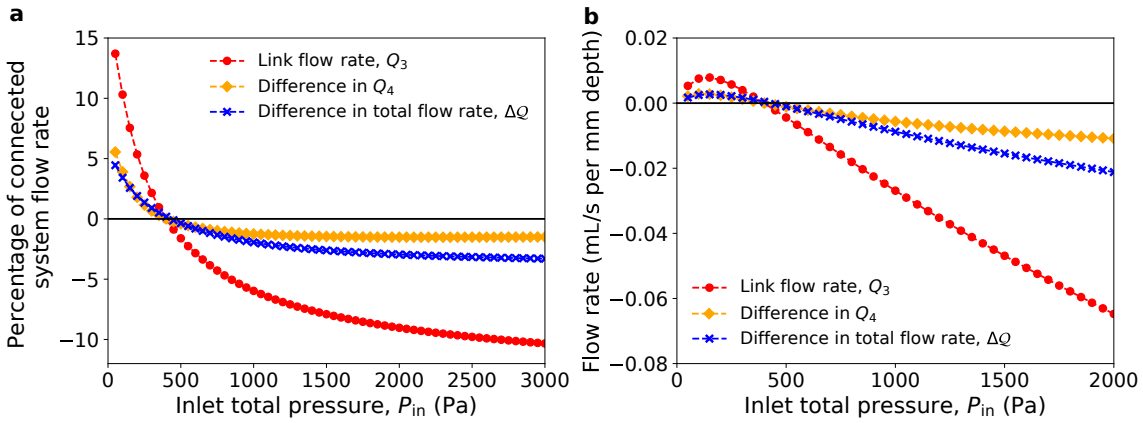

Figure 3.5. **Braess's paradox under controlled total pressure.** Comparison of flow rates through the connected and disconnected configurations when the total pressure is controlled at the inlets. **a**, Flow rates plotted as a percentage of the total flow rate Q_C. **b**, Dimensional values of the flow rates shown in **a**. Panels **a** and **b** are the counterparts of Fig. 2.3a and Fig. 3.3, respectively, where static pressure is controlled. The dimensions of the channels are the same as for Fig. 2.5 with $L_1 = 0.25\,\text{cm}$.

3.4. Simulation results for channel with obstacles

In Fig. 3.6a, we show how the relation between ΔP and Re for a straight channel changes when obstacles are present. The nonlinearity of the relation increases with the number of obstacles and we relate this observed nonlinearity to the Forchheimer effect commonly found in porous media. One of the properties of the Forchheimer relation in equation (2.2) is that the coefficients α and β only depend on the geometric structure of the system and not on properties

of the working fluid. We verify that this property also carries over to our system in Fig. 3.6b. First, we fit the relation between Re and $-\Delta P/Re$ to determine α and β for a channel with ten obstacles. Then, we use these coefficients to predict the same relation for the same channel when a working fluid with a different viscosity is used. The excellent agreement between the prediction and the simulations confirms that α and β are not dependent on the fluid properties. We also observe that as the flow rate is reduced to an Re below $O(1)$, inertial effects become negligible and the relation between Re and $-\Delta P/Re$ plateaus to a constant value (Fig. 3.6c).

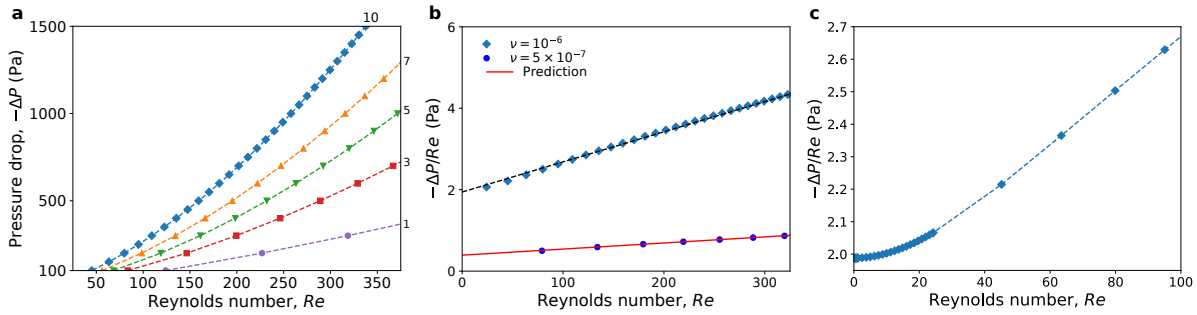

Figure 3.6. **Nonlinearty in flow through a channel with obstacles. a**, Simulation results of the relation between Reynolds number and pressure loss for a channel with varying numbers of cylindrical obstacles (indicated next to each curve). The simulations are performed with a water-like fluid (kinematic viscosity $\nu = 10^{-6}\,\mathrm{m^2/s}$). **b**, Relation between Re and $-\Delta P/Re$ for the channel with ten obstacles (same data shown in **a**) is fit with a straight line (dashed line). Simulation results are indicated by symbols. The fitted parameters, α and β, are used to predict the same relation for flow through the same channel but for a fluid with $\nu = 5 \times 10^{-7}\,\mathrm{m^2/s}$ (continuous line). **c**, Relation between Re and $-\Delta P/Re$ for the ten-obstacle channel in **a** at lower values of Re. The flattening of the relation as Re approaches zero shows that the pressure-flow relation is approximately linear for $Re \leq O(1)$. In all panels, the lengths of the channels are $1.25\,\mathrm{cm}$, and the fitted parameters in **b** are $\alpha = 1.62 \times 10^{8}\,\mathrm{m^{-2}}$ and $\beta = 570\,\mathrm{m^{-1}}$.

3.5. Simulation results for linking channel in the absence of obstacles

An important model prediction for the static pressure controlled case is that when all pressure loss equations are linear (i.e., $\beta = 0$), there is no strictly positive pressure P_{in} at which the flow rate through the linking channel is zero (i.e., $Q_3 = 0$, which would indicate a flow switching point). This implies that nonlinearity is necessary for the observed flow switching effect. We test this prediction using simulations of the connected system configuration but with the obstacles removed from channel segment 4 in Fig. 3.1. Figure 3.7a,b shows the flow rate through the linking channel both when static pressure and when total pressure is controlled at the inlets. We see that, indeed, no switch in the direction of flow through the linking channel is observed.

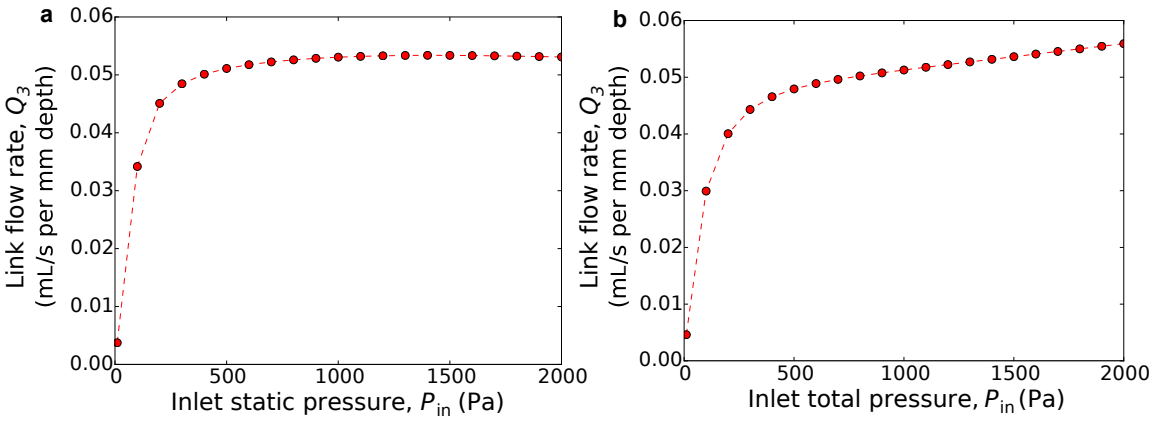

Figure 3.7. **Flow through linking channel for system without obstacles. a**, **b**, Simulation results for flow rate through the linking channel in the absence of obstacles in channel segment 4 when the controlled variable P_{in} is the static pressure (**a**) and total pressure (**b**). We observe no change in flow direction for either case for the range of pressures considered. Following the labels in Fig. 3.1, the dimensions of the channels used in **a** are $L_1 = 0.17$, $L_2 = 0.85$, $L_3 = 0.1$, $L_4 = 1.25$, and $L_5 = 1.0$; in **b** the dimensions used are $L_1 = 0.25$, $L_2 = 3.0$, $L_3 = 0.1$, $L_4 = 1.25$, and $L_5 = 1.4$ (all in units of cm).

3.6. Supplemental experimental results for channel with obstacles, flow switching, and Braess's paradox

The observed nonlinear pressure-flow relation for a channel containing obstacles is essential for programming a flow switch in the linking channel. To confirm inertial effects in the flow around the obstacles as the source of the nonlinearity, we experimentally measure the pressure-flow relation for channels constructed from materials with higher and lower rigidity than the PDMS composition used in the experiments presented in Fig. 2.2e,f. In Fig. 3.8, we show the resulting relations between Re and $-\Delta P/Re$ for channels fabricated from Flexdym and SU-8 photoresist (both with and without obstacles), as well as extended data from the PDMS channels presented in Fig. 2.2e,f. The Flexdym and SU-8 photoresist channels both have approximately the same geometry and dimensions as the PDMS channels. The SU-8 photoresist has a Young's modulus three orders of magnitude larger than that of the PDMS and is thus highly rigid, while Flexdym has a Young's modulus three times smaller than that of the PDMS. In agreement with the results for the PDMS channel, the measurements for both Flexdym and SU-8 photoresist channels show linear dependence of $-\Delta P/Re$ on Re for channels with obstacles and no dependence on Re for channels without obstacles. These results provide additional support for the conclusion that the approximately quadratic relation between $-\Delta P$ and Re for a channel with obstacles arises from inertial effects in the flow around the obstacles.

We also note that the flow switching behavior has no reliance on the manual valve used in the setup of Fig. 2.4. We experimentally demonstrate the flow switch explicitly using a system with a linking channel without a valve in Fig. 3.9.

Finally, in Fig. 3.10 we show further characterization of Braess's paradox through experimentally collected time series data for Q_4, Q_5, and Q_4+Q_5 as the linking channel is sequentially

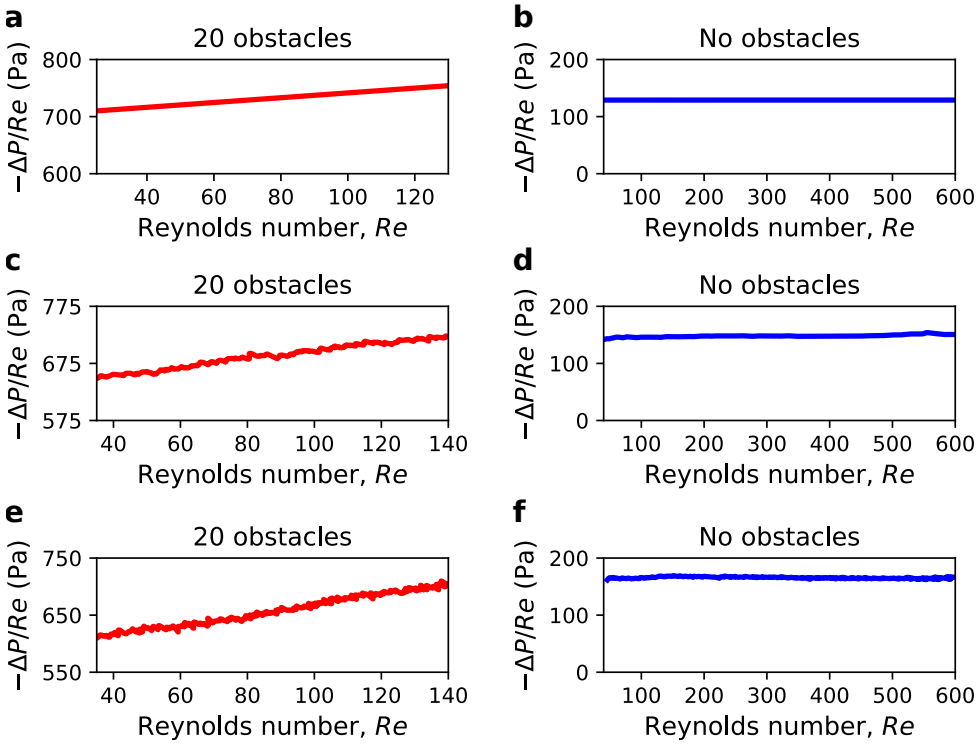

Figure 3.8. **Nonlinear flow in Flexdym, PDMS, and SU-8 photoresist channels. a-f** Experimental measurements of flow rate for Flexdym (**a, b**), hardened PDMS (**c, d**), and SU-8 photoresist (**e, f**) channels with (**a, c, e**) and without (**b, d, f**) obstacles. The range of Re shown in all panels corresponds to approximately the same range of driving pressure, where the higher values of Re in **b**, **d**, and **f** result from the lower hydraulic resistance in the absence of obstacles. The channel dimensions are the same as those used in Fig. 2.2e-f, within the limits of experimental realization.

opened and closed for a driving pressure above P^*_{in}. This supplements the results presented in Fig 2.4b-d, where we present an experimental demonstration of the paradox as evidenced by the increase in the average flow rates Q_4 and Q_5 when the linking channel valve is closed. Figure 3.10a,b shows clear, consistent transitions from higher to lower flow rates through both channel 4 and channel 5 each time the linking channel is opened.

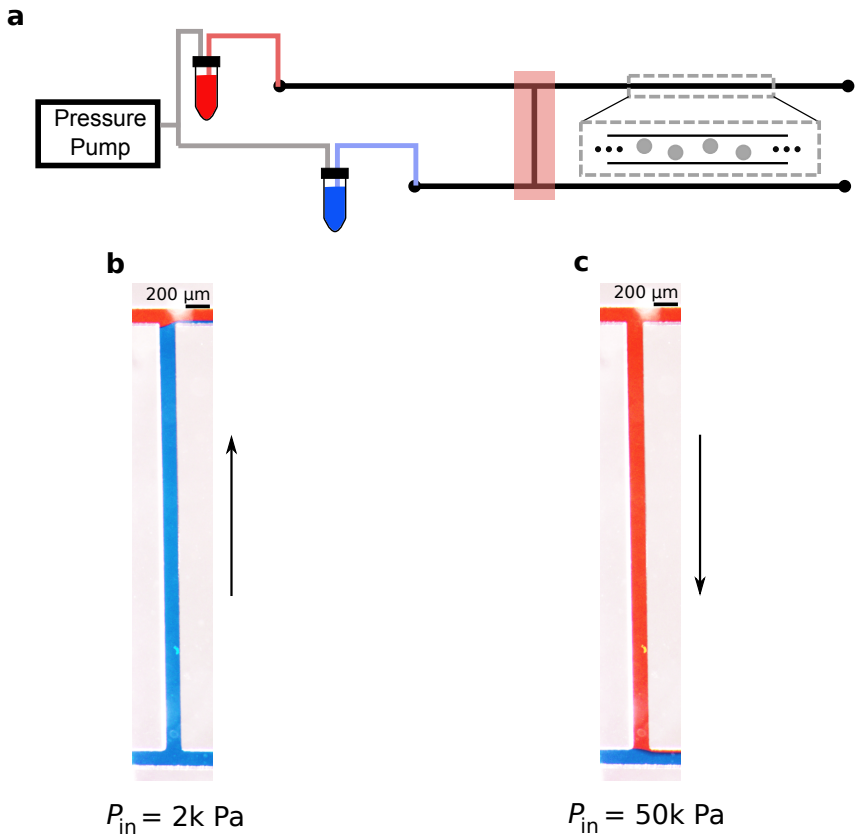

Figure 3.9. **Experimental demonstration of flow switching.** **a**, Schematic of microfluidic network used in Fig. 2.4 without linking channel valve. **b**, **c**, Experimental images of flow through the linking channel for P_{in} below (**b**) and above (**c**) P_{in}^{*} for a camera view corresponding to the red-shaded portion in **a**, where arrows indicate flow directions. All dimensions are the same as in Fig. 2.4, except for the linking channel, which has length $0.6\,\text{cm}$.

3.7. Designing multiswitch networks

Here, we expand on the details of how larger networks, such as those depicted in Fig. 2.1b, can be systematically designed to exhibit multiple switches at desired pressures. The model for a multiswitch network is constructed in the same manner as equations (3.6)-(3.12), whereby a pressure-flow relation is associated to each channel segment along with conservation equations

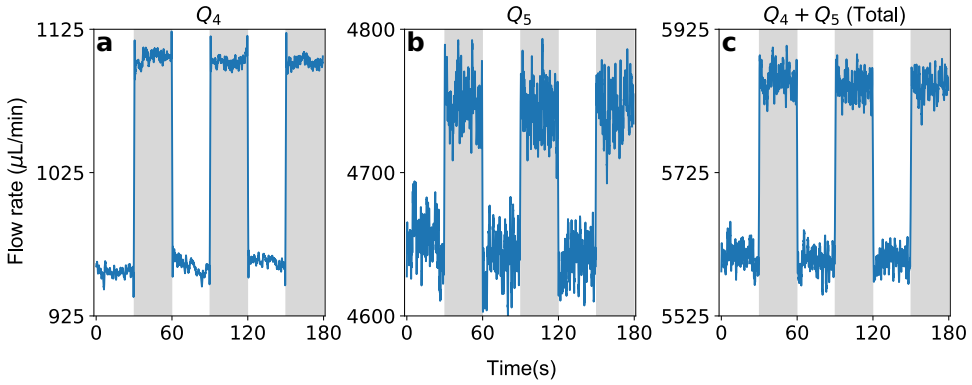

Figure 3.10. **Experimental observation of flow rate impact of linking channel. a-c**, Time series of the measured flow rate through channel 4 (**a**), through channel 5 (**b**), and through the combination of channels 4 and 5 (**c**). The linking channel is sequentially opened (white shade) and closed (gray shade) in 30 second intervals for P_{in} maintained at $80\,\text{kPa}$. All channel segment lengths are the same as in Fig. 2.4, except for the linking channel, which has length $0.6\,\text{cm}$. All channels have a height of $220\,\mu\text{m}$ and a width of $195\,\mu\text{m}$, and the obstacles have a diameter of $99\,\mu\text{m}$.

for each of the channel junctions. For the purpose of designing multiswitch networks, we consider the pressure-flow relations for all channel segments without obstacles (including linking channels) to be of the form of equation (2.1). For the segments with obstacles, relations of the form of equation (3.5) are used. For the ten-switch network in Fig. 2.6a, this amounts to 56 equations, including three nonlinear equations corresponding to the channel segments with obstacles. For given channel dimensions, the critical switching pressure for a specific linking channel can be determined by including an additional constraint into the model that enforces the flow rate through the corresponding linking channel to be zero. The resulting set of 57 equations can then be solved for the critical switching pressure of the linking channel. This process is repeated for each linking channel to yield the set of ten driving pressure values for which the switches occur.

The design challenge is then to determine the channel segment dimensions such that the values of P_{in} at which the flow switches occur correspond to the predefined set of target pressures. If all channel dimensions are specified, the system of equations for large networks can be solved numerically using a root finding method or least-squares approach. Therefore, to determine the channel dimensions that achieve the set of target pressures, we define a nonlinear optimization problem whereby the adjustable parameters are a subset of the channel segment dimensions. The objective function to be minimized is a measure of the distance of the set of switching pressures from the set of target pressures. This approach can be effective in ordering the switches over the working pressure range even if the objective function cannot be brought to zero, which is of relevance since the set of tunable channels in a network can be limited in specific applications. The approach is suitable for use in general applications, especially given that achieving the exact predefined switching pressures is expected to be less important in practice than having the switches occur in the specified order.

In Table 3.1, we present the dimensions of all channel segments and the switching pressures of each linking channel prior to optimization for the ten-switch network in Fig. 2.6. In addition, we show three sets of targeted pressures (corresponding to the switching sequences in Figs. 2.6b and 3.11) and the corresponding switching pressures and channel segment lengths found through optimization. The same initial network structure was used for all optimization runs. The specific objective function used during optimization is the sum of relative differences between the actual and target switching pressures for all linking channels in the network. Optimization was performed using a Nelder-Mead optimization algorithm and was implemented through the Python SciPy Optimize library.

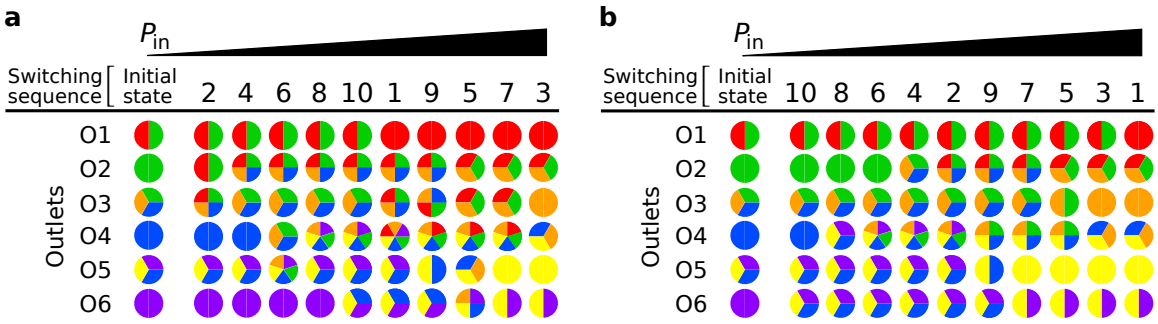

Figure 3.11. **Alternative switching sequences for multiswitch network. a**,**b** Patterns of outlet flows achieved through optimization of the ten-switch network presented in Fig. 2.6 for two targeted switching sequences. The channel segment dimensions that give rise to each sequence are presented in Table 3.1.

In designing the multiswitch networks presented in this study, we considered network layouts in which obstacles were placed in the most downstream segment of every-other parallel channel. Each of the channel segments with obstacles were of the same length and contained the same number of obstacles, so that α and β did not vary between them. In choosing the target pressures, we chose higher pressures for all upstream linking channels than all downstream linking channels, but considered any order otherwise. The resulting number of possible switching orders is still extremely large: $[(n_l/m)!]^m$ for a network consisting of n_l linking channels distributed over m layers. In the specific case of Fig. 2.6, we have $n_l = 10$ and $m = 2$ (one upstream layer of five linking channels and one downstream layer of five linking channels), thus yielding $14,400$ distinct switching orders, each corresponding to a different internal flow state.

We note, however, that the optimization method outlined above is applicable to more general networks. They can include, for example, designs in which segments with obstacles are interspersed throughout the network or the coefficients of the Forchheimer nonlinearity are also considered to be adjustable. While our results demonstrate that the inclusion of obstacles in only a small subset of channels can result in a very large number of flow states, an even larger

number of flow switches, and thus flow states, are achievable by simply adding more linking channels to the network.

Initial Conditions			
Parameters		Switching Pressures	
Name	Value (cm)	Switch	Pressure (Pa)
a_1	0.628	1	737
a_2	0.580	2	337
a_3	0.561	3	309
b_1	0.534	4	264
b_2	0.528	5	495
b_3	0.495	6	242
c_1	5.280	7	249
c_2	5.120	8	218
c_3	4.861	9	425
		10	183

Optimization 1				
Switching Pressures			Parameters	
Switch	Target Pressure (Pa)	Optimized Pressure (Pa)	Name	Optimized Value (cm)
1	800	771	a_1	3.112
2	240	251	a_2	3.392
3	900	924	a_3	3.656
4	280	267	b_1	2.405
5	1000	1029	b_2	2.651
6	320	304	b_3	2.721
7	1100	1056	c_1	4.526
8	360	382	c_2	4.846
9	1200	1200	c_3	4.773
10	400	400		

Optimization 2				
Switching Pressures			Parameters	
Switch	Target Pressure (Pa)	Optimized Pressure (Pa)	Name	Optimized Value (cm)
1	800	796	a_1	4.926
2	240	241	a_2	5.386
3	1200	1198	a_3	5.541
4	280	279	b_1	3.781
5	1000	1025	b_2	4.230
6	320	308	b_3	4.525
7	1100	1068	c_1	4.367
8	360	376	c_2	4.720
9	900	900	c_3	4.819
10	400	400		

Optimization 3				
Switching Pressures			Parameters	
Switch	Target Pressure (Pa)	Optimized Pressure (Pa)	Name	Optimized Value (cm)
1	1200	1140	a_1	6.724
2	400	424	a_2	6.882
3	1100	1132	a_3	6.853
4	360	343	b_1	5.129
5	1000	1064	b_2	5.405
6	320	299	b_3	5.412
7	900	868	c_1	4.555
8	280	294	c_2	4.543
9	800	807	c_3	4.304
10	240	239		

Table 3.1. **Optimized design of ten-switch network.** Top left columns: initial channel dimensions and switching pressures of the network, where the switch numbers and parameters are as marked in Fig. 2.6a. Top right columns: target switching pressures, optimized switching pressures, and optimized channel dimensions corresponding to the switching order in Fig. 2.6b-d. Bottom left columns: same as in the top right columns for the target pressures corresponding to the switching order in Fig. 3.11a. Bottom right columns: same as in the top right columns for the target pressures corresponding to the switching order in Fig. 3.11b. The other (fixed) channel segment lengths are $d = 0.475$ cm, $e = 0.3$ cm, and $f = 1.25$ cm. In addition, the width of the five upstream and five downstream linking channels is 2.39×10^{-2}cm and 1.11×10^{-2}cm, respectively; the width of all other channels is $w = 5 \times 10^{-2}$cm.

3.8. Experimental demonstration and simulation of multiswitch network

In the previous chapter, we discuss the design of microfluidic networks with multiple linking channels. We have experimentally verified the switching behavior in one such network using the setup in Fig. 3.12a, which includes six linking channels and two channel segments each containing twenty obstacles. In this experiment, dyed water is driven into each inlet by the same pressure source. Images of the flow through all channels are depicted at low (Fig. 3.12b) and high (Fig. 3.12c) values of the source pressure. At low driving pressure, the flows through the linking channels are oriented towards the channels containing obstacles. As P_{in} is increased, the flow direction through each linking channel switches, resulting in a pattern of flows diverging from the channels with obstacles.

In Fig. 3.13, we show the internal flow patterns obtained through two-dimensional simulations of a six-switch network, similar to the one used in the three-dimensional experiments. The same switching behavior is again observed as in the experiments: at low pressures, flows enter the channels with obstacles through the linking channels, and at high pressures, flows diverge from the channels with obstacles. This behavior is evident in both the experiments and simulations by observing the difference in the flow compositions of each outlet at low and high driving pressures. In particular, the flows (at the outlets) with pure blue compositions at low pressure transition to mixed red/blue compositions at high pressure. Similarly, the flows with mixed red/blue compositions at low pressure transition to pure red compositions at high pressure.

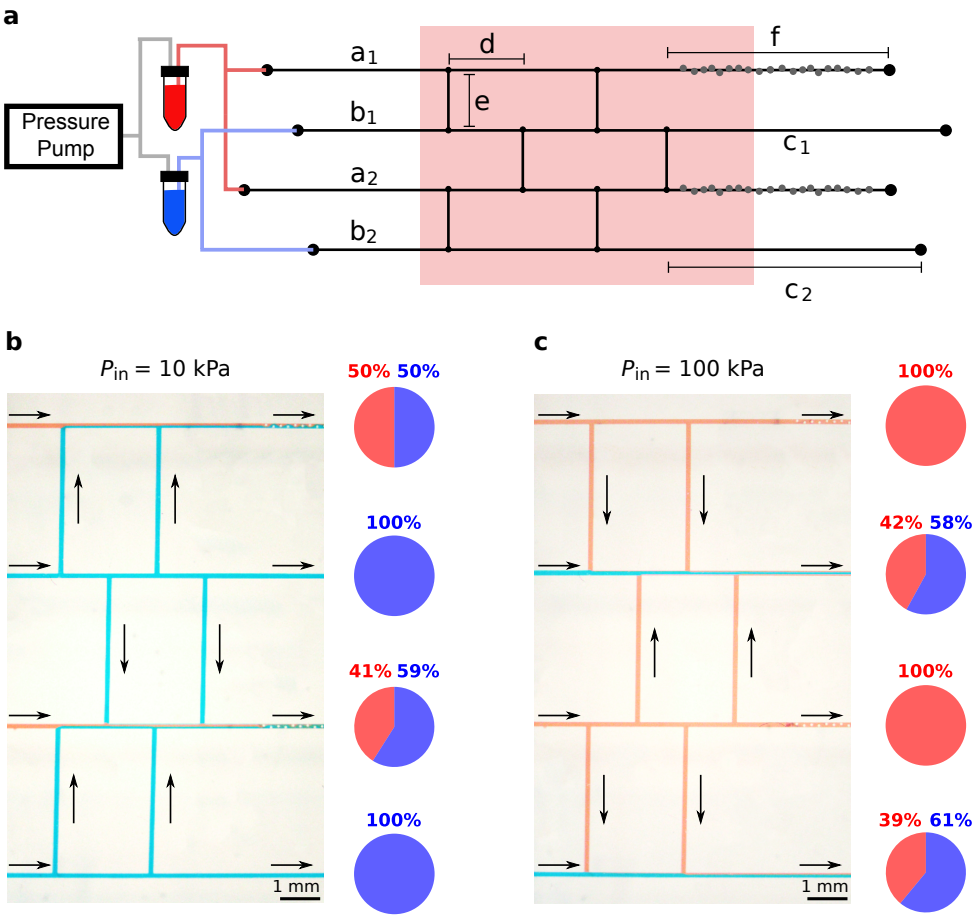

Figure 3.12. **Experimental demonstration of six-switch network.** **a**, Schematic of experimental setup, where red- and blue-dyed water is driven into individual inlets by a common pressure P_{in}. The shaded rectangle depicts the camera view. **b**, **c**, Images of flows through the network for low (**b**) and high (**c**) driving pressure P_{in}, where the arrows indicate flow direction. The pie charts show the flow composition at each outlet, as determined through the proportion of red and blue pixels extracted from the image along a line perpendicular to the flow direction (and upstream from the obstacles) for each outlet channel. The dimensions of the channel segments are $a_1 = a_2 = 0.738, b_1 = b_2 = 0.515, c_1 = c_2 = 4.117, d = 0.195, e = 0.6$, and $f = 1.25$ (all in units of cm). Two channel segments each contain twenty obstacles (indicated by grey circles in **a**) with diameters of $112\ \mu$m. All channels have a height of $219\ \mu$m and width of $194\ \mu$m.

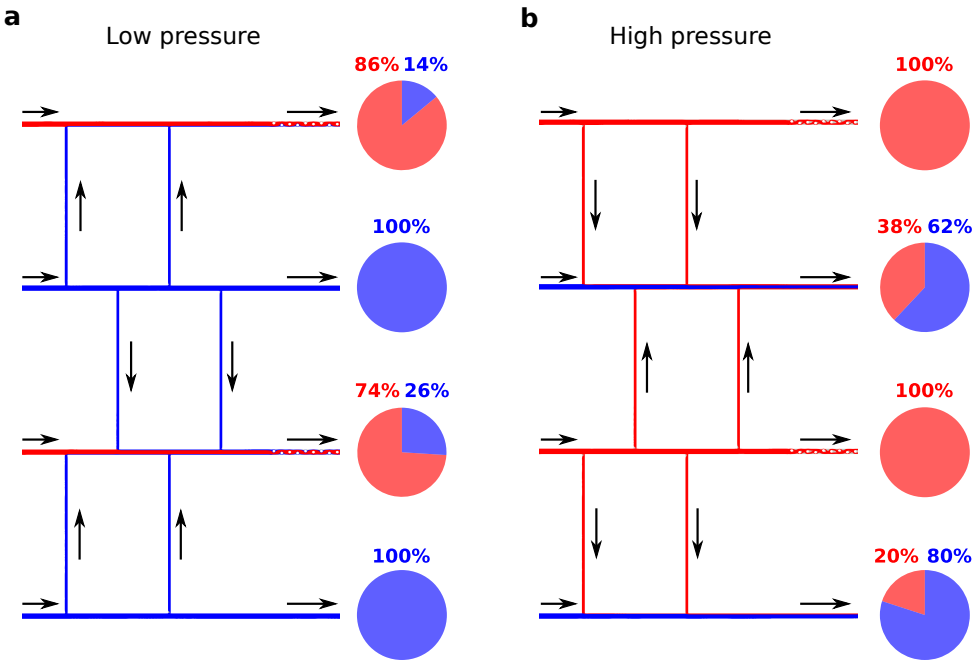

Figure 3.13. **Simulation of six-switch network. a**, **b**, Simulation results of the Navier-Stokes equations for flow through the network presented in Fig. 3.12a. Red and blue streamlines show the flows originating from the inlets with the corresponding colored fluid at low (**a**, $P_{\text{in}} = 1\,\text{kPa}$) and high (**b**, $P_{\text{in}} = 30\,\text{kPa}$) driving pressures, where the total pressure was controlled at the inlets. The view of the network corresponds to the shaded rectangle in Fig. 3.12a and the arrows indicate the direction of flow. The pie charts show the flow composition at each outlet, as determined through the proportion of the sample of red and blue streamlines that intersect the cross-section of each outlet channel (upstream from the obstacles). The dimensions of the channel segments are $a_1 = a_2 = 0.738, b_1 = 0.390, b_2 = 0.515, c_1 = c_2 = 4.117, d = 0.195, e = 0.6$, and $f = 1.05$ (all in units of cm). Two channel segments each contain twenty obstacles (indicated by grey circles in Fig. 3.12a) with diameters of $100\,\mu$m. All linking channels have a width of $100\,\mu$m and all other channels have a width of of $200\,\mu$m.

CHAPTER 4

Spontaneous oscillations and negative conductance transitions in microfluidic networks

The tendency for flows in microfluidic systems to behave linearly poses a challenge for designing integrated flow control schemes to carry out complex fluid processing tasks. This hindrance has led to the use of numerous external control devices to manipulate flows, thereby thwarting the potential scalability and portability of lab-on-a-chip technology. Here, we devise a microfluidic network exhibiting nonlinear flow dynamics that enable new mechanisms for on-chip flow control. This network is shown to exhibit oscillatory output patterns, bistable flow states, hysteresis, signal amplification, and negative conductance transitions, all without reliance on external hardware, movable parts, flexible components, or oscillatory inputs. These dynamics arise from nonlinear fluid inertia effects in laminar flows that we amplify and harness through the design of the network geometry. We suggest that these results, which are supported by fluid dynamical simulations and theoretical modeling, will inspire development of new built-in control mechanisms for applications ranging from on-chip clocks and integrated memory to synchronization. This research was conducted in collaboration with Jean-Régis Angilella and Adilson E. Motter.

4.1. Motivation

Microfluidic systems—networks of miniature flow channels capable of processing fluids—are now commonly used in applications ranging from chemical analysis [**46**] and flow cytometry

[**83**] to computing [**84**] and point-of-care diagnostics [**16**]. The value of microfluidic networks is manifest in their utility for manipulating fluid motion with precision. However, such manipulation is often controlled through the use of external hardware [**45, 16, 15**]. For instance, microscopic valves generally need to be actuated by macroscopic, computer-operated pumps [**20**], which has impeded development of portable microfluidic systems [**16, 15**]. The need for active control stems from the low Reynolds numbers typical of microfluidic flows, whereby fluid inertia forces are small relative to viscous dissipation, causing flow rate changes to be linearly related to pressure changes [**11**]. Thus, it remains challenging to design integrated control mechanisms that are capable of inducing responsive flow dynamics, such as oscillations, switching, and amplification, without relying on external actuation.

Nonetheless, significant progress has been made in the development of built-in microfluidic controls. State-of-the-art approaches for incorporating passive valves for flow rate regulation generally take advantage of flexible membranes and surfaces to generate nonlinear fluid-structure interactions [**23, 56, 47, 14**]. Complex flow patterns and logic operations have been implemented in such networks, but flexible components can hinder integration, yield to high driving pressures, and may require polymer materials that are not chemically compatible with the working fluid [**13, 15, 16**]. On the other hand, recent appreciation has emerged for the impact and utility of fluid inertia effects on manipulating local flow dynamics in microfluidics [**59, 60, 85**]. It has been shown that even for moderate Reynolds numbers, the formation of vortices and secondary flows can be exploited for particle segregation [**64, 86, 65, 87**], mixing fluids [**63, 88, 89**], and diverting flow streams [**61, 62**].

Here, we present a microfluidic network construction that demonstrates new dynamics resulting from fluid inertia, which, importantly, can serve as novel flow control mechanisms and

facilitate the design of fully integrated microfluidic systems. Our network exhibits: (i) spontaneous emergence of persistent flow-rate oscillations for fixed driving pressures; (ii) hysteretic flow behavior in which more than one set of stable flow rates exist for the same driving pressures; and (iii) negative conductance transitions, whereby an increase (decrease) in the driving pressure leads to a discontinuous decrease (increase) in the flow rate. These behaviors are interesting in their own right, and are analogous to phenomena found in electronic circuits (although the mechanisms giving rise to them are fluid-specific and crucially different, as we demonstrate here). Moreover, the behaviors in (i) and (ii) are paramount for establishing microfluidic logic systems [**90, 47, 84**] and timing mechanisms [**14, 54**], for which they have been generated via external hardware or through use of elastic components. The counter-intuitive behavior in (iii), sought previously using flexible diaphragm valves [**91, 92**], could be used for signal amplification and flow switching. Our network does not include flexible components nor relies on external control devices. Instead, these behaviors arise by structuring the network so that dynamic vortices are generated in the flow and nonlinear fluid inertia effects are amplified. The results presented in this work are derived from simulations of the Navier-Stokes equations and an analytical dynamical model developed to capture the diverse flow properties of the network.

4.2. Microfluidic network description and simulation results

A circuit schematic of our microfluidic network is shown in Fig. 4.1. The network consists of five channel segments that are constructed into two parallel paths connected by a transversal path. Generally, the steady-state relation between the flow rate Q through a microfluidic channel and the pressure loss ΔP along the channel takes the form $\Delta P = RQ$, where R is the (absolute) fluidic resistance of the channel. When R is constant, this relation is analogous to Ohm's law

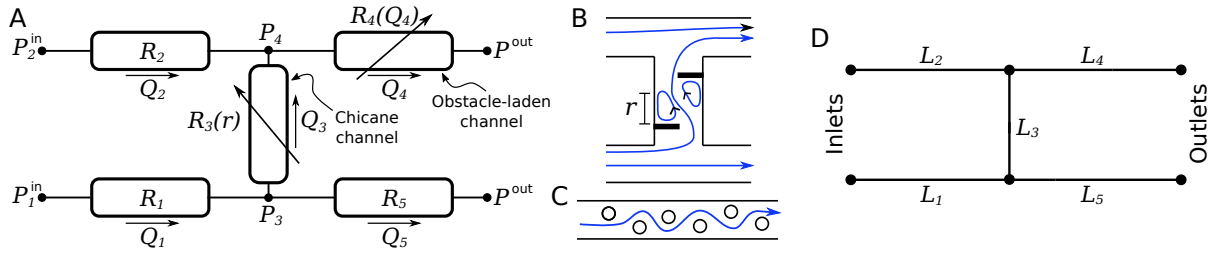

Figure 4.1. **Microfluidic network structure.** (**A**) Circuit schematic of the network, where the labels denote pressures (P_i), channel resistances (R_i), and flow rates (Q_i). The inlet and outlet pressures are identified by the superscripts "in" and "out", respectively, and the positive flow directions are indicated by arrows. Two channels exhibit variable (flow-dependent) resistance due to the presence of obstacles. (**B-C**) Geometric structure of the chicane (B) and obstacle-laden (C) channels. The blue curves mark example streamlines and specify flow direction. The closed streamlines in (B) represent vortices that form near the barriers and r marks the linear size of the left vortex. (**D**) Network topology of the circuit in (A), where the length of each channel segment is labeled by L_i.

for electronic resistors [**17, 18**]. Therefore, we represent the three (straight) channels in the network that exhibit constant fluidic resistance as linear resistors in the schematic (Fig. 4.1A). The two remaining channels include either a chicane of blade-like barriers (Fig. 4.1B) or an array of six cylindrical obstacles (Fig. 4.1C) that induce nonlinear pressure-flow relations and are represented as nonlinear resistors. As we show below, the obstacle-laden channel serves to amplify inertial effects and the chicane channel gives rise to oscillations. The lengths of the channels vary (Fig. 4.1D) but all share a common width w of $500\,\mu$m. The cylindrical obstacles have a radius of $w/5$ and the two barriers, which extend to the center of the chicane channel, are of thickness $w/10$. No-slip boundary conditions are assumed at all surfaces, and we consider the static pressure at the outlets of the system P^{out} to be held at a fixed common value, taken to be zero. At the inlets, we control either the pressures (P_1^{in} and P_2^{in}) or the flow rates (Q_1 and Q_2).

For the network presented in Fig. 4.1, the individual channel segment lengths, as labeled in Fig. 4.1D, are: $L_1 = 0.1$, $L_2 = 0.6$, $L_3 = 0.1$, $L_4 = 1.0$, and $L_5 = 0.5$, all in cm. The cylindrical obstacles in the obstacle-laden channel (Fig. 4.1C) are separated by a distance of approximately $6w/5$. The blade-like barriers in the chicane channel (Fig. 4.1B) are each placed a distance $w/2$ from the midpoint of the axis along the channel.

We present the outstanding properties of this microfluidic network through fluid dynamics simulations of incompressible flow in two-dimensions. We consider a water-like working fluid with density $\rho = 1000$ kg/m^3 and dynamic viscosity $\mu = 10^{-3}$ Pa·s. In microfluidics, pressure-driven flow is used across a variety of applications [**45**], whereby the system inlets are connected to a pressurized fluid reservoir, the outlets are open to atmosphere (or a lower pressure reservoir), and flow is driven by the resulting pressure gradient. Here, we investigate the case in which a common static pressure is applied at the inlets, that is $P_1^{\text{in}} = P_2^{\text{in}} = P^{\text{in}}$, which corresponds to the physical scenario in which the inlets are connected to a high pressure reservoir through intermediate passive pressure regulators.

Our simulations of the Navier-Stokes equations for incompressible fluid were performed using OpenFOAM-version 4.1. Meshes of the system geometry were generated using Gmsh-version 2.9.3, with average cell area ranging from 10 to 70 μm^2. The pisoFoam and simpleFoam solvers in OpenFOAM were used for time-dependent and steady-state simulations, respectively. For simulations where a Dirichlet static pressure boundary condition was used at an inlet/outlet, a Neumann boundary condition was used to set the gradient of the velocity field to zero in the direction normal to the inlet/outlet. This combination of boundary conditions results in a fully-developed velocity profile at the inlet/outlet, and corresponds to the physical situation in which the channels extend upstream and downstream of the computational domain. Similarly, when

instead the flow rate was controlled at an inlet, a parabolic velocity profile was specified and a zero-gradient boundary condition was used for the pressure.

In Fig. 4.2A, we show simulation results of the total flow rate $Q_T = Q_1 + Q_2$ through the network in Fig. 4.1 over a range of driving pressures, P^{in}, from which we observe two striking properties. First, for P^{in} within two disjoint ranges, two stable solutions for the total flow rate exist. Second, a subset of solutions are unsteady and exhibit oscillating flow rates (further details provided in section 4.4 and Fig. 4.11), despite P^{in} being fixed. In particular, we find that at a critical value of P^{in}, solutions along the high-flow branch (red symbols in Fig. 4.2A) become small-amplitude limit cycles. The corresponding amplitudes and periods grow with P^{in} (the frequency of the oscillations range from 4-20 Hz; see Fig. 4.10), and at a higher critical P^{in} the limit cycle collides with the unstable branch, thereby destabilizing the high-flow solution branch. An important property of the oscillating solutions is that the proportions of the flow rates through different channel segments also become time-dependent (Fig. 4.2B). Bistability and spontaneous oscillations have been previously studied in fixed-structure microfluidic networks when feedback loops are incorporated [**93**] or when multiple working fluids with different viscosities are used [**94**]. However, neither of these mechanisms are required in our system.

The characteristic length scale used in defining the Reynolds numbers of the flows is the hydraulic diameter of the channels, defined as $4A/P$, where A is the area and P is the perimeter of the channel cross section (common to all channel segments). In two dimensions, the hydraulic diameter is $2w$ and the characteristic velocity used is Q/w. Therefore, we define the Reynolds number for individual channel segments to be $2\rho Q/\mu$, where Q is the associated flow rate through the channel.

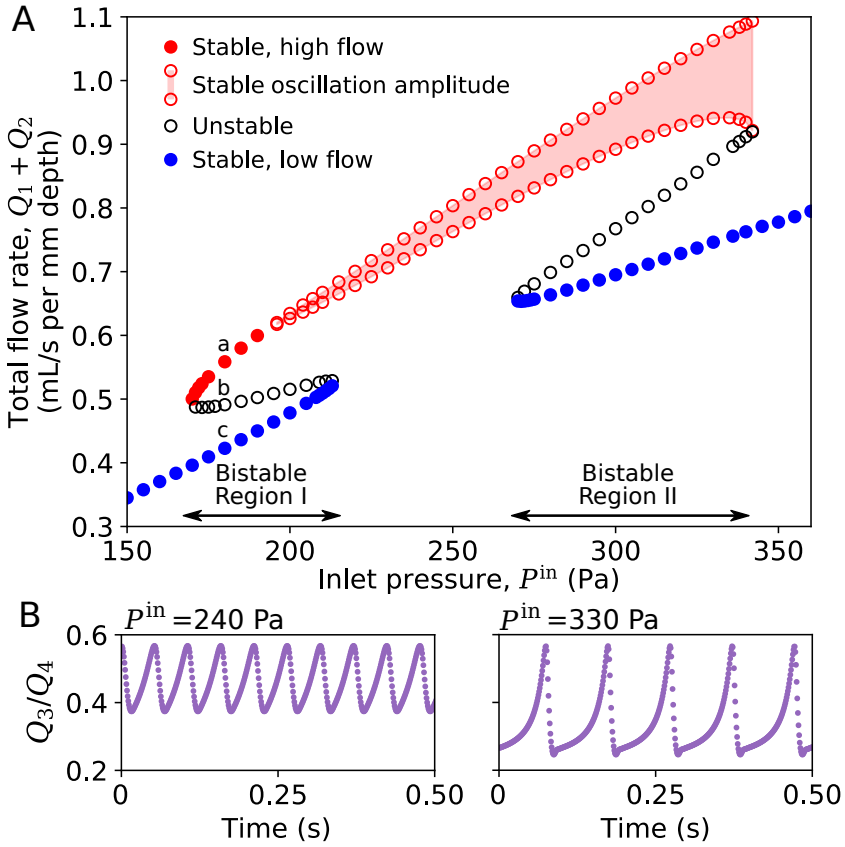

Figure 4.2. **Bistability and spontaneous oscillations.** (**A**) Bifurcation diagram of total flow rate as a function of the inlet pressure P^{in}, generated from direct simulations of the network in Fig. 4.1 for $P_1^{\text{in}} = P_2^{\text{in}} = P^{\text{in}}$. There exist stable high-flow (red) and low-flow (blue) solution branches, separated by an unstable intermediate-flow branch (black). Oscillating solutions arise spontaneously along the high-flow branch, where the oscillation amplitude is indicated by the shaded region. The Reynolds number for flows through the chicane channel and the obstacle-laden channel are in the range of 14–90 and 80–155, respectively. The solutions for $P^{\text{in}} = 180\,\text{Pa}$, marked with a, b, and c, will be used as references in comparing with other figures. The unstable solutions are determined through flow controlled simulations (further details provided in section 4.4 and Fig. 4.9). (**B**) Time series of the proportion of flow exiting the obstacle-laden channel that passes through the chicane channel (Q_3/Q_4) for two driving pressures that yield oscillatory flows, showing that frequency decreases and amplitude increases as the driving pressure is increased.

Another outstanding property that arises from the bistability in our system is the possibility of negative conductance transitions and other sudden transitions in Q_T that result from small changes in P^{in}. We characterize these transitions, which occur at the boundaries of the bistable regions (Fig. 4.2A), by defining (local) fluidic conductance and resistance as $C = \delta Q_T / \delta P^{\text{in}}$ and its reciprocal, respectively. Here, δ indicates a finite change and P^{in} is the controlled variable. Therefore, negative conductance and resistance occur when an increase (decrease) in P^{in} leads to a decrease (increase) in Q_T. More importantly, our system exhibits transition points, as shown in Fig. 4.3A, at which $C(\delta P^{\text{in}})$ diverges in the limit of small δP^{in}: two points at which $C(\delta P^{\text{in}} \to 0) = +\infty$, corresponding to positive conductance transitions, *and* two points at which $C(\delta P^{\text{in}} \to 0) = -\infty$, corresponding to negative conductance transitions. Figure 4.3B shows that related transitions emerge when the flow rate Q_T, rather than the pressure P^{in}, is taken as the control variable. In this case, a change in Q_T can lead to transitions in which P^{in} changes by a finite amount. In particular, the later includes signal amplification transitions, which are remarkable transitions in which an infinitesimal increase (decrease) in Q_T leads to a finite decrease (increase) in P^{in}. Both the pressure and flow driven transitions reported here are intimately related to the emergence of hysteresis in the system, which is another consequence of bistability that has potential applications in the development of systems with built-in memory.

The solutions belonging to the different branches in Fig. 4.2A can be further distinguished by the flow rates through specific channels as well as the internal flow structure. It is particularly insightful to examine the streamlines around the complex geometry in the chicane channel, and the associated flow rate Q_3. In Fig. 4.4A, we show the streamlines corresponding to the three labeled states in Fig. 4.2A. A number of steady vortices are observed in the flow around the barriers. The sizes of the vortices are correlated and we designate r to be the size of one of

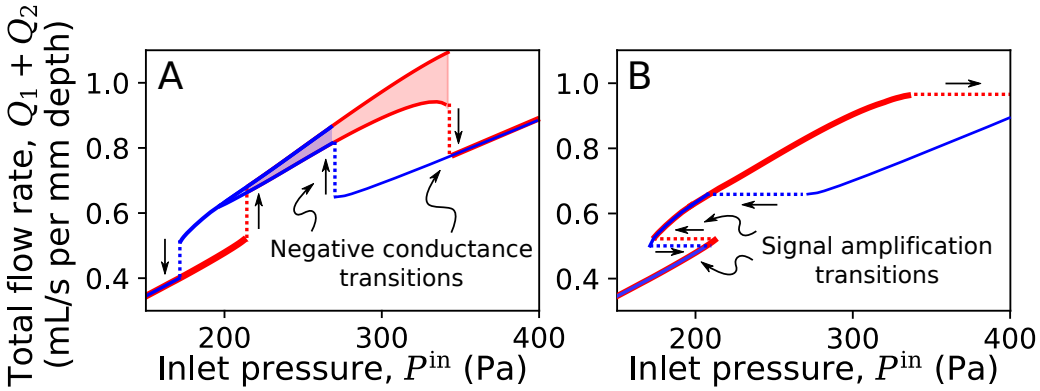

Figure 4.3. **Hysteresis and negative fluidic transitions.** (**A**) Hysteresis loop and resulting negative conductance transitions for the network in Fig. 4.1 when quasistatically increasing (red) or decreasing (blue) the inlet driving pressure. (**B**) Counterpart of (A) and resulting signal amplification transitions when quasistatically varying the total flow rate. For the latter, Q_1 and Q_2 are controlled so as to maintain equal pressures at the inlets.

them, as labeled in Figs. 4.1B and 4.4A. We use a one-dimensional measure for r, taken to be the distance from the barrier to the vortex reattachment point along the channel wall. In Fig. 4.4, B and C, we show that both Q_3 and r differ markedly for solutions belonging to the three branches in Fig. 4.2A and that oscillations simultaneously emerge in these variables (further details provided in section 4.4 and Fig. 4.11). Notably, solutions along the high- (low) flow branch in Fig. 4.2A correspond to large (small) values of Q_3 and r.

We determine the relationship between r and Q_3 by performing simulations in which the flow rates at both inlets (Q_1 and Q_2) are controlled. From these simulations we compute r, Q_3, and the pressure loss along the chicane channel ΔP_{34}, where the latter corresponds approximately to $P_3 - P_4$ (Fig. 4.1). In Fig. 4.5, we show relations between these quantities for sets of simulations in which Q_1 is fixed while Q_2 is varied. We observe nonlinear relations between r and Q_3 (Fig. 4.5A), between Q_3 and the pressure loss along the chicane channel (Fig. 4.5B), and between r and the fluidic resistance of the chicane channel (Fig. 4.5C). These

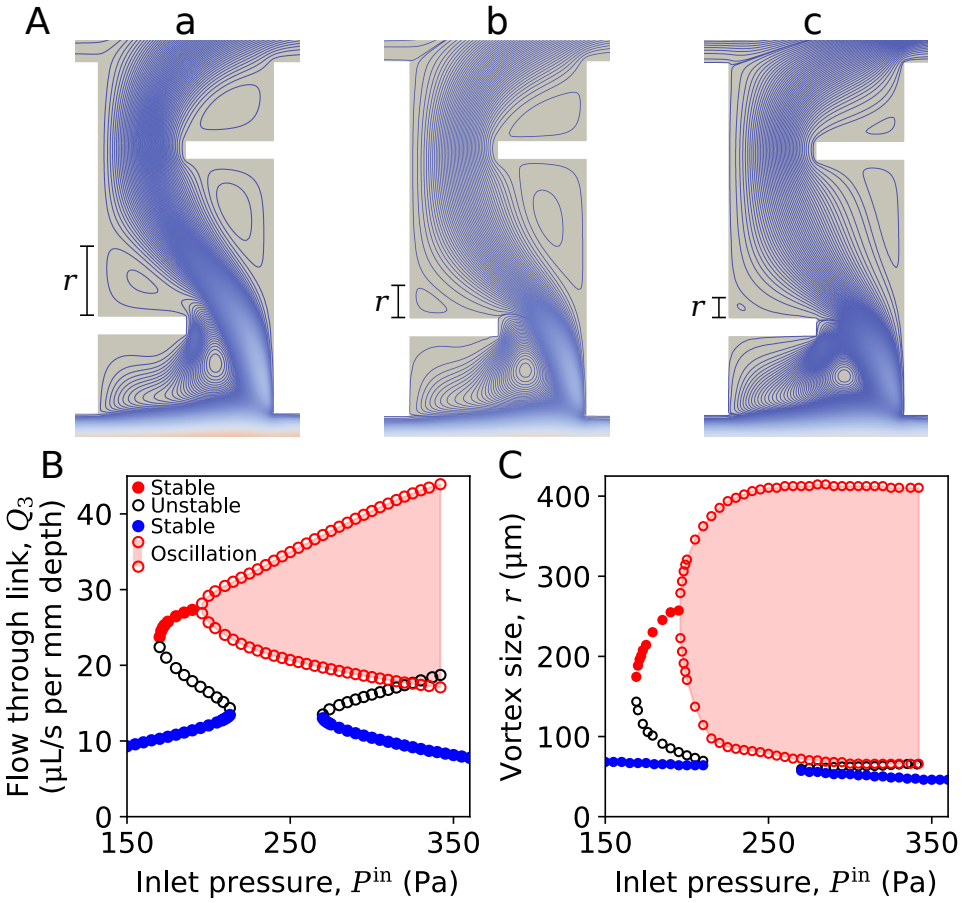

Figure 4.4. **Flow structure in chicane channel.** (**A**) Streamlines corresponding to the labeled solutions in Fig. 4.2A show variations in the vortices around the blade barriers. The size of one of the vortices is denoted by r. (**B-C**) Bifurcation diagrams for Q_3 (B) and r (C), corresponding to all simulation results presented in Fig. 4.2A.

nonlinear relations suggest a coupling between the pressure-flow relation of the chicane channel and the vortex size. Values for P_3 and P_4 in Fig. 4.5 were measured by averaging the pressure sampled across the channel width at a distance $3w/5$ downstream of the chicane channel junctions. We also note that discontinuities arise in the pressure-flow relation for the chicane channel (Fig. 4.5B) that result from abrupt changes in the vortex size as Q_2 is varied (Fig. 4.5A).

These discontinuities show the emergence of regions where the pressure-flow relation is negatively sloped, which compare to regions of negative differential resistance along current-voltage curves in electronics (further discussion provided in section 4.4).

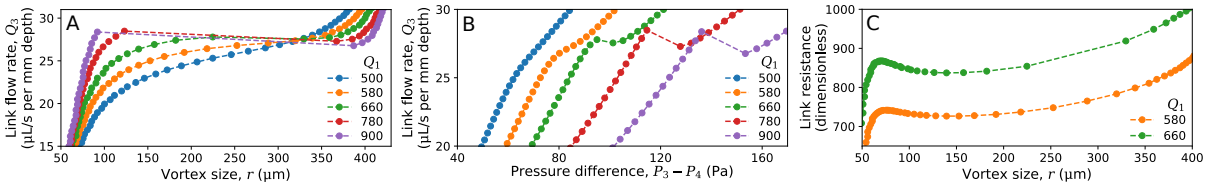

Figure 4.5. **Vortex-flow rate interaction.** (**A-C**) Navier-Stokes simulation results of the network in Fig. 4.1 for fixed values of Q_1 as Q_2 is increased, from which we determine the relation between Q_3 and r (A), the pressure-flow relation for the chicane channel (B), and the dependence of the chicane channel resistance on r (C). Transitions are evident at the points of discontinuity in (B), which can be associated with the points of discontinuity in Fig. 4.3, albeit for different control and independent variables. The pressures P_3 and P_4 are approximated from simulations by averaging pressure values sampled across the channel width near the chicane channel junctions. The chicane channel resistance is defined as $(P_3 - P_4)/Q_3$ and is non-dimensionalized by dividing it by μ/w^2.

4.3. Analytical dynamical model

We now construct an analytical model of the system in Fig. 4.1 that characterizes our simulation results. For unidirectional laminar flow through a straight channel, the general solution of the Navier-Stokes equations for an incompressible fluid can be approximated as

$$l\dot{Q} = \Delta P - RQ, \tag{4.1}$$

where the dot implies a time derivative and l may be referred to as the fluidic inductance [**22**]. For a two-dimensional channel of length L, explicit calculation of the fluidic resistance and inductance gives $R = 12\mu L/w^3$ and $l = \rho L/w$. While Eq. 4.1 is valid under unsteady conditions, it reduces to $\Delta P = RQ$ in the steady state.

One of the assumptions in the derivation of Eq. 4.1 is that all streamlines of the channel flow are straight, which causes the nonlinear inertial terms in the Navier-Stokes equations to vanish. Streamlines in the chicane channel clearly violate this assumption (Fig. 4.4A) and nonlinear effects are therefore expected to be present. Indeed, we observe an approximately quadratic relation between the chicane channel resistance, R_3, and the vortex size, r, for $60 < r < 400\,\mu$m (Fig. 4.5C). To construct an approximate dynamical equation for Q_3, we use the form of Eq. 4.1 with the constant resistance replaced by a function of r. Specifically, we take $R_3(r) = 12\mu(L_b + \gamma(r - r_b)^2)/w^3$, where L_b serves as a base component of the resistance, γ is a constant coefficient of the variable component that depends on the vortex size, and r_b is the vortex size that minimizes the resistance (from Fig. 4.5C, $r_b \approx 150\,\mu$m). With this added dependence on r, we must also account for the dynamics of the vortex size. The steady-state relation between Q_3 and r found through flow-controlled simulations (Fig. 4.5A) can be well fit by a cubic equation of the form $Q_3 - Q_3^* = \eta(r - r^*)^3 - \xi(r - r^*)$, where η and ξ are positive parameters and Q_3^* and r^* are constants that shift the cubic relation from the origin. For simplicity, we consider the growth rate of r to be proportional to the deviation from this equilibrium relation. Therefore, the dynamical equations that characterize the chicane channel

take the form

$$\dot{r} = \epsilon\big(Q_3 - Q_3^* - \eta(r - r^*)^3 + \xi(r - r^*)\big), \tag{4.2}$$

$$\dot{Q}_3 = \frac{w\Delta P_{34}}{\rho L_3} - \frac{12\nu}{w^2 L_3}\big(L_b + \gamma(r - r_b)^2\big)Q_3, \tag{4.3}$$

where ϵ is a positive constant. For suitable parameters, we find these equations capture the most salient properties in Fig. 4.4, B and C. We show in Fig. 4.6 that for different ΔP_{34}, Eqs. 4.2-4.3 can exhibit bistability and stable limit cycle solutions. We note that the additional dependence of the relations presented in Fig. 4.5 on Q_1 can be accounted for by allowing η and L_b to be functions of Q_1 (further details provided in section 4.5).

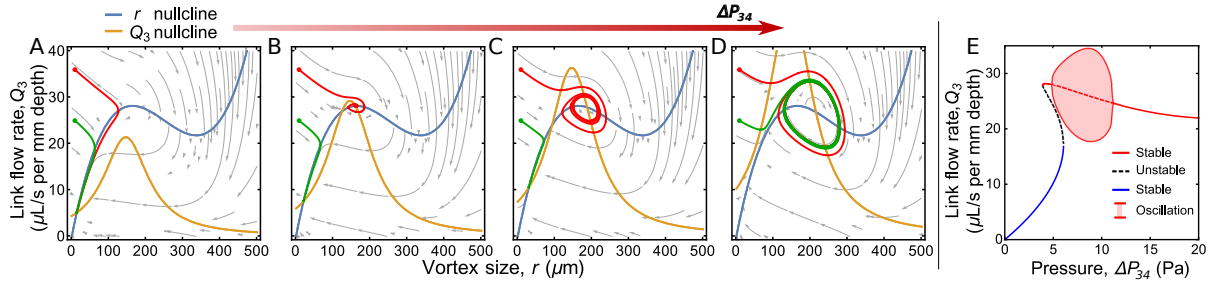

Figure 4.6. **Analytical dynamical model of flow through the chicane channel.** (**A-D**) Phase space plots showing example trajectories (red and green curves) and streamlines (grey curves), generated from Eqs. 4.2-4.3 for the flow rate and vortex dynamics at different values of ΔP_{34}. Fixed point solutions to the equations exist at the intersections of the r and Q_3 nullclines (i.e., the curves in phase space for which $\dot{r} = \dot{Q}_3 = 0$). The solution set may consist of one steady solution (A), three steady solutions (two stable, one unstable) (B), two steady solutions (one stable, one unstable) and a stable limit cycle (C), or a single stable limit cycle (D), depending on the value of ΔP_{34}. (**E**) Bifurcation diagram of Q_3 produced for Eqs. 4.2-4.3. The parameters used here are: $Q_3^* = 25\,\mu$L/s per mm depth, $r_b = 146\,\mu$m, $r^* = 250\,\mu$m, $L_b = 0.146$ cm, $\gamma = 0.264\,\mu\text{m}^{-1}$, $\epsilon = 4166$ m^{-1}.

A second nonlinear element of the network in Fig. 4.1 is the obstacle-laden channel. As the flow rate through this channel segment increases, stationary eddies form in the wake of the

obstacles for moderate Reynolds numbers. The presence of many of these obstacles in close proximity generates large velocity gradients in the surrounding flow, which amplifies energy dissipation and results in an overall nonlinear pressure-flow relation for steady flow through the channel. This equilibrium relation is well characterized by the Forchheimer equation used to describe steady flow through porous media, where inertial effects are significant even at very low flow rates [**70**]. The Forchheimer equation takes the form $\Delta P = \alpha\mu LV + \beta\rho LV^2$, where V is the average velocity, α is the reciprocal permeability, and β is the non-Darcy flow coefficient. The latter two parameters are solely dependent on the system geometry, and not on the working fluid. For our two-dimensional channel with obstacles, we take $V = Q_4/w$ so that the pressure-flow relation for the channel becomes $P_4 = \alpha\mu L_4 Q_4/w + \beta\rho L_4 Q_4^2/w^2$, where α and β are fit from simulations (further details provided in section 4.4 and Fig. 4.12). We account for this nonlinearity in a dynamical equation for Q_4 by using a flow-rate-dependent function in place of the constant resistance in Eq. 4.1. Specifically, we take $R_4(Q_4) = \alpha\mu L_4/w + \beta\rho L_4 Q_4/w^2$ so as to recover the Forchheimer equation in steady flow. A consequence of the nonlinearity of this channel is that it gives rise to a non-monotonic relation between the pressure difference across the chicane channel and P^{in}. As P^{in} is increased from zero, Q_3 initially increases, before decreasing, as indicated by the low-flow solution branch in Fig. 4.4B.

We now construct the dynamical model for the full network in Fig. 4.1 as follows: (i) we use flow relations of the form in Eq. 4.1 with constant resistances for the three channel segments without obstacles and with a flow rate dependent resistance function (discussed above) for the obstacle-laden channel; (ii) we use Eqs. 4.2-4.3 to describe the flow rate and vortex dynamics in the chicane channel with ΔP_{34} substituted by $(\zeta P_3 - P_4)$, where ζ is a free parameter that may deviate from 1 to account for an effective pressure difference across the chicane channel;

and (iii) we account for the most dominant minor pressure losses due to diverging flows at the channel junctions [**78**]. For the latter, we include terms of the form kQ_3Q_5/Q_1 in the flow equations for Q_3 and Q_5, where k is a positive constant. This leads to six ordinary differential equations (five for flow rates and one for the vortex size), which can be reduced to four equations by making use of the equations that account for flow rate conservation at the channel junctions: $Q_1 = Q_3 + Q_5$ and $Q_2 = Q_4 - Q_3$ (further details of the model are provided in section 4.5).

The model predictions of the total flow rate, chicane channel flow rate, and vortex size for the network in Fig. 4.1 under a common driving pressure at the inlets are presented in Fig. 4.7. The model captures well the complex solution structure observed in Figs. 4.2A and 4.4, B and C, shows strong quantitative agreement with simulations, and provides several interpretations for the observed flow behavior. First, spontaneous oscillations are found to arise through the transition from a fixed-point solution to a stable limit cycle via a supercritical Hopf bifurcation. The amplitude of the limit cycle grows with the driving pressure and eventually collides with the unstable solution surface of Q_3 and r, as shown in Fig. 4.7, thereby destabilizing the oscillating solution through a homoclinic bifurcation. Second, the nonlinearity arising from the Forchheimer effect gives rise to the two distinct bistable regions (and thus two negative conductance transitions), as a result of the non-monotonic relation between P^{in} and the pressure loss along the chicane channel. Third, the difference in the total flow rate between the solution branches is primarily determined by the minor losses. Without these terms, the model may still predict bistability, but the difference in total flow rate for solutions belonging to different branches would be negligible.

Our model can also be used to integrate the nonlinear behaviors described above into larger microfluidic systems. As an example, consider the extended network with three outlets in

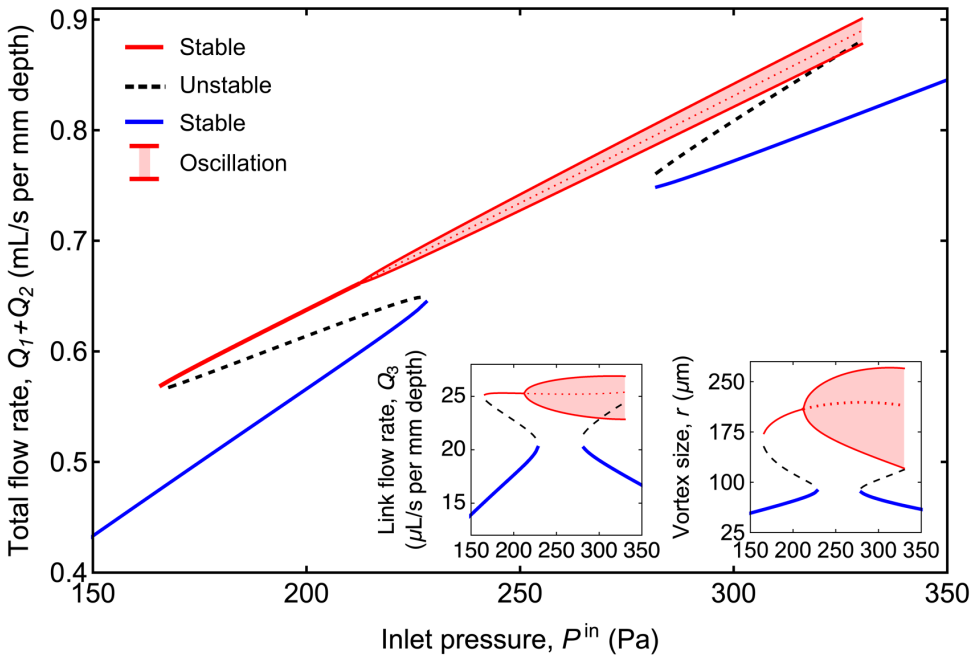

Figure 4.7. **Model predictions of network flow dynamics.** Bifurcation diagrams produced by our model for the total flow rate, flow rate through the chicane channel (left inset), and vortex size (right inset). Model parameters were fit to simulation results and are provided in section 4.5.

Fig. 4.8A, where the inlet flows are marked with different colors. By driving the flows through this network using a common pressure, three unique oscillatory flow compositions can be realized at the outlets. Figure 4.8B presents our model predictions, showing that the flow composition at the individual outlets is different but their flow rates oscillate in phase (further model details are provided in section 4.5). Thus, the property that flow rates through all channel segments oscillate with the same period can be extended to larger networks and used to produce synchronized, time-dependent output flow patterns.

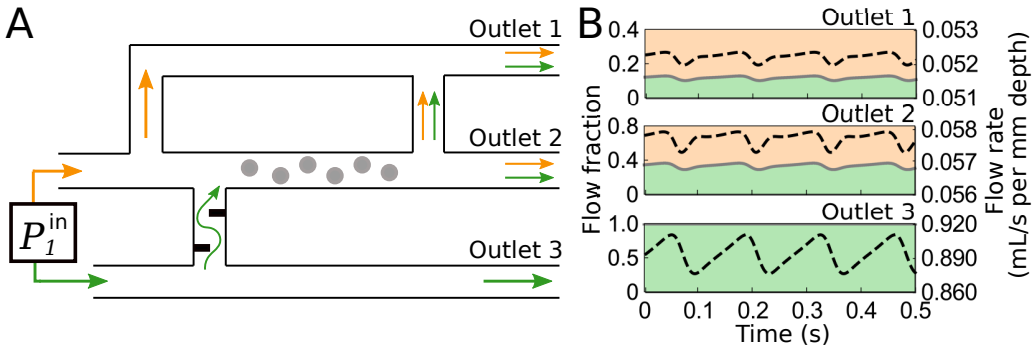

Figure 4.8. **Synchronous output patterns.** (**A**) Schematic of extended microfluidic network with three outlets, where inlet flows are marked orange and green, the inlet pressure is held fixed at $P_{\text{in}} = 350$ Pa, and the outlet pressure is held fixed at zero. (**B**) Model predictions for the network shown in (A), where the green areas show the portions of the flows that originate from the bottom inlet (left axis) and the dashed lines indicate the total flow rate through the respective outlet (right axis).

4.4. Extended results and discussion of direct fluid dynamics simulations

Flow controlled Navier-Stokes simulations. To show how multistability arises for pressure-driven flows through the network in Fig. 4.1, we present additional simulations in which pressure is controlled at one inlet (P_1^{in}), flow rate is controlled at the other inlet (Q_2), and the resulting value of P_2^{in} is measured. In Fig. 4.9, we show the relative difference between the inlet pressures for several examples in which P_1^{in} is fixed with Q_2 being varied. Points where this difference vanishes (i.e., crossings of the horizontal axis) indicate potential solutions for the case in which P_1^{in} and P_2^{in} are controlled to be equal. This is an indirect way of identifying both the stable and unstable solutions for the pressure controlled simulations since, by their very nature, the latter are not directly observable. Indeed, we see for low driving pressure (Fig. 4.9A) a single solution exists, and as the pressure is increased, two additional solutions emerge through a saddle-node bifurcation. The three solutions indicated by a, b, and c in Fig. 4.9B correspond to the labeled solutions in Bistable Region I in Fig. 4.2A. For a higher driving pressure (Fig. 4.9C),

the only indicated solution for which pressures at the inlets are equal occurs over a discontinuity and corresponds to a driving pressure in Fig. 4.2A that yields a single unsteady solution. For still higher pressures (Fig. 4.9D), multiple solutions reemerge and correspond to solutions within Bistable Region II in Fig. 4.2A. We determine the stability of all identified solutions by performing time-dependent simulations.

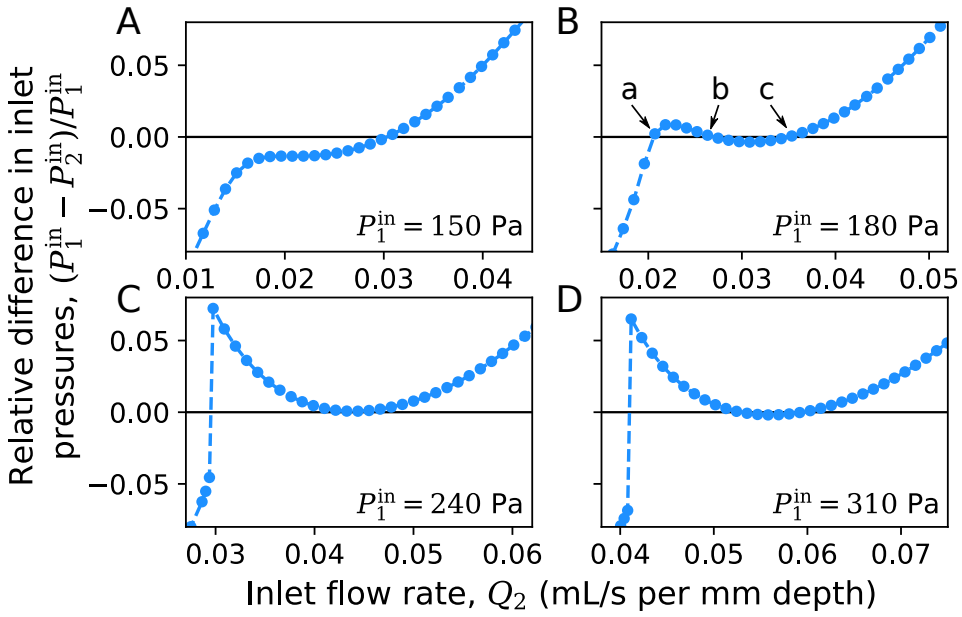

Figure 4.9. **Flow controlled Navier-Stokes simulations reveal bistability.** (**A - D**) Relative difference in inlet pressures of the network in Fig. 4.1 for fixed P_1^{in} with Q_2 varied. In accordance with the two bistable regions identified in Fig. 4.2A), the number of axis crossings, as P_1^{in} is fixed to higher values, varies between one (A and C) and three (B and D). The total flow rates corresponding to the solutions labeled in (B) are marked in Fig. 4.2A.

Flow rate and vortex oscillations. For unsteady solutions along the high-flow branch in Figs. 4.2A and 4.4, B and C, all variables (flow rates and vortex size) oscillate with the same period. The period of the oscillating solutions as a function of the driving pressure P^{in} is presented in Fig. 4.10. As the driving pressure approaches the value at which the unsteady solutions

become unstable, the period of the oscillations diverges, which is indicative of a homoclinic bifurcation, whereby the stable limit cycle collides with the unstable solution surface.

Example time series for the total flow rate, vortex size, and flow rate through the chicane channel are presented in Fig. 4.11 for two values of P^{in}. Two timescales are particularly evident in the oscillations of the flow rate through the chicane channel (Fig. 4.11, B and E) and the vortex size (Fig. 4.11, C and F), whereby a comparatively slow growth in each of these quantities is followed by a rapid decline. This is a typical characteristic of so called relaxation oscillations, first defined in the context of Van der Pol's equation [**95**]. As the amplitude of the oscillations in the flow rate grow along the high-flow solution branch so does the amplitude in the oscillations of the vortex size. For high enough driving pressures, the vortex vanishes for a very short time relative to its period, as shown in the time series of r in Fig. 4.11F. To better facilitate the visualization of the oscillation amplitude in Fig. 4.4C, the maximum amplitude value was taken to be the maximum value of r over one oscillation period at each driving pressure, while the minimum was taken to be the value of r at which the magnitude of dr/dt was minimized (other than at the extrema of r). This adjusted minimum represents the minimum vortex size outside of the the very short time range in which the vortex vanishes.

Negative differential resistance in the chicane channel. There are interesting parallels between the oscillations that arise in our system and those found in early work on electronic circuits. In particular, the well-known Van der Pol equation characterizes the oscillatory behavior observed in electronic circuits that incorporate a component with negative differential resistance [**95**]. Indeed, evidence of negative differential resistance exists for the chicane channel in our system (Fig. 4.5B) and is characterized by the negatively sloped region in Fig. 4.6E, which also corresponds to the region where oscillations arise. Moreover, extensions of the Van der

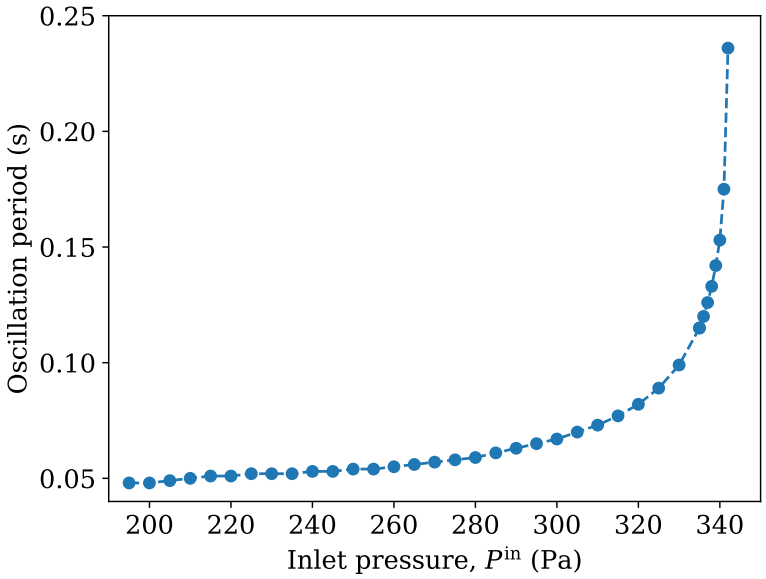

Figure 4.10. **Divergence of oscillation period.** Period of oscillation of unsteady solutions along the high-flow branch in Fig. 4.2A for different values of P^{in}. The dots represent the results from Navier-Stokes simulations, and the interpolating dashed line is a guide to the eye.

Pol equation, through the addition of nonlinear terms, have been shown to describe dynamics similar to those observed in our network in chemical reaction networks [**96**].

4.5. Dynamical model of microfluidic network

The model describing flows through the network in Fig. 4.1 is based on Eqs. 4.1-4.3. For the flow equations of Q_1, Q_2, and Q_5, we use the form in Eq. 4.1, where the resistances take the standard form for a two-dimensional channel, $12\mu L_i/w^3$. The corresponding length of each of channel segment is labeled in Fig. 4.1D. Below we present the complete dynamical model, which incorporates nonlinear terms that account for inertial effects in the flow around obstacles and minor losses.

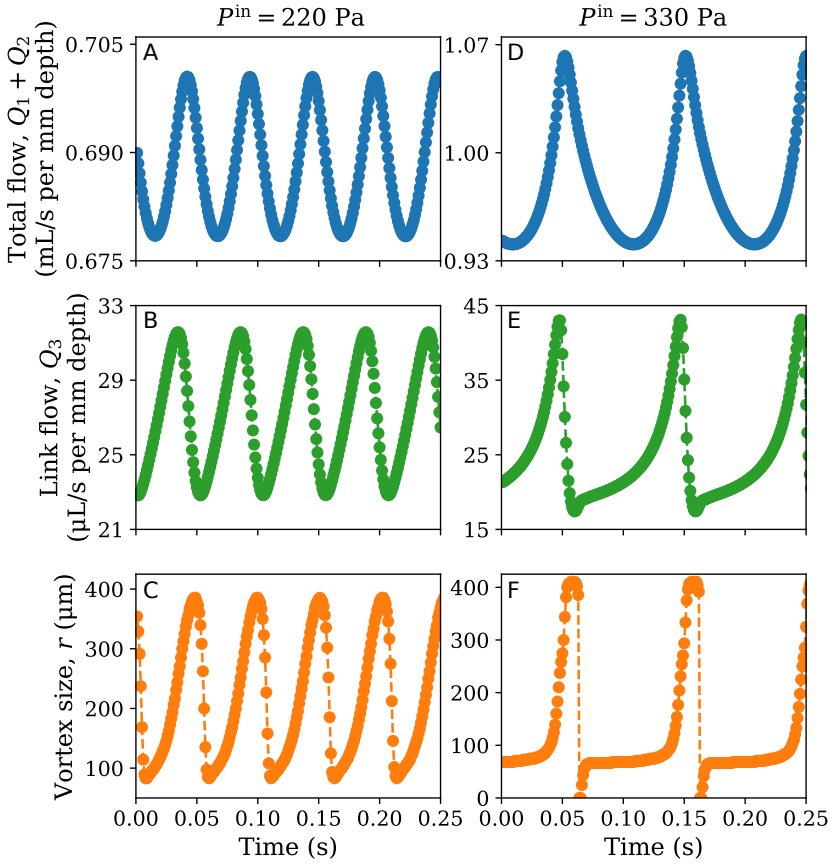

Figure 4.11. **Example time series of oscillating solutions determined by Navier-Stokes simulations.** (**A** and **D**) Oscillations in the total flow rate, (**B** and **E**) flow rate through the chicane channel, and (**C** and **F**) vortex size for two different fixed driving pressures, $P^{\text{in}} = 220\,\text{Pa}$ (A-C) and $P^{\text{in}} = 330\,\text{Pa}$ (D-F). The symbols represent measurements from direct fluid dynamic simulations, sampled uniformly in time, and the interpolating line is used to guide the eye.

Chicane channel flow and vortex dynamics. To characterize the flow rate through the chicane channel, we use Eqs. 4.2-4.3, which couple the pressure-flow relation and vortex dynamics. We account for the additional dependence of Eq. 4.2 on Q_1, as observed in Fig. 4.5A, by allowing η to be a function of Q_1. To keep the model simple, we define

$$\eta(Q_1) = p + q\,Q_1, \tag{4.4}$$

where p and q are constants. Further, we set

$$\xi = \frac{(r^*)^2\eta - Q^*}{r^*}, \tag{4.5}$$

which ensures that $r = 0$ for $Q_3 = 0$, corresponding to the physical requirement that the vortex vanishes as the flow rate goes to zero.

The pressure drop ΔP_{34} in Eq. 4.3 corresponds to the pressure loss along the chicane channel. This loss is approximately equal to $P_3 - P_4$ (Fig. 4.1A). However, the pressure field can vary significantly over short distances at the channel junctions. To account for this effect, as well as the fact that the chicane channel has a comparatively wide width and short length, we define the effective pressure drop as $\zeta P_3 - P_4$, where ζ is a constant expected to be near one. We also note that the measured resistance of the chicane channel (Fig. 4.5C) also shows dependence on Q_1. This can be included in the model by allowing L_b in Eq. 4.3 to vary with Q_1, but this modification did not present marked differences in the model prediction, so we chose not to include it here.

Flow through obstacle-laden channel. The channel with flow rate Q_4 contains six cylindrical obstacles. For steady flow, the pressure-flow relation is well-characterized by the Forchheimer equation, whereby the pressure loss along the channel depends quadratically on the flow rate. The steady pressure-flow relation takes the form

$$\Delta P = \frac{\alpha\mu L}{w}Q + \frac{\beta\rho L}{w^2}Q^2. \tag{4.6}$$

In Fig. 4.12, we show that our simulation results conform to this equation for the isolated obstacle-laden channel. The observed linear relation between Q and $\Delta P/Q$ with non-zero slope indicates an approximately quadratic relation between Q and ΔP. This nonlinearity arises as a

result of large velocity gradients and eddies that form in the wakes of the obstacles as the flow rate is increased, which thereby alters the fluidic resistance of the channel. Therefore, we approximate the dynamic flow rate relation for Q_4 by using Eq. 4.1 with the resistance R replaced by the flow-rate-dependent expression $R_4(Q_4) = \alpha\mu L_4/w + \beta\rho L_4 Q_4/w^2$.

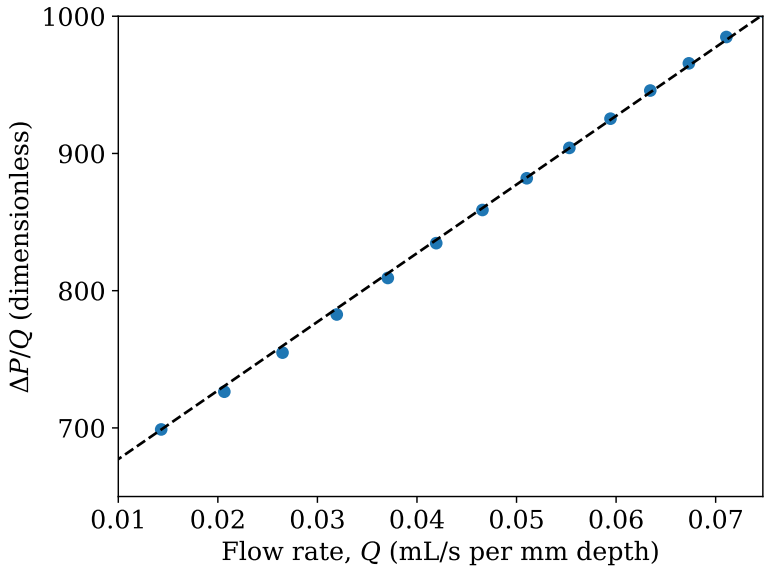

Figure 4.12. **Nonlinear flow through channel with obstacles.** The Navier-Stokes simulation results (symbols) show the relation between the fluidic resistance, $\Delta P/Q$, and the flow rate, Q, for a channel with six cylindrical obstacles. The linear fit (dashed line) confirms that ΔP is well approximated by Eq. 4.6. The channel length is $1\,\text{cm}$, and the fitted values of α and β are $1.24 \times 10^{-8}\,\text{m}^{-2}$ and $513\,\text{m}^{-1}$, respectively. The resistance is non-dimensionalized by dividing it by μ/w^2.

Minor losses at channel junctions. The Reynolds numbers of the flows through the system are up to the order of 100 for the chicane and obstacle-laden channels and 1000 for obstacle-free channels. Given that nonlinearity arises in the pressure-flow relations for different channels, fluid inertia effects are clearly significant. Therefore, additional pressure losses in areas where streamlines combine, diverge, or bend—so called minor losses—should be considered. The

flow rates Q_1 and Q_5 are an order of magnitude higher than elsewhere in the network since the absence of obstacles in the associated channels yield low fluidic resistances. As a result, the most dominant minor losses are expected to occur at the junction of Q_1, Q_3, and Q_5. Minor loss terms are typically found empirically for different geometries, and at flow junctions they generally take the form of a scaling factor that depends on the flow rate with a coefficient that is a function of the ratio of diverging flows (36). The scaling factor and coefficient can each be nonlinear, in principle, but for our model we use the simple expression kQ_3Q_5/Q_1, where k is a constant. A term of this form is included in the flow rate equation for Q_3 and Q_5, with independent values of k.

Non-dimensional model equations. Our model of the microfluidic network in Fig. 4.1 is constructed from equations describing each component of the network and includes terms that account for interactions between components, as described in the preceding sections. The variables and parameters in the model can be non-dimensionalized using the following definitions:

(4.7)

$$\overline{P} = \frac{P}{\rho\nu^2/w^2};\ \overline{Q} = \frac{Q}{\nu};\ \overline{L} = 12\frac{L}{w};\ \overline{r} = 12\frac{r}{w};\ \overline{\gamma} = \frac{\gamma w}{12};\ \overline{t} = t\frac{\nu}{w^2};$$

$$\overline{\eta} = \frac{\eta}{\nu}\left(\frac{w}{12}\right)^3;\ \overline{p} = \frac{p}{\nu}\left(\frac{w}{12}\right)^3;\ \overline{q} = q\left(\frac{w}{12}\right)^3;\ \overline{\xi} = \xi\frac{w}{12\nu};\ \overline{\alpha} = w^2\alpha, \overline{\beta} = w\beta;\ \overline{\epsilon} = 12w\epsilon;$$

where t indicates time and $\nu = \mu/\rho$ is the kinematic viscosity.

The complete set of non-dimensional equations that define the model read:

$$\dot{Q}_1 = 12\left(\frac{P_1^{\rm in} - P_3}{L_1} - Q_1\right), \tag{4.8}$$

$$\dot{Q}_2 = 12\left(\frac{P_2^{\rm in} - P_4}{L_2} - Q_2\right), \tag{4.9}$$

$$\dot{Q}_3 = 12\left(\frac{\zeta P_3 - P_4}{L_3} - \frac{1}{L_3}\big(L_{\rm b} + \gamma(r - r_b)^2\big)Q_3 + k_3\Big(\frac{Q_5}{Q_1}\Big)Q_3\right), \tag{4.10}$$

$$\dot{Q}_4 = 12\left(\frac{P_4}{L_4} - \frac{1}{12}(\alpha + \beta Q_4)Q_4\right), \tag{4.11}$$

$$\dot{Q}_5 = 12\left(\frac{P_3}{L_5} - Q_5 + k_5\Big(\frac{Q_3}{Q_1}\Big)Q_5\right), \tag{4.12}$$

$$\dot{r} = \epsilon\big((Q_3 - Q_3^*) - \eta(Q_1)(r - r^*)^3 + \xi(r - r^*)\big), \tag{4.13}$$

$$Q_1 = Q_3 + Q_5, \tag{4.14}$$

$$Q_2 = Q_4 - Q_3, \tag{4.15}$$

where the bars over non-dimensional quantities are omitted for brevity.

For $\eta(Q_1)$ and ξ in Eq. 4.13, we use non-dimensionalized forms of Eqs. 4.4-4.5. In view of Eqs. 4.14-4.15, the model can be reduced to only four equations for the variable Q_1, Q_2, Q_3, and r, which we use for the predictions presented in Fig. 4.7.

Model parameters. The undeclared parameter values we use for the model predictions in Fig. 4.7 are as follows. For the channel width and lengths, as labeled in Fig. 4.1D, we use the same values as in the simulations. The fitted values of α and β are declared in the caption of

Fig. 4.12. The remaining non-dimensional parameters are:

$$\begin{aligned} \zeta = 1.08,\ \overline{L}_b = 42,\ \overline{\gamma} = 7.35,\ \overline{r}_b = 4.1,\ \overline{r}^* = 5.5,\ \overline{\epsilon} = 10.9, \\ \overline{k}_3 = 15.75,\ \overline{k}_5 = 12,\ \overline{Q}_3^* = 25,\ \overline{p} = 0.12,\ \overline{q} = 0.8 \times 10^{-5}, \end{aligned} \tag{4.16}$$

where $\overline{p}$ and $\overline{q}$ are used in the non-dimensional form of Eq. 4.4.

Three-outlet network in Fig. 4.8. In Fig. 4.8 we demonstrated how different output flow patterns can be generated in an expanded version of the network in Fig. 4.1. Specifically, we consider the scenario in which three additional channel segments without obstacles are incorporated into the network described in Fig. 4.1, resulting in a system with three outlets (Fig. 4.8A). A schematic of the three-outlet network is presented in Fig. 4.13. The predictions of the outlet flows for this network, presented in Fig. 4.8B, are derived from a dynamic model constructed in the same manner as in Eqs. 4.8-4.15. The model consists of ten flow rate equations (one for each channel segment), five flow-rate conservation equations, and one equation for the vortex dynamics. Aside from the channel segment lengths, all parameter values used are the same as in Eq. 4.16. The channel segment lengths used for the prediction in Fig. 4.8B and corresponding to the labels in Fig. 4.13 are: $L_1 = 0.1035$, $L_2 = 0.3$, $L_3 = 0.1$, $L_4 = 10.0$, $L_5 = 0.3$, $L_6 = 1.0$, $L_7 = 0.45$, $L_8 = 0.1$, $L_9 = 0.02$, $L_{10} = 0.05$, all in cm. Finally, the driving pressure used was $P_{\text{in}} = 350$ Pa, which yielded oscillating flows throughout the network.

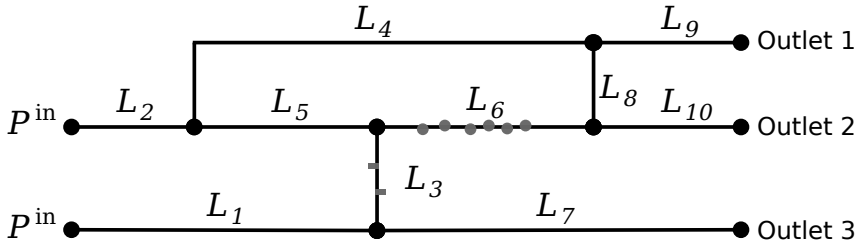

Figure 4.13. **Network schematic of three-outlet system in Fig. 4.8A.** The length of each channel segment is denoted by L_i.

4.6. Discussion

A recurrent question in the study of microfluidics is the extent to which they should mimic electronic circuits. A fundamental aspect of microelectronics is its doubly integrated nature—characterized by both the fabrication and operation of controllers on chip—as well as its non-reliance on movable components—which sets it apart from macroelectronics. Here, motivated by the challenge of developing built-in controls in microfluidics, we identified mechanisms that can facilitate integration without dependence on movable parts or external actuation (other than through the working flow). This includes our demonstration of self-sustained oscillations, which can be used for timing and synchronization of logic gates, multistability and associated transitions, which can be used for signal amplification and switching, and hysteresis, which serve as a possible mechanism for memory. In particular, we demonstrated the emergence of spontaneous periodic variations in the relative uptake rates from different inlets, which can be explored to generate time-dependent mixtures and output flow patterns. However, these dynamical behaviors rely on effects that do not have direct analogs in microelectronics, namely fluid inertia and the resulting nonlinearity arising from interactions between components.

Our results demonstrate that fluid inertia effects can be amplified and induce behaviors in fixed-structure microfluidic systems that have not been previously generated without external actuation. Indeed, the negative conductance transitions, spontaneous oscillations, hysteresis, and multistability simulated and modeled in our system all emerge as a consequence of coupling between the geometric structure of the network and fluid inertia effects Flows around obstacles and through the porous-like channel is determinant for generating these dynamics; porous media microfluidics have become important for the study of flows through natural systems as well as systems engineered for specific functions [**97**], such as the control of viscous fingering [**98**]. In this work, we placed new emphasis on the viability of porous-like structures to serve as nonlinear elements that are analogous to nonlinear resistors in electronics. Our approach contrasts with microfluidic networks designed in direct analogy with simple electronic circuits, where the connections between components only translate to linear algebraic flow-rate conservation equations [**22, 17, 18**]. It is also instructive to note that previous work on inertial microfluidics was primarily focused on the local manipulation of flows or particles, whereas this study proposes systems that harness fluid inertia effects for non-local flow control throughout the network, which, crucially, can be realized as a built-in mechanism. Given that our system can be constructed from rigid materials, it is able to withstand a wide range of driving pressures (e.g., $1\,\text{Pa}$–10^6 Pa), which facilitates implementation across the length scales relevant to microfluidics.

The flow dynamics that arise in our system can be tailored for various applications. Microfluidic systems capable carrying out sequential operations generally require a timing mechanism that is either generated from an external device or through the use of flexible valves [**54**].

The oscillations that arise in our system could serve as an on-chip frequency reference and enable process synchronization or waveform synthesis. Moreover, the vortex dynamics that give rise to the oscillations may be used to enhance state-of-the-art methods for particle sorting and manipulation that function through interactions between particles and micro-vortices [**99**]. In particular, vortex dynamics can be used to produce complex (and even chaotic) particle trajectories in laminar flows [**100, 101**], which is a property exploited in proposed microfluidic applications to cryptography [**102**]. Finally, microfluidic networks are now widely used in the study of colloids [**103, 104**] and active matter [**105, 106**]. Our system offers a rich environment to further investigate these materials given that they exhibit surprising collective behavior when placed in different flow fields [**107**] and when driven through porous media [**108**].

Moving forward, we envision a shift in the design of microfluidic systems towards networks that exhibit dynamical behaviors analogous to those of microelectronics, even if generated through very different mechanisms. In particular, the coupling of inertial effects and network geometry can be explored in diverse microfluidic applications to implement preprogrammed functionality, such as the generation of prespecified oscillation or output patterns at specific driving pressures.

CHAPTER 5

Levitation of heavy particles in asymptotically downward flows

In the fluid transport of particles, it is generally expected that heavy particles carried by a laminar fluid flow moving downward will also move downward. We establish a theory to show, however, that particles can be dynamically levitated and lifted by interacting vortices in such flows, thereby moving against gravity and the asymptotic direction of the flow, even when they are orders of magnitude denser than the fluid. The particle levitation is rigorously demonstrated for potential flows and supported by simulations for viscous flows. We suggest that this counterintuitive effect has potential implications for the air-transport of water droplets and the lifting of sediments in water. This research was conducted in collaboration with Jean-Régis Angilella (first author) and Adilson E. Motter [**109**].

5.1. Motivation

Many natural and industrial flows transport small particles, like droplets, sediments, and microorganisms [**32**]. Inertial effects cause the trajectories of such particles to deviate from the streamlines of the flow, making the study of particle-laden flows challenging both theoretically and experimentally [**110, 111, 112, 113**]. Key to such studies are the dissipative nature of the advection dynamics and the consequent tendency of the particles to accumulate in specific zones of the flow domain, both in closed flows [**114, 115, 116, 117, 118, 119, 120, 121, 122, 123, 122, 124**] and in open flows [**125, 126, 127, 128, 129**], even when the flows are incompressible. For example, particles less dense than the fluid tend to be attracted to the interior of vortices

[**130, 131**], which can lead to the formation of attractors for the particle dynamics independently of the global properties of flow. Particles denser than the fluid, on the other hand, tend to be repelled by vortices, which is a mechanism that can lead to the formation of attractors if the flow is closed; this effect, which is also related to the preferential trajectories phenomenon [**116**], has been widely investigated over the past two decades [**110**]. However, much less is known about dense particles moving in flows that have unbounded streamlines and are therefore open. In open flows, an outstanding problem of particular interest concerns the transport of small particles much denser than the fluid, which we term *heavy particles* and which can represent for example water droplets in the air.

In this article, we demonstrate the possibility of levitation and upward transport of heavy particles by a flow moving asymptotically downward, even in the presence of gravity. Because at first these conditions seem to facilitate downward advection, one might expect that all particles would necessarily fall, which is in sharp contrast with the effect we report. The starting point of our analysis is the observation that such a flow can support pairs of mutually interacting vortices traveling in a direction that opposes the flow. We thus focus on asymptotically simple flows that move downward and have a pair of vortices moving upward. Using this class of flows we show that *attracting points* (dimension-zero attractors) formed near the center of vorticity can capture heavy particles released at any distance above the vortices. For this to occur, particle inertia must allow for particles to approach the vortices and for the existence of attractors to retain them in that region; we show that these two conditions are satisfied for a wide range of Stokes number in the class of flows we consider. This is demonstrated analytically using asymptotic analysis and Melnikov functions, and is illustrated numerically using simulations in both inviscid and viscous laminar flows.

Our analysis is inspired by previous experimental realizations of flows with pairs of interacting vortices [**132, 133, 134, 135, 136**] and theoretical work on particle advection in such flows [**127, 121, 123, 129, 124, 137, 138, 139, 140**]. Several studies have shown, both numerically [**127**] and analytically [**121, 123, 129**], the formation of attractors for the dynamics of heavy particles in the vicinity of identical co-rotating vortices. Different work has shown that such attractors persist for non-identical vortices in closed potential flows in the absence of gravity [**124**], but no results exist for open flows, viscous regimes, or the effects of gravity. Here, in order to demonstrate the proposed levitation of heavy particles, we first generalize the special results in open flows, previously established for nongeneric vortex pairs, to the case of (i) generic pairs of both co-rotating and counter-rotating vortices of arbitrary vortex strength ratio, (ii) for vortices moving against a background flow that is co-directional with gravity, and (iii) for both potential and viscous flows. Under these general conditions we then show the existence of attracting points that capture heavy particles from both the closed and open flow regions and carry them against gravity and the background flow.

5.2. Theoretical model

The model flow is depicted in Fig. 5.1. It consists of two vortices, A and B, with strengths Γ_A and Γ_B, respectively, plus mirror vortices A' and B' with opposite strengths and symmetric positions with respect to the vertical axis Oz. This axis can be regarded as a "wall" in the framework of potential flow theory used in our calculations. The position $\mathbf{r}_I$ of the center of vorticity I of the pair (A, B) is $\mathbf{r}_I = (\Gamma_A \mathbf{r}_A + \Gamma_B \mathbf{r}_B)/(\Gamma_A + \Gamma_B)$, where $\mathbf{r}_A$ is the position of A and $\mathbf{r}_B$ is the position of B. In the absence of mirror vortices, point I remains fixed and AB rotates steadily around I with angular velocity $\Omega_0 = (\Gamma_A + \Gamma_B)/(8\pi d_0^2)$, where $2d_0 = |AB|$

is the distance between the vortices, which remains constant in this case. When the two pairs (A, B) and (A', B') are close enough to interact, elementary vortex dynamics show that point I moves vertically, and its distance to the symmetry axis Oz remains equal to its initial value, L_0. For $d_0 \ll L_0$, the (vertical) velocity of I approaches $w_0 = (\Gamma_A + \Gamma_B)/4\pi L_0$ in the frame of the fluid at infinity. The streamfunction of the exact 2D potential flow induced by the four vortices, in the frame translating at constant speed $w_0\,\hat{\mathbf{z}}$, where $\hat{\mathbf{z}}$ is the upward unit vector, is

$$\psi(\mathbf{r}, t) = \frac{\Gamma_A}{4\pi} \ln \frac{|\mathbf{r} - \bar{\mathbf{r}}_A|^2}{|\mathbf{r} - \mathbf{r}_A|^2} + \frac{\Gamma_B}{4\pi} \ln \frac{|\mathbf{r} - \bar{\mathbf{r}}_B|^2}{|\mathbf{r} - \mathbf{r}_B|^2} + w_0\, y, \tag{5.1}$$

where $\mathbf{r} = (y, z)$, and $\bar{\mathbf{r}}_A$ and $\bar{\mathbf{r}}_B$ are the positions of the mirror vortices A' and B', respectively. The instantaneous velocity of fluid elements in this frame trace closed streamlines near the vortices (*closed flow* region) and open streamlines further away from them (*open flow* region). As indicated in Fig. 5.1, these two regions meet along the separatrix streamline Σ joining the stagnation points located on the z-axis, S_1 and S_2. The structure formed by $\Sigma \cup S_2S_1$ is a heteroclinic cycle for the dynamics of fluid elements; heteroclinic (and homoclinic) cycles are generally expected to play a role in the transport of both non-inertial and inertial particles [**141, 110**].

To proceed, we define $\gamma = \Gamma_A/\Gamma_B$ as the vortex strength ratio, where $-1 < \gamma \leq 1$. It can be checked that up to order ε^2, when $\varepsilon \equiv d_0/L_0 < (\gamma + 1)/2$, A and B rotate around I approximately as a rigid body with angular velocity Ω_0. This allows us to write $\mathbf{r}_{A,B}(t)$ and $\bar{\mathbf{r}}_{A,B}(t)$ in the form of $2\pi/\Omega_0$-periodic functions plus $O(\varepsilon^2)$ corrections. Throughout the rest of the article we operate with the equations in non-dimensional form, using as units L_0 for lengths and $w_0/2$ for velocities since these choices capture the appropriate orders of magnitude for the flow near the heteroclinic cycle Σ. (No new notation is introduced for non-dimensional

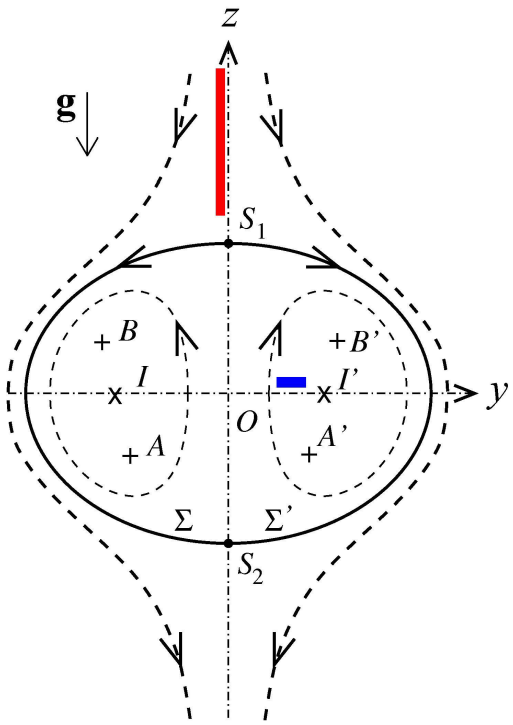

Figure 5.1. Sketch of the flow: vortices A and B and their mirrors together with typical streamlines (dashed lines) in the reference frame of the centers of vorticity I and I'. The flow along the open streamlines moves downward—the orientation of the gravitational field, $\mathbf{g}$. Also shown is where the particles are initiated (with the velocity of the flow) in the potential flow simulations below: blue and red particles are released in the closed and open regions of the flow, respectively.

variables.) Expanding Eq. (5.1) in powers of ε, in non-dimensional form the streamfunction reads

$$\psi(\mathbf{r},t)=\psi_0(\mathbf{r})+\frac{4\gamma\varepsilon^2}{(1+\gamma)^2}\Big[\psi_{2c}(\mathbf{r})\cos\frac{2t}{\varepsilon^2}+\psi_{2s}(\mathbf{r})\sin\frac{2t}{\varepsilon^2}\Big] \tag{5.2}$$

plus $O(\varepsilon^3)$ terms, where the components ψ_0, ψ_{2c}, ψ_{2s} are identical to those for the case $\gamma = 1$ [**142**] given that the γ-dependence is accounted for by the prefactor. The remainder in Eq. (5.2) can be shown to be $O(\varepsilon^4)$ when $\gamma = 1$. The velocity field—defined as $\mathbf{u} = \nabla \times (\psi\,\hat{\mathbf{x}})$,

where $\hat{\mathbf{x}}$ is the right handed unit vector orthogonal to the yz plane—is therefore of the form $\mathbf{u}(\mathbf{r},t) = \mathbf{u}_0(\mathbf{r}) + \varepsilon^2 \mathbf{u}_2(\mathbf{r}, t/\varepsilon^2; \gamma) + O(\varepsilon^3)$, where $\mathbf{u}_2$ is time-periodic with period $T = \pi\varepsilon^2$ and corresponds to the leading perturbation induced by the rotation of the vortices.

The components ψ_0, ψ_{2c}, and ψ_{2s} of the steamfunction in Eq. (5.2) read

$$\psi_0(\mathbf{r}) = \ln \frac{[z^2 + (y-1)^2]^2}{[z^2 + (y+1)^2]^2} + 2y, \tag{5.3}$$

$$\psi_{2c}(\mathbf{r}) = -8y \frac{\left[3\,z^4 - (-1+y^2)^2 + 2\,z^2\,(1+y^2)\right]}{\left[z^2 + (1+y)^2\right]^2 \left[z^2 + (1-y)^2\right]^2}, \tag{5.4}$$

$$\psi_{2s}(\mathbf{r}) = -8yz \frac{[-3 + z^4 + 2\,y^2 + y^4 + 2\,z^2\,(-1+y^2)]}{\left[z^2 + (1+y)^2\right]^2 \left[z^2 + (1-y)^2\right]^2}, \tag{5.5}$$

where $\mathbf{r} = (y, z)$ (as indicated in Fig. 5.1).

Having established the fluid flow equations, we now write the particle equation of motion in this flow. For a heavy particle with small particle Reynolds number, the non-dimensional equation is $\ddot{\mathbf{r}} = \widetilde{\mathrm{St}}^{-1} \left[\mathbf{u}(\mathbf{r},t) + \widetilde{\mathbf{V}}_T - \dot{\mathbf{r}}\right]$, where $\mathbf{r}$ is the particle position, $\widetilde{\mathbf{V}}_T = -\widetilde{V}_T \hat{\mathbf{z}} = -2(g\,\tau_p/w_0)\hat{\mathbf{z}}$ is the free-fall terminal velocity, and $\widetilde{\mathrm{St}}$ is the Stokes number (i.e., the response time of the particle, τ_p, divided by the time-scale of the flow, $2L_0/w_0$) [**143**]. We also introduce another Stokes number, $\mathrm{St} = \Omega_0\,\tau_p$, to describe the dynamics of particles directly influenced by the rotation of the vortices around each other. The formation of attractors near the vortices requires that St be no larger than order one since drag has to balance centrifugal force in this case. We therefore assume $\mathrm{St} = O(1)$, so that $\widetilde{\mathrm{St}} \equiv \varepsilon^2 \mathrm{St} \ll 1$ and the equation for $\mathbf{r}$ can be reduced to

$$\dot{\mathbf{r}} = \mathbf{v}_0(\mathbf{r}) + \varepsilon^2 \mathbf{v}_2(\mathbf{r}, t/\varepsilon^2; \gamma) + O(\varepsilon^3), \tag{5.6}$$

where $\mathbf{v}_0(\mathbf{r}) = \mathbf{u}_0(\mathbf{r}) + \widetilde{\mathbf{V}}_T$ and $\mathbf{v}_2(\mathbf{r}, \tau; \gamma) \simeq \mathbf{u}_2(\mathbf{r}, \tau; \gamma) - \mathrm{St}\big[(\mathbf{u}_0 + \widetilde{\mathbf{V}}_T).\nabla \mathbf{u}_0 + \partial \mathbf{u}_2(\mathbf{r}, \tau; \gamma)/\partial \tau\big]$, for $\tau = t/\varepsilon^2$ (see also Ref. [**144**]). We show that the particle dynamics described by this equation have at least one (for $-1 < \gamma \leq 1$) and possibly two attracting points (for $0 < \gamma \leq 1$), provided that the Stokes number is not too large.

In Eq. (5.6), the leading term, $\mathbf{v}_0$, represents the conservative dynamics of non-inertial particles in a steady flow induced by the equivalent to a single vortex with strength $\Gamma_A + \Gamma_B$ (together with its mirror) plus a uniform flow $-\widetilde{V}_T \hat{\mathbf{z}}$. The particle streamfunction for this term, $\psi_p(y, z) = \psi_0(y, z) + y\widetilde{V}_T$, is time-independent (a similar streamfunction has been used to describe plankton dynamics [**145**]). The first perturbative term, $\varepsilon^2 \mathbf{v}_2$, contains the contribution $\mathbf{u}_2$ of the unsteadiness of the flow due to the fact that for $\varepsilon > 0$ there are two vortices rather than one, and also the effect of inertia in the St terms. It is thus convenient to regard this system as a time-independent Hamiltonian ψ_p perturbed by dissipative and fast periodic terms [**146**]. To leading order in ε, the trajectories of the particles coincide with the curves $\psi_p(y, z) = cte$. These curves correspond to open streamlines separated from closed streamlines by a heteroclinic cycle, which we denote Σ_p and which is the particle analog of Σ in Fig. 5.1 except that Σ_p does not include the time-dependent perturbation terms.

An important necessary condition for particles from the open flow to be captured by attracting points in the vicinity of the vortices is that they cross Σ_p (the separatrix of the unperturbed dynamics) under the effect of the motion of the vortices. The occurrence of separatrix crossing can be predicted employing a construction based on separatrix maps [**147, 148**]. We consider a solution $\mathbf{r}(t)$ of the perturbed system (up to order ε^2) and define t_n $(n = 1, 2, ...)$ as the times at which the particle crosses the axis Oy downward. We also use τ_{2n} and τ_{2n+1} to denote the times the particle passes closest to the saddle points S_1 and S_2, respectively, and $H_n = \psi_p[\mathbf{r}(\tau_{2n})]$

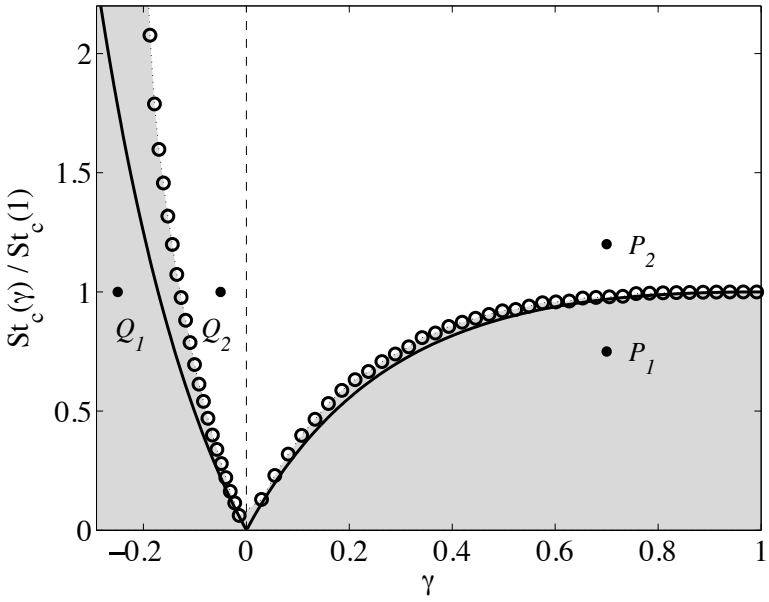

Figure 5.2. Normalized critical Stokes number for arbitrary vortex strength ratio, γ. Circles represent simulations for $\widetilde{V}_T = 0.1$ and $\varepsilon = 0.35$, whereas solid lines represent the theoretical prediction in Eq. (5.10). Particles released in the open flow with St in the shaded area may cross Σ_p and hence be levitated, while those above it cannot.

and $H_{n+1} = \psi_p[\mathbf{r}(\tau_{2n+1})]$ to denote the corresponding values of the unperturbed Hamiltonian. Oscillations of $H_{n+1} - H_n$ around zero as n varies will indicate that the separatrix Σ_p is crossed. Assuming that $\mathbf{r}(t) \simeq \mathbf{q}(t - t_n)$, for $\mathbf{q}(t)$ denoting the solution of the unperturbed system along Σ_p, we obtain

$$H_{n+1} - H_n \simeq \varepsilon^2 M(t_n), \tag{5.7}$$

where $M(t_n)$ is the Melnikov function associated with Σ_p:

$$M(t_n) = \frac{4\gamma(a + \widetilde{V}_T b)}{(1+\gamma)^2}\Big[\sin\frac{2t_n}{\varepsilon^2} - 2\mathrm{St}\cos\frac{2t_n}{\varepsilon^2}\Big] - m\,\mathrm{St} \tag{5.8}$$

Here, the amplitudes $a = a(\varepsilon)$ and $b = b(\varepsilon)$ are functions of ε only, and m is a constant accounting for the centrifugal effect along Σ_p due to the particle's inertia.

The Melnikov function in Eq. (5.8) is either strictly negative or oscillates between positive and negative values[1]. When the function has a constant negative sign, we have $H_{n+1} < H_n$ for all n, which indicates that particles are centrifuged away from the vortices. When the function has simple zeros, particles can enter and exit the closed flow. Thus, the central prediction of our theory is that a heavy particle in the open flow may be captured by an attracting point near the vortices provided that the Stokes number St is below the critical value

$$\mathrm{St}_c(\gamma) = \frac{4 \mid \gamma \mid}{m(1+\gamma)^2}\Big[a(\varepsilon) + \widetilde{V}_T b(\varepsilon)\Big], \tag{5.9}$$

which is the condition for $M(t_n)$ to change sign (and in fact have infinitely many isolated zeros). We therefore predict that the levitation of heavy particles released in the open flow region above the vortices is possible for $\mathrm{St} < \mathrm{St}_c(\gamma)$. These results imply that heavy particles with densities across many orders of magnitude can be levitated by the same flow[2].

Remarkably, Eq. (5.9) shows that St_c is an increasing function of $\widetilde{V}_T$ and hence that gravity *facilitates* levitation. This means that a particle that would be too inertial to penetrate inside Σ_p in the absence of gravity can be captured by the attracting points when gravity is present. This equation also shows that St_c depends on the vortex strength ratio γ and in particular that the

[1]Because our calculations are for the vortices (A, B), this conclusion would be reversed for the image vortices (A', B').

[2]In terms of the particle radius d and particle-to-fluid density ratio ρ_p/ρ_f, for given ε and flow Reynolds number the Stokes number for heavy particles is $\mathrm{St} \propto d^2\rho_p/\rho_f$, meaning that the predictions can be the same for a denser (but smaller) particle.

normalized critical Stokes number is

$$\frac{\mathrm{St}_c(\gamma)}{\mathrm{St}_c(1)} = \frac{4 \mid \gamma \mid}{(1+\gamma)^2}, \tag{5.10}$$

irrespective of $\widetilde{V}_T$ and ε. Thus, not only levitation is possible for both co- and counter-rotating vortices of arbitrary $\gamma \neq -1$, but also the phenomenon is *more pronounced* for counter-rotating vortices with sufficiently small γ than for identical co-rotating vortices ($\gamma = 1$).

Figure 5.2 shows the analytical prediction in Eq. (5.10) along with a numerical verification for particles released in the open flow above the vortices (red region in Fig. 5.1), where bisection in St was used to determine the critical value at which particles start crossing Σ_p. The agreement with the numerics is good, particularly for co-rotating vortices. Importantly, the numerical St_c is always higher than the theoretical prediction, widening the range of the effect [3].

5.3. Potential flow simulations

To further illustrate the theoretical results above we have done a series of computations by choosing the parameters according to the diagram of Fig. 5.2. Figure 5.3 shows the evolution of clouds of particles for two different Stokes numbers in the case of co-rotating vortices: $\mathrm{St} < \mathrm{St}_c$ [Fig. 5.3(a, b)] and $\mathrm{St} > \mathrm{St}_c$ [Fig. 5.3(c, d)], corresponding to the points P_1 and P_2 in Fig. 5.2, respectively. The particles are released in the open-streamline region above the vortices (red) and in the closed-streamline region near the vortices (blue), as sketched in Fig. 5.1. The clouds are shown after 16 turnover times [Fig. 5.3(a, c)] and after 95 turnover times [Fig. 5.3(b, d)],

[3]The agreement is less satisfactory for counter-rotating vortices (unless $|\gamma|$ is small) because our theory requires not only that $\varepsilon \ll 1$ (i.e., that the distance between I and the wall be large compared to the separation between the vortices) but also that $\varepsilon < (\gamma+1)/2$ (i.e., that each individual vortex be far from the wall—some distance from the wall would be required also for the stability of the vortex system [**149**]). The latter condition is satisfied in the co-rotating case since $(\gamma+1)/2 > 1/2$, but not in the counter-rotating case unless $|\gamma|$ is sufficiently small, which corresponds to one vortex being sufficiently weaker than the other.

which was chosen purposely large to facilitate visualization of the long-term behavior. For P_1, a fraction of the blue particles as well as a fraction of the red particles accumulate near the two attracting points after long times. (For visualization, particles near the attracting points were slightly dispersed). In contrast, for P_2 only blue particles are captured by the attracting points; red particles remain outside Σ_p and are transported downstream. These observations are in complete agreement with our predictions.

Similar agreement is observed for counter-rotating vortices, as shown in Fig. 5.4 for $\mathrm{St} < \mathrm{St}_c$ (Q_1 in Fig. 5.2) and $\mathrm{St} > \mathrm{St}_c$ (Q_2 in Fig. 5.2), but with two important differences. First, in the case of Q_1 there is only one attracting point around which a portion of blue and red particles accumulate. This is expected for the range of Stokes number considered, but studies of isolated counter-rotating pairs suggest that other attractors may exist for different parameters [**124**]. Second, for Q_2, there is no attractor, so that not only do red particles not cross Σ_p inward, but also all blue particles are centrifuged outward across Σ_p. As a result, in this case no particle is captured by an attractor independently of the initial condition.

5.4. Simulations of the Navier-Stokes equations

To verify the significance of our predictions for more realistic flows, we have simulated viscous flow solutions of the Navier-Stokes equations in the setup of Fig. 5.1. As shown in Fig. 5.5, for $\mathrm{St} < \mathrm{St}_c$, particles with initial positions in both the closed flow [5.5(a, c)] and open flow [5.5(a, d)] are captured and levitated by attracting points in the vicinity of the vortices. The main difference from the case of idealized potential flows considered above is that levitation is not permanent in viscous flows since the vortices eventually coalesce. For the conditions considered in Fig. 5.5, which corresponds to approximately 15 turnover times before vortex

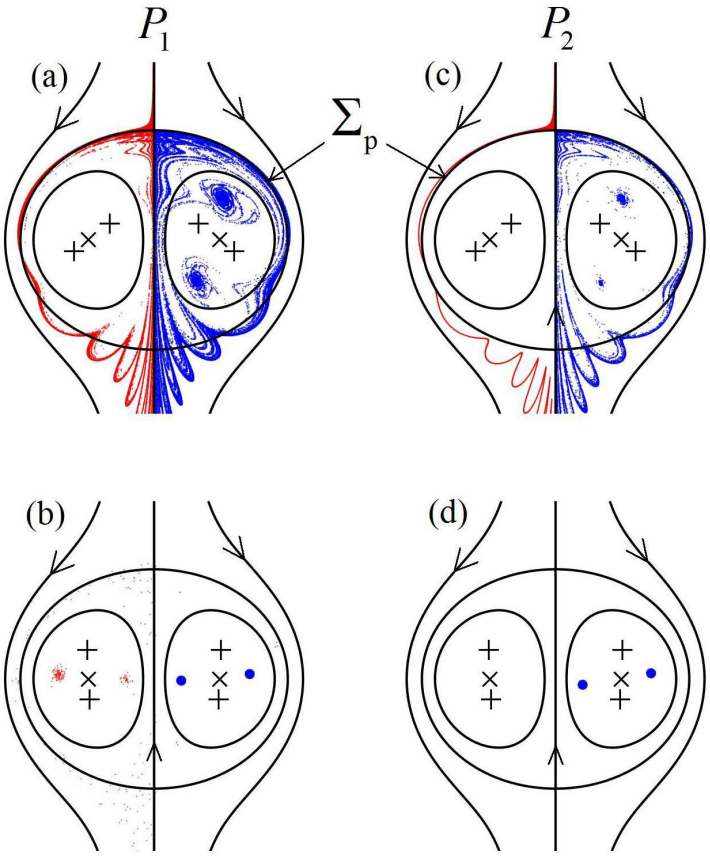

Figure 5.3. Levitation by co-rotating vortices for the flow in Eq. 5.1. Colors indicate particle clouds at different times for (a, b) point P_1 ($\mathrm{St} < \mathrm{St}_c$) and (c, d) point P_2 ($\mathrm{St} > \mathrm{St}_c$) in Fig. 5.2. The first row [(a) and (c)] corresponds to $t = 16$ and second row [(b) and (d)] to $t = 95$ (in units of the undisturbed turnover time, $2\pi/\Omega_0$). Also shown are streamlines defined by $\psi_p(y, z) = cte$ (continuous lines), the vortices ($+$), and the center of vorticity ($\times$). Red and blue represent particles released from the open and closed flows, respectively, and are shown on opposite sides of the wall to facilitate visualization.

merging, particles from the open flow are accelerated downward by vortices alone but, when capture occurs, up to 20% of the particles are levitated by the vortices until they merge [dashed versus continuous lines in Fig. 5.5(b)]. A partial view of the basins of attraction [Fig. 5.5(e)]

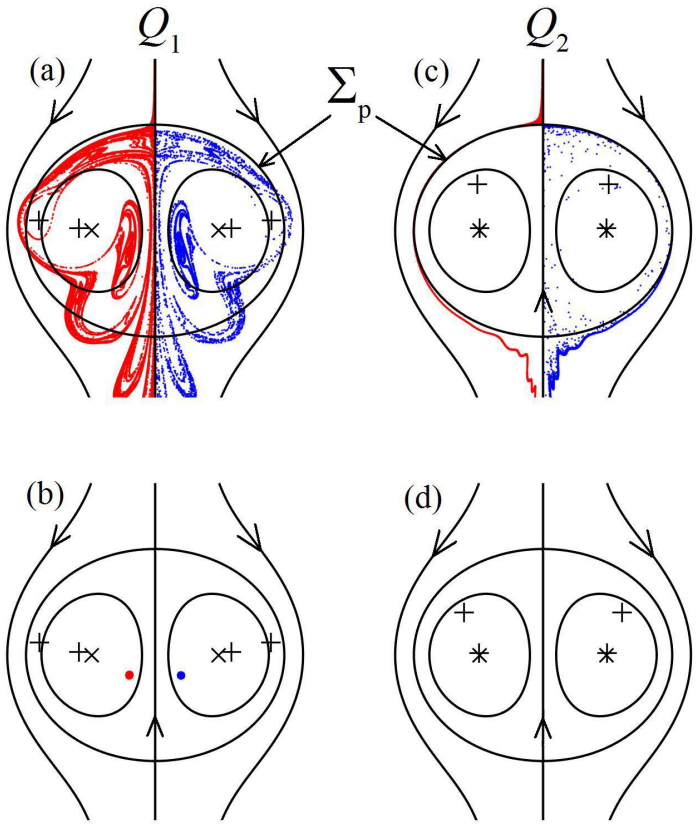

Figure 5.4. Levitation by counter-rotating vortices. Counterpart of Fig. 5.3 for (a, b) point Q_1 ($\mathrm{St} < \mathrm{St}_c$) and (c, d) point Q_2 ($\mathrm{St} > \mathrm{St}_c$) in Fig. 5.2. The first row [(a) and (c)] corresponds to $t = 21$ and the second row [(b) and (d)] to $t = 127$. As in the case of co–rotating vortices, Σ_p is open to particles released outside when $\mathrm{St} < \mathrm{St}_c$ and closed to those particles when $\mathrm{St} > \mathrm{St}_c$. Here there is, however, a single attracting point for each vortex pair for Q_1 and none for Q_2.

provides further insight into the initial conditions of the particles that can be levitated by this mechanism. Simulations were performed using OpenFOAM [**150**].

5.5. Stability analysis and simulation results

Dynamics near the attracting points. To prove the existence and stability of attracting points when gravity is present, we focus on one vortex pair, say (A, B). The pair (A', B') is assumed

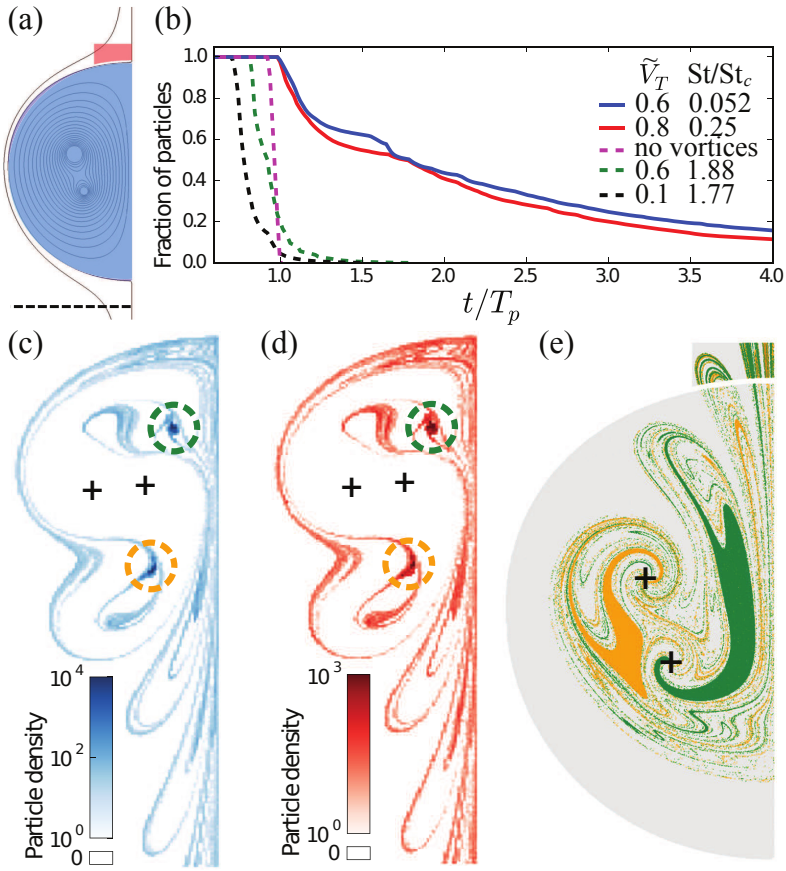

Figure 5.5. Particle levitation for Navier-Stokes simulations of co-rotating vortices. (a) Initial positions of uniformly distributed particles with zero initial velocity in the open (red) and closed (blue) flow. (b) Fraction of particles from the open flow remaining above a threshold [dashed line in (a)] as a function of time in units of T_p (the maximum particle residence time in the absence of vortices). The various choices of $\widetilde{V}_T$ and St represent scenarios in which: particles are levitated by attracting points (solid lines), particles do not cross into the closed flow region (dashed black), no attracting point are present (dashed green), and vortices are absent (dashed magenta). (c, d) Density plots for particles from the closed (c) and open (d) flows at $t/T_p = 3.7$ for one choice of parameters in (b) (solid red); dashed circles mark the positions of the attracting points. (e) Section of the attraction basins: initial conditions of particles inside dashed circles of corresponding colors in (c) and (d). The flow parameters are $\gamma = 0.7$, $\varepsilon = 0.375$, and Reynolds number $Re = 4,000$.

to be far from (A, B) so that, to leading order, the angular velocity is Ω_0 and the translational velocity of point I is w_0. We consider the motion of heavy particles in the reference frame rotating at constant velocity Ω_0, and translating at constant vertical speed w_0. We also non-dimensionalize the variables using time and length scales relevant for the dynamics near the vortices: $1/\Omega_0$ for times and d_0 for lengths. These units will be called "internal units" in the following and should not be confused with the "external units" $2L_0/w_0$ and L_0 used above to investigate the dynamics near the separatrix Σ_p. In addition, we use the rotating Cartesian coordinates $(I; X, Y, Z)$ where $IX = Ix$ is perpendicular to the plane of the flow, and IY and IZ coincide with Iy and Iz at the initial time. Using $\hat{\mathbf{X}}$, $\hat{\mathbf{Y}}$, and $\hat{\mathbf{Z}}$ to denote the unit vectors in the coordinate directions, the unit vector in the direction of gravity reads $\hat{\mathbf{g}} = -\hat{\mathbf{Y}} \sin t - \hat{\mathbf{Z}} \cos t$.

In this new frame, the non-dimensional equation of motion for heavy particles in the internal system of units is

$$\ddot{\mathbf{R}} = \frac{1}{\mathrm{St}}\big(\mathbf{W} - \dot{\mathbf{R}}\big) + \frac{V_T}{\mathrm{St}}\hat{\mathbf{g}} + \mathbf{R} - 2\hat{\mathbf{X}} \times \dot{\mathbf{R}}, \tag{5.11}$$

where $\mathbf{R}$ is the particle position and $\mathbf{W}$ is the fluid velocity field (in this frame). The last two terms are the centrifugal and Coriolis forces, respectively. Because particles are much heavier than the fluid, forces proportional to the mass of the displaced fluid, like the Archimedes force and the opposite of the Coriolis and centrifugal forces acting on the fluid, have been neglected. Also, St=$\Omega_0\tau_p$ is the Stokes number already introduced above, $V_T = g\tau_p/\Omega_0 d_0$ is the non-dimensional settling velocity in still fluid, and the ratio V_T/St is the inverse Froude number. The Stokes number (St) and non-dimensional settling velocity (V_T) introduced with the internal

units are related to the external ones by

$$\widetilde{\mathrm{St}} = \varepsilon^2 \mathrm{St}, \quad \text{and} \quad \widetilde{V}_T = V_T/\varepsilon, \tag{5.12}$$

where $\widetilde{\mathrm{St}} \ll 1$, $\mathrm{St} = O(1)$, $\widetilde{V}_T = O(1)$, and $V_T \ll 1$. Therefore, gravitational settling is weak in the internal dynamics (near the vortices) and stronger in the external one (near the separatrix Σ_p). In contrast, particle inertia effects are weak in the external dynamics (which favors the crossing of Σ_p) and stronger near the vortices (which favors capture by attracting points).

To order ε^2, the fluid velocity field is

$$\mathbf{W} = \mathbf{W}_0(\mathbf{R}, \gamma) + \varepsilon^2 \big[\mathbf{W}_{2c}(\mathbf{R}, \gamma) \cos 2t + \mathbf{W}_{2s}(\mathbf{R}, \gamma) \sin 2t\big], \tag{5.13}$$

where the leading order is the relative velocity field induced by an isolated vortex pair with vortex strength ratio γ (see, e.g., Ref. [**124**]) and the velocity fields $\mathbf{W}_{2c}$ and $\mathbf{W}_{2s}$ account for the effect of the vertical wall (the symmetry axis Oz separating AB and $A'B'$). In the limit of small ε the wall causes each vortex pair to stretch and compress twice each revolution. That is why, in this frame and system of units, the perturbation terms are proportional to $\cos 2t$ and $\sin 2t$.

To analyze the stability of equilibrium points, we follow the procedure employed by IJzermans and Hagmeijer in Ref. [**119**], and set

$$\mathbf{R}(t) = \mathbf{R}_{eq} + \mathbf{h}(t), \tag{5.14}$$

where $\mathbf{R}_{eq}$ denotes any one of the equilibrium points in the rotating frame in the absence of both wall and gravity (the existence of these points, when neither wall nor gravity is present,

has been proven in Ref. [**121**] for identical vortices and in Ref. [**124**] for unequal vortices). In particular, $\mathbf{R}_{eq}$ is any solution of $\mathbf{W}_0(\mathbf{R}_{eq})/\mathrm{St} + \mathbf{R}_{eq} = \mathbf{0}$, which reflects the balance between inward drag and the centrifugal force at the equilibrium point. In Eq. (5.14), $\mathbf{h} = \mathbf{h}(t)$ represents the perturbation accounting for the effect of gravity and the wall. Using this decomposition in Eq. (5.11), and neglecting the quadratic terms in $\mathbf{h}$, we obtain

$$\ddot{\mathbf{h}} = \frac{1}{\mathrm{St}}\Big\{(\mathrm{D}\mathbf{W}_0^{eq})\,\mathbf{h} + \varepsilon^2\Big[\mathbf{W}_{2c}(\mathbf{R}_{eq},\gamma)\cos 2t + \mathbf{W}_{2s}(\mathbf{R}_{eq},\gamma)\sin 2t \\ -\widetilde{V}_T(\hat{\mathbf{Y}}\sin t + \hat{\mathbf{Z}}\cos t)\Big] - \dot{\mathbf{h}}\Big\} + \mathbf{h} - 2\hat{\mathbf{X}}\times\dot{\mathbf{h}}\,, \tag{5.15}$$

where $\mathrm{D}\mathbf{f}$ is used to denote the Jacobian matrix of $\mathbf{f}$ and $\mathrm{D}\mathbf{W}_0^{eq} = \mathrm{D}\mathbf{W}_0|_{\mathbf{R}_{eq}}$. The general solution of this non-homogeneous linear equation is the sum of a particular solution $\mathbf{h}_a(t)$ and the solution $\mathbf{h}_b(t)$ of the homogeneous part of the equation.

The homogeneous equation corresponds exactly to the case in which both gravity and the wall are absent. Focusing on equilibrium points $\mathbf{R}_{eq}$ that (in the absence of gravity and the wall) are asymptotically stable, we have $\mathbf{h}_b(t) \to 0$ as $t \to +\infty$. Provided the internal Stokes number is not too large, as considered here, there are either one or two such stable points when neither gravity nor the wall is present [**124**]; from here on we consider only these equilibria and show that they are converted into time-dependent attracting points when the effect of gravity and/or the wall are significant.

The particular solution can be sought in the form of a combination of two Fourier modes:

$$\mathbf{h}_a(t) = \sum_{n=1,2}(\mathbf{p}_n\cos nt + \mathbf{q}_n\sin nt), \tag{5.16}$$

where the amplitudes $\mathbf{p}_n$ and $\mathbf{q}_n$ are given by a set of linear equations,

$$\mathbf{L}_1\mathbf{p}_1 - \mathbf{M}_1\mathbf{q}_1 = \varepsilon^2\frac{\widetilde{V}_T}{\mathrm{St}}\hat{\mathbf{Z}}, \tag{5.17}$$

$$\mathbf{L}_1\mathbf{q}_1 + \mathbf{M}_1\mathbf{p}_1 = \varepsilon^2\frac{\widetilde{V}_T}{\mathrm{St}}\hat{\mathbf{Y}}, \tag{5.18}$$

$$\mathbf{L}_2\mathbf{p}_2 - \mathbf{M}_2\mathbf{q}_2 = -\frac{\varepsilon^2}{\mathrm{St}}\mathbf{W}_{2c}(\mathbf{R}_{eq},\gamma), \tag{5.19}$$

$$\mathbf{L}_2\mathbf{q}_2 + \mathbf{M}_2\mathbf{p}_2 = -\frac{\varepsilon^2}{\mathrm{St}}\mathbf{W}_{2s}(\mathbf{R}_{eq},\gamma), \tag{5.20}$$

for $\mathbf{L}_1 = \frac{1}{\mathrm{St}}\mathrm{D}\mathbf{W}_0^{eq}+2\mathbf{I}$, $\mathbf{M}_1 = \frac{1}{\mathrm{St}}\mathbf{I}+2\mathbf{A}$, $\mathbf{L}_2 = \mathbf{L}_1+3\mathbf{I}$, $\mathbf{M}_2 = 2\mathbf{M}_1$, and matrix $\mathbf{A}$ representing a rotation of $\pi/2$ around $\hat{\mathbf{X}}$. The matrices $\mathbf{M}_1$ and $\mathbf{M}_2$ are invertible—it can be checked that their determinants are nonzero irrespective of St. The matrix $\mathbf{L}_1$ is also invertible since its eigenvalues are $\lambda_i = 2 + \mu_i/\mathrm{St}$ $(i = 1, 2)$, where μ_i's are the eigenvalues of the matrix $\mathrm{D}\mathbf{W}_0^{eq}$, which are known to have non-zero imaginary parts. Finally, a similar argument can be used to show that the matrix $\mathbf{L}_2$ is also invertible. Thus, after some elementary algebra, we are led to

$$\big(\mathbf{M}_1^{-1}\mathbf{L}_1 + \mathbf{L}_1^{-1}\mathbf{M}_1\big)\mathbf{p}_1 = \varepsilon^2\frac{\widetilde{V}_T}{\mathrm{St}}\big(\mathbf{L}_1^{-1}\hat{\mathbf{Y}} + \mathbf{M}_1^{-1}\hat{\mathbf{Z}}\big). \tag{5.21}$$

By solving this last system we obtain the amplitude $\mathbf{p}_1$. The other amplitudes $\mathbf{p}_n$ and $\mathbf{q}_n$ can be obtained in a similar way, so that the periodic solution $\mathbf{h}_a(t)$ in Eq. (5.16) exists and is uniquely defined.

We therefore conclude that, for sufficiently small $\varepsilon \ll 1$, the trajectories of inertial particles in the presence of gravity and the wall converge to some periodic orbit in an ε^2-neighborhood of the equilibrium point $\mathbf{R}_{eq}$ of the unperturbed system.

Calculation of the Melnikov function. The variation of the undisturbed Hamiltonian $H = \psi_p(\mathbf{r}(t))$ along the disturbed trajectory $\mathbf{r}(t)$ between the discrete times τ_{2n} and τ_{2n+1} is [**147, 148**]

$$H_{n+1} - H_n = \int_{\tau_{2n}}^{\tau_{2n+1}} \frac{d}{dt}\psi_p(\mathbf{r}(t))\, dt = \int_{\tau_{2n}}^{\tau_{2n+1}} \nabla\psi_p(\mathbf{r}(t)) \cdot \frac{d\mathbf{r}(t)}{dt}\, dt. \tag{5.22}$$

Assuming the trajectory is close to the separatrix Σ_p, we write $\mathbf{r}(t) \simeq \mathbf{q}(t - t_n)$, where $\mathbf{q}(t)$ is a trajectory on Σ_p. Therefore it satisfies $\dot{\mathbf{q}} = \mathbf{v}_0(\mathbf{q})$, $\mathbf{q}(-\infty) = S_1$, and $\mathbf{q}(+\infty) = S_2$, where the z-coordinates of S_1 and S_2 are given by $z = \pm\big[(6-\widetilde{V}_T)/(2+\widetilde{V}_T)\big]^{1/2}$. For convenience, we take the initial condition $\mathbf{q}(0)$ at the intersection between Σ_p and the axis Oy. In addition, we perform the change of variables $t \to t - t_n$, and take into account the fact that $\tau_{2n} - t_n < 0 < \tau_{2n+1} - t_n$ and that $|\tau_{2n} - t_n| \gg 1$ and $|\tau_{2n+1} - t_n| \gg 1$ (because the dynamics are very slow near S_1 and S_2). The integration interval $[\tau_{2n} - t_n, \tau_{2n+1} - t_n]$ can then be replaced by $[-\infty, +\infty]$, leading to $H_{n+1} - H_n = \varepsilon^2 M(t_n)$, where $M(t_n)$ is the Melnikov function,

$$M(t_n) = \int_{-\infty}^{\infty} \mathbf{v}_0(\mathbf{q}(t)) \times \mathbf{v}_2\Big(\mathbf{q}(t), \frac{t + t_n}{\varepsilon^2}\Big)\, dt. \tag{5.23}$$

Note that in this equation and others below, the cross products should be interpreted as projected in the $\hat{\mathbf{x}}$ direction.

The unperturbed trajectory $\mathbf{q}(t)$ cannot be obtained analytically for arbitrary $\widetilde{V}_T$. We therefore approximate it by assuming that $\widetilde{V}_T$, though larger than the internal non-dimensional velocity V_T, is sufficiently smaller than unity that it allows us to write $\mathbf{q}(t) = \mathbf{q}_0(t) + \widetilde{V}_T\, \mathbf{q}_1(t) + O(\widetilde{V}_T^2)$, where the functions $\mathbf{q}_0(t)$ and $\mathbf{q}_1(t)$ are determined numerically. Setting $\mathbf{U}_2 = \mathbf{u}_2 -$

St $\partial \mathbf{u}_2/\partial\tau$, after some algebra the Melnikov function reads

$$M(t_n) = I_1 + I_2 + I_3 + O(\widetilde{V}_T^2) + O(\widetilde{V}_T \mathrm{St}), \tag{5.24}$$

where

$$I_1 = \int_{-\infty}^{\infty} \dot{\mathbf{q}}_0(t) \times \mathbf{U}_2\Big(\mathbf{q}_0(t), \frac{t+t_n}{\varepsilon^2}\Big)\, dt - \mathrm{St} \int_{-\infty}^{\infty} \dot{\mathbf{q}}_0(t) \times \ddot{\mathbf{q}}_0(t)\, dt, \tag{5.25}$$

$$I_2 = \widetilde{V}_T \int_{-\infty}^{\infty} \dot{\mathbf{q}}_1(t) \times \mathbf{U}_2\Big(\mathbf{q}_0, \frac{t+t_n}{\varepsilon^2}\Big)\, dt, \tag{5.26}$$

$$I_3 = \widetilde{V}_T \int_{-\infty}^{\infty} \dot{\mathbf{q}}_0(t) \times \Big((\mathbf{D}\mathbf{U}_2)\, \mathbf{q}_1(t)\Big)\, dt. \tag{5.27}$$

By expanding the sines and cosines appearing in I_1 and assigning zero to the integrals of odd functions of t, we obtain

$$I_1 = \frac{4\gamma}{(1+\gamma)^2} a(\varepsilon)\Big(\sin\frac{2t_n}{\varepsilon^2} - 2\mathrm{St}\cos\frac{2t_n}{\varepsilon^2}\Big) - m\,\mathrm{St}, \tag{5.28}$$

where the multiplicative coefficient $a(\varepsilon)$ depends only on ε,

$$a(\varepsilon) = \int_{-\infty}^{\infty} \dot{\mathbf{q}}_0(t) \times \Big[\mathbf{u}_{2s}(\mathbf{q}_0(t)) \cos\frac{2t}{\varepsilon^2} - \mathbf{u}_{2c}(\mathbf{q}_0(t)) \sin\frac{2t}{\varepsilon^2}\Big]\, dt, \tag{5.29}$$

and m is a constant,

$$m = \int_{-\infty}^{\infty} \dot{\mathbf{q}}_0(t) \times \ddot{\mathbf{q}}_0(t)\, dt. \tag{5.30}$$

The velocity fields $\mathbf{u}_{2c}$ and $\mathbf{u}_{2s}$ correspond to the streamfunctions ψ_{2c} and ψ_{2s} respectively.

The constant m is computed numerically once $\mathbf{q}_0(t)$ has been determined, resulting in $m \simeq 30.4$. The function $a(\varepsilon)$ is also computed numerically, and then fitted with an exponential-rational function of the form

$$a(\varepsilon) = \frac{e^{-\alpha_e/\varepsilon^2}}{\varepsilon^2}\big(\alpha_0 + \alpha_2\varepsilon^2 + \alpha_4\varepsilon^4\big), \tag{5.31}$$

where the α_i's are obtained using a least-squares algorithm. The resulting constants are $\alpha_e \simeq 0.60$, $\alpha_0 \simeq 16.5$, $\alpha_2 \simeq -9.5$, and $\alpha_4 \simeq -51.5$. Applying the same treatment to the integrals I_2 and I_3, we obtain

$$I_2 + I_3 = \frac{4\gamma}{(1+\gamma)^2}\,\widetilde{V}_T\big[b_2(\varepsilon) + b_3(\varepsilon)\big]\Big(\sin\frac{2t_n}{\varepsilon^2} - 2\mathrm{St}\cos\frac{2t_n}{\varepsilon^2}\Big), \tag{5.32}$$

where

$$b_2(\varepsilon) = \int_{-\infty}^{\infty} \dot{\mathbf{q}}_1(t) \times \Big[\mathbf{u}_{2s}(\mathbf{q}_0(t))\cos\frac{2t}{\varepsilon^2} - \mathbf{u}_{2c}(\mathbf{q}_0(t))\sin\frac{2t}{\varepsilon^2}\Big]\,dt, \tag{5.33}$$

$$b_3(\varepsilon) = \int_{-\infty}^{\infty} \dot{\mathbf{q}}_0(t) \times \Big[(\mathbf{D}\mathbf{u}_{2s})\,\mathbf{q}_1(t)\,\cos\frac{2t}{\varepsilon^2} - (\mathbf{D}\mathbf{u}_{2c})\,\mathbf{q}_1(t)\,\sin\frac{2t}{\varepsilon^2}\Big]\,dt. \tag{5.34}$$

Both b_2 and b_3 depend only on ε and are computed numerically once $\mathbf{q}_0(t)$ and $\mathbf{q}_1(t)$ have been determined. The sum $b_2(\varepsilon) + b_3(\varepsilon)$, denoted $b(\varepsilon)$ above, is fitted with an exponential-rational function of same form as the one used for $a(\varepsilon)$, with the coefficients α_i's replaced by β_i's: $\beta_e \simeq 0.60$, $\beta_0 \simeq 174.6$, $\beta_2 \simeq -1120.6$, and $\beta_4 \simeq 1972.0$.

Navier-Stokes simulations of viscous flows. The computations in Figs. 5.2-5.4 were performed assuming idealized inviscid flows (exact solutions of the Euler equations). For moderate Reynolds number, viscosity is expected to have significant effects on the flow, as viscous diffusion causes the size of the vortex cores to expand over time. Once the radius of either core

becomes comparable to the distance between the vortices, vortex merging occurs and any attractors of the particle dynamics vanish. We performed simulations solving the two-dimensional Navier-Stokes equations with a viscous working fluid to determine whether heavy-particle levitation could be observed prior to the eventual coalescence of the vortices. The initial velocity field of the fluid consisted of the superposition of a uniform downward flow (in the direction of gravity) with a velocity magnitude of $0.625w_0$ relative to the laboratory reference frame and two pairs of co-rotating Lamb-Oseen vortices with inter-vortex distance $2d_0$ as in the setup of Fig. 5.1. The Reynolds number of the flow, $Re = \Omega_0 {d_0}^2/\nu$, where ν is the dynamic viscosity of the fluid, was set to be $4,000$ in all simulations we report. For these conditions, in each run of our simulations we released $100,000$ particles from the closed flow and $50,000$ from the open flow with zero initial velocity, as defined in Fig. 5.5(a). After simulating many combinations of $\widetilde{V}_T$ and $\widetilde{\text{St}}$, we observed the following scenarios: for $\text{St}/\text{St}_c > 1$ either no attracting points exist or they exist but no particles from the open flow are captured by them; for $\text{St}/\text{St}_c < 1$ attracting points exist and particles from the open flow are captured and levitated by them.

To quantify the levitation mechanism for particles from the open flow, we calculate the fraction of particles released in the open flow that remain above a threshold as a function of time. We set the threshold to a distance $2.4L_0$ downstream from the initial center of vorticity I, which lies right below the closed flow separatrix so that any particle that falls below this threshold will not be pulled back upstream. This fraction is shown in Fig. 5.6, illustrating the different scenarios mentioned above, where time is represented in units of the maximum time T_p a particle with the given initial conditions would remain above threshold in the the same flow without vortices. We define the levitation period to be the time $t - T_p$ the particle remains above this threshold. For example, for $\widetilde{V}_T = 0.6$ and $\text{St}/\text{St}_c = 0.05$ particles from the open flow

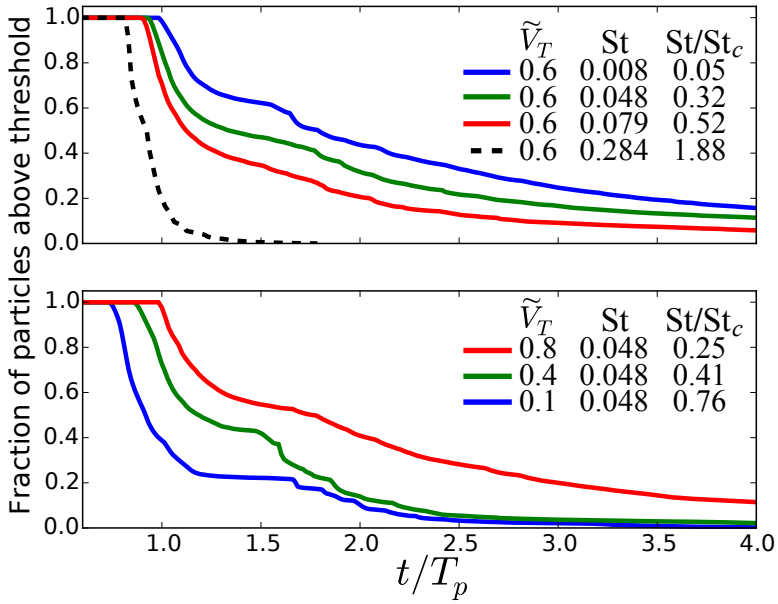

Figure 5.6. Fraction of particles from the open flow that remain above the threshold marked in Fig. 5.5(a) as function of time, for $\gamma = 0.7$ and $\varepsilon = 0.375$. The different curves correspond to (a) different choices of St for $\widetilde{V}_T = 0.6$ and (b) different choices of $\widetilde{V}_T$ for St $= 0.048$. The fraction of particles levitated for a long period increases as St is decreased and as $\widetilde{V}_T$ is (and hence gravity) increased, which parallels the dependence of St$_c$ in our theory based on potential flows.

approach the attracting points and nearly 20% of the particles have a levitation period larger than $3T_p$. For $\widetilde{V}_T = 0.6$ and St$/$St$_c = 1.88$, on the other hand, there are no attractors in the vicinity of the vortices and the levitation period is close to zero for most particles. We also observe that for a fixed value of St, increasing $\widetilde{V}_T$ can increase the fraction of particles above the threshold at all times, which is counter-intuitive but consistent with our analytical results for potential flow, where stronger gravity is observed to enhance the levitation effect.

Simulations were performed with OpenFOAM (version 2.2) using the PISO algorithm in solving for the flow field. The particle motion was calculated with Lagrangian particle tracking with one-way coupling of the particles to the fluid.

5.6. Discussion

Levitation—the action of rising or hovering in apparent defiance of gravity—is a fascinating phenomenon with many practical implications. A classic demonstration is the Bernoulli ball levitation, in which a macroscopic particle heavier than air (such as a ping pong ball) can levitate in response to an inclined upward air stream that appears to only partially balance gravity. A key aspect of that form of levitation is the transversal stability due to the Coandă effect which relies on the tendency of the flow to curve around the surface of the ball and sustains stable levitation when the upward air stream is tilted. Here, we report a new form of fluid-dynamical levitation that can be observed even for a downward stream (i.e., in the direction of gravity) and that allows heavy particles to be levitated by a flow regardless of whether they are 10, 100, or 1,000 times denser than the fluid. This phenomenon is fundamentally different from the Coandă effect in that it concerns microscopic heavy particles and requires no disturbance of the flow by the particles.

Our demonstration that heavy particles can be levitated shows that they can be transported in any direction relative to the asymptotic flow and gravity. Exploring this effect in more complex problems (possibly involving non-laminar flows), such as the air-transport of water droplets and aerosols [**151, 152, 153**], the resuspension of sediments by coherent vortical structures [**154, 155**], and industrial applications for particle sorting [**125, 126**], are among the questions of great interest for future research.

CHAPTER 6

Suppression of Faraday waves via substrate heterogeneity

The discovery of universality in driven systems has focused attention on idealized homogeneous media and model equations, yielding insights into the pattern formation processes that we observe in everyday life. In contrast to these idealized systems studied in the past, recent advances in the network sciences have drawn increasing attention to more realistic, heterogeneous systems. While the general expectation is that such systems exhibit more complex behaviors that are less amenable to analysis, surprising symmetric collective order can emerge instead, even when such states are unstable in the corresponding homogeneous systems. Here, we describe a general mechanism for such heterogeneity-stabilized symmetric states in parametrically driven media. We illustrate this mechanism theoretically in a mathematically-amenable model of coupled pendula and experimentally in Faraday waves. This research was conducted in collaboration with Zachary G. Nicolaou (first author), Ernest van der Wee, Michelle Driscoll, and Adilson E. Motter.

6.1. Motivation

The relationship between system symmetry and pattern formation in driven systems has been of longstanding scientific interest [**6, 156**]. In a typical pattern-forming system, a homogeneous medium undergoes an instability as a driving force increases past a threshold value. The state symmetry is then spontaneously broken, leading to universal and familiar patterns such as stripes, squares, or hexagons in two-dimensional systems, for example. While the emergence of

patterned states in homogeneous systems is now well understood, the unexpected consequences of system heterogeneity has also garnered attention. For example, Anderson localization, in which disorder in conducting materials can not only impede conduction through scattering but can also trap and localize charge carriers, has been of great interests for decades [**157**]. Similarly, impurities [**158, 159**] and heterogeneous driving [**160, 161**] have also been shown to have stabilizing properties in a variety of contexts. More recently, it has been found that system heterogeneity can surprisingly stabilize symmetric states that are unstable in the corresponding homogeneous system, as first noted in networks of coupled oscillators [**33, 34, 36, 35**]. While such asymmetry-induced symmetry has been clearly established theoretically, explicit experimental confirmation in realistic systems has yet to be demonstrated.

Here, we note a general mechanism that can lead to heterogeneity-stabilized symmetric states in continuous media. Noting that both periodic and random heterogeneities can generically open gaps between bands in the dispersion relation governing wave growth, we show that stabilized regions of the parameter space can emerge near band gaps in the presence of heterogeneities. To illustrate this mechanism, we focus on parametrically driven systems, such as the Faraday waves that form on a fluid surface driven by vertical vibration. We describe heterogeneity-induced stabilization in a minimal spring-pendulum system that is amenable to mathematical analysis as well as in simulations and experiments of Faraday wave formation in water.

Faraday waves are a classic example of a pattern forming system [**41, 6**]. Consider, for example, a cylindrical vessel containing an inviscid fluid like water and driven by a vertical vibration, as shown in Fig. 6.1a. For sufficiently large driving amplitudes, the flat fluid surface

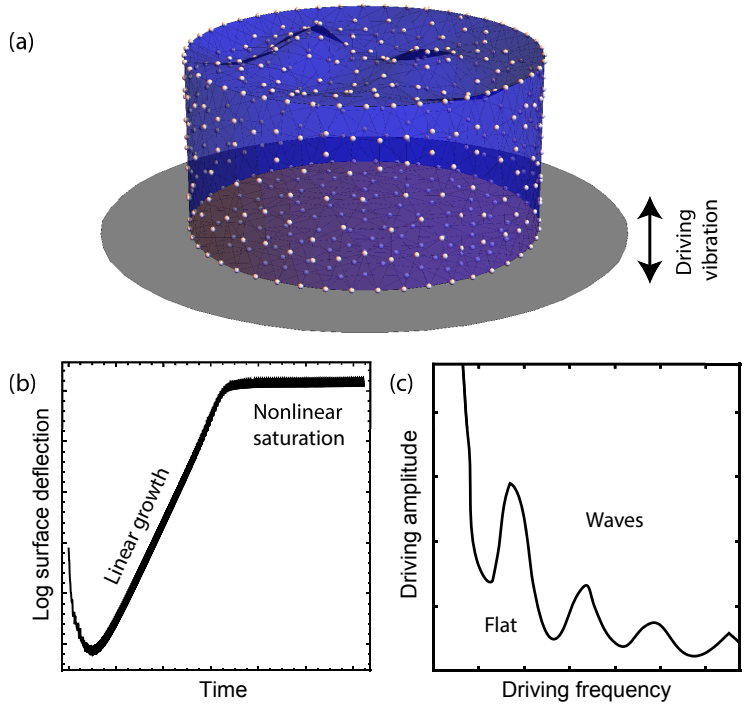

Figure 6.1. **Development of Faraday wave patterns. a**, Finite element simulation of fluid flow in a cylindrical vessel driven by vertical vibrations. **b**, When the driving amplitude is sufficiently large, the flat fluid film is linearly unstable, and a pattern of surface waves develops after a nonlinear saturation. **c**, Instability tongues corresponding to different wave modes separate flat and patterned waves in the driving amplitude–frequency parameter space.

becomes unstable in the linear stability analysis. The surface deflection then grows exponentially in the linear regime before a nonlinear saturation to a final pattern, as shown in Fig. 6.1b. The driving frequency vs. driving amplitude parameter space is then divided into regions in which the fluid surface remains flat and regions in which wave patterns emerge on the surface, as shown in Fig.6.1c, with each instability "tongue" exhibiting a different spatial pattern. Although a great number of theoretical and experimental studies on Faraday waves have been undertaken, relatively few have explored the effects of heterogeneous configurations such as substrates which are not flat [**162, 163, 164, 165**].

6.2. Pendulum array model

Before describing heterogeneity-stabilized symmetric states in Faraday waves, we first focus on the illustrative toy model of coupled pendula shown Fig. 6.2a. The position of each pendulum is described by the angle θ_i with the vertical direction, and each pendulum is coupled to its neighbors via a linear spring. Such pendulum models have been of recent interest in the study of time crystals because of their simple description compared to continuous media [**166, 167**]. The system is driven by the vertical periodic motion of the supporting ceiling. To model the impact of heterogeneity, the height of the support ceiling varies periodically while the length of the pendula also varies such that the uniform solution always exists (i.e., the base all pendula at the same height). In the accelerated reference frame of the moving ceiling, the equations of motion are

$$\begin{aligned} m(l \pm \Delta)\ddot{\theta}_i = &-m\left(g + a\cos(\omega t) \pm 4k_s\Delta\right)\sin(\theta_i) \\ &+ k_s(l \mp \Delta)\sin(\theta_{i+1} - \theta_i) \\ &+ k_s(l \mp \Delta)\sin(\theta_{i-1} - \theta_i), \end{aligned} \tag{6.1}$$

where $l \pm \Delta$ are the pendulum lengths, k_s is the spring constant, g is the gravitational constant, m is the mass of the pendula, and a is the amplitude of the vertical acceleration.

When $\Delta = 0$, the system is homogeneous with all pendula identical, while for $\Delta > 0$, the pendula lengths alternate. In the absence of driving, the propagation of waves in the pendulum array is determined by the linear dispersion relation that relates the wavelength of the waves to their frequencies. When $\Delta > 0$, a band gap opens in the undriven dispersion relation, as shown in Fig. 6.2b. Taking the Fourier decomposition with the Bloch wave solutions determined by

Floquet theory, the stability of this equation can be determined through the largest eigenvalue of a linear operator [**168**]. Additionally, direct numerical integration of Eq. (6.1) has been implemented to find the growth rate from the base solution initialized with random perturbations. Each tongue in the dotted lines in Fig. 6.2c corresponds to a different wavenumber that fits in the periodic domain with 16 pendula as determined through direct numerical simulations, while the stability boundaries for subharmonic modes in the infinite system limit as determined by Floquet theory are shown as solid lines. The driving frequencies near $f_d/2 = 2$ correspond to a wavenumber $k = \pi$ where the band gap opens. The band gap introduces an additional barrier that requires larger driving forces to overcome before the system goes unstable. The instabilities near $k = \pi$ are then shifted in frequency in opposite directions for the modes in different bands as the gap opens, and thus the system is stabilized around this band gap.

As is usually the case, the prominent instabilities in the homogeneous system are subharmonic with oscillation periods of twice the driving period, while the harmonic instabilities (with the same period as the driving) only occur for larger driving amplitudes and lower frequencies. Thus, this instability only partially breaks the symmetry inherent in the system. Interestingly, in the center of the band gap for the heterogeneous system, a different short-wavelength instability, which we deem *anharmonic* remains which is neither harmonic nor subharmonic but emerges with a frequency that is incommensurate with the driving frequency. This anharmonic instability fully breaks the symmetry of the driving force, as the frequency of the instability ranges between 0.4 and 0.6 times the driving frequency (depending on the parameters) rather than being exactly half the driving frequency, as was the case for subharmonic instabilities. We observed this unusual behavior only in specific models when a mode lies exactly at the boundary

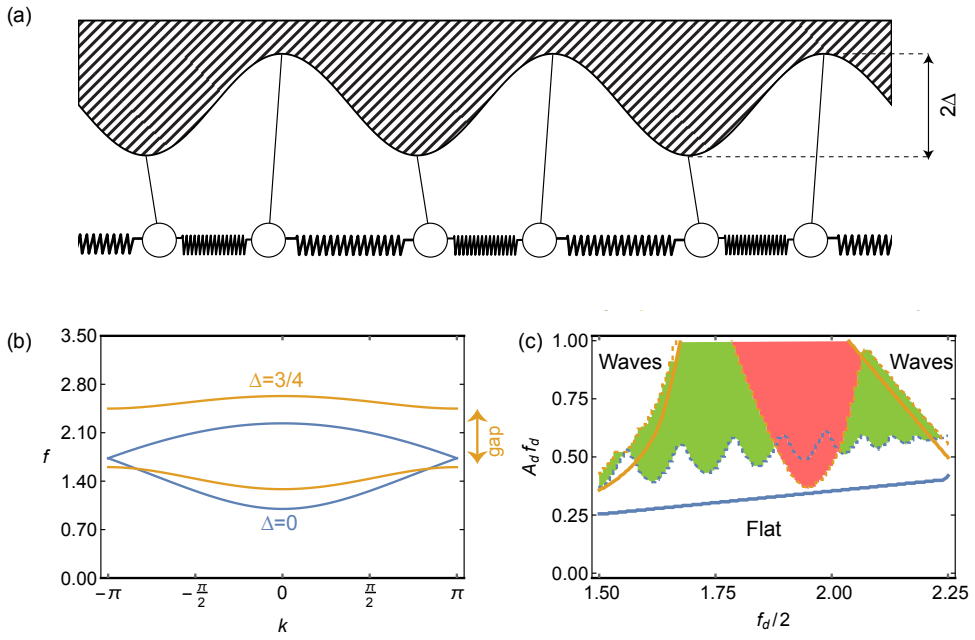

Figure 6.2. **Wave suppression in heterogeneous array of coupled pendula. a**, Array of coupled pendula with periodically varied rod lengths. **b**, Frequency f vs wavenumber k for the infinite array with the homogeneous ceiling (blue line) and the heterogeneous ceiling (orange line). **c**, Stability boundaries in the driving frequency f_d and driving velocity $A_d f_d$ space near the band gap, with patterned wave states forming above the solid (dashed) lines and unpatterned flat states below the solid (dashed) lines in the infinite (finite) systems. The heterogeneity stabilizes the flat states in the green regions, while an anharmonic instability appears in the pink region.

between two bands that separate in the band gap[1]. Other interesting behavior including localized and topological states have been noted to occur around band gaps [**169, 170, 171, 172**].

6.3. Simulations of Faraday waves with a heterogeneous substrate

We turn next to the demonstration of heterogeneity-stabilzied symmetric states in the context of Faraday waves. While a complete theory on the emergence of Faraday waves in a viscid

[1]For the system of pendula with alternating masses rather than alternating lengths (and in the Faraday waves described below), the modes in different branches split evenly without leaving an anharmonic instability behind, and a larger region of parameter space is stabilized by the heterogeneity.

fluid has been recently developed [**173**], we focus on the inviscid theory for simplicity, which adequately describes our experiments in water after fitting for phenomenological damping coefficients. Let h specify the position of the fluid surface at $z = h_0 + A_d \sin(\omega_d t) + h$. The flat surface corresponds to $h = 0$ with fluid velocities $u_z = A_d \omega_d \cos(\omega_d t)$, $u_x = u_y = 0$, and pressure $P = -gz$. This is always a solution to the fluid equations of motion, and the stability of this base solution is considered. For the flat substrate, extensive analytical work has been done, and the surface deflection with wavenumber k and $h = h_0 + \mathrm{e}^{ikx} H$, can be described in terms of the Mathieu equation,

$$\frac{\partial^2 H}{\partial t^2} = -k \tanh(k h_0) \left(g + k^2 \sigma - A_d \omega_d \sin(\omega_d t) \right) H. \tag{6.2}$$

The undriven dispersion relation,

$$\omega^2 = k \tanh k h_0 \left(g + \sigma k^2 \right), \tag{6.3}$$

between the wavenumber k and the frequency ω of a disturbance governs the instabilities for small driving amplitudes. In particular, waves with frequencies that are half-integer multiples of ω_d have positive growth rate β and are easily excited at small amplitudes.

For heterogeneous substrates, we implemented finite element simulations to assess whether an inviscid fluid film would remain flat or become patterned under a given driving frequency and amplitude. As in the pendulum system, the periodic substrate opens a band gap at a wavelength of one half of the substrate wavelength, as shown in Fig. 6.3a, leading to a shift in the instability tongues that stabilizes the uniform film over an expanded parameter range. To probe the impact that more general heterogeneous substrates have on the instability boundary, we generated five hundred random substrate shapes, taking the Fourier coefficients of the first twelve

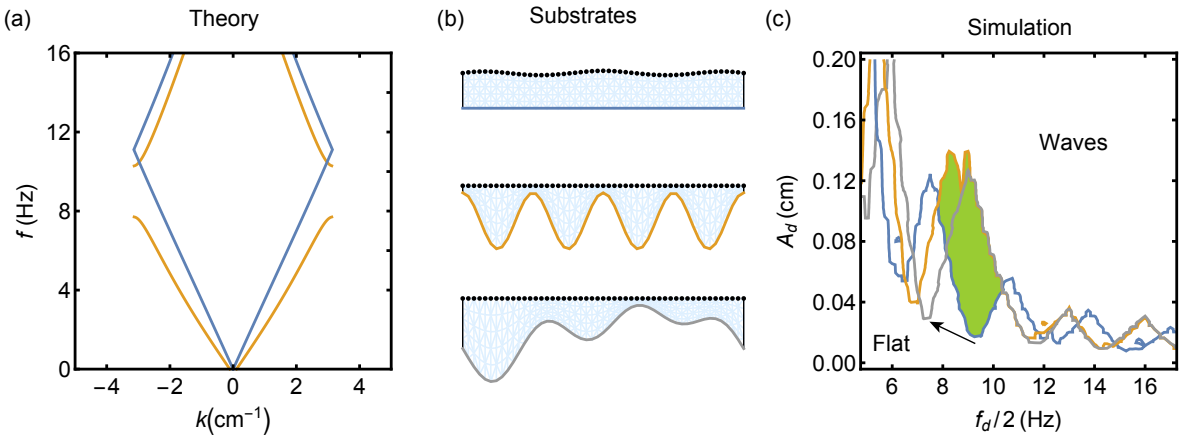

Figure 6.3. **Suppression of Faraday wave instability.** **a**, Analytically calculated frequency–wavelength dispersion relation for flat and periodic substrates. As in the pendulum system, a gap opens for the periodic substrate. **b**, The simulation domain and mesh for flat (blue), periodic (orange), and random (gray) substrates. **c**, Instability boundaries, with the heterogeneity-stabilized regions shaded green.

modes as random Gaussian variables (with amplitude inversely proportional to Fourier index). For each of these substrates, we measured the growth rate β for a range of fiftey-five values of frequency ω_d and amplitude A near the dominant subharmonic instability tongues for driving accelerations around $0.8g$. We then selected the substrate that created the largest gap between the modes around 8Hz and 12Hz. The flat, periodic, and optimal random substrates are shown in Fig. 6.3b. Surprisingly, the simulated stability regions for this optimal random substrate was nearly identical to that of the periodic substrate, despite the fact that the substrate was aperiodic, as shown in Fig. 6.3c. We emphasize that the driving strength necessary to excite the instability for the heterogeneous substrate is significantly higher than for the flat substrate for frequencies near the instability. Thus, surprisingly, the heterogeneity in the substrate stabilizes the flat, free-surface solution for these frequencies.

6.4. Experimental results

Since the dispersion relation in Eq. (6.3) depends exponentially on the film thickness, the substrate heterogeneity must be rather large to significantly impact the instability boundaries. Because of these very heterogeneous geometries, it is natural to speculate that the predominant mechanism behind our observations is compartmentalization of the fluid between the maxima of the substrate. To test whether simple compartmentalization can account for the heterogeneity-induced stabilization, we performed simulations for substrates with a fixed number of narrow peaks and used periodic boundary conditions to both eliminate side-wall effects and maintain full translational symmetry. Importantly, the distributions of narrow peaks with even spacing does a substantially poorer job of stabilizing the flat film than a sinusoidal substrate, shifting the relevant mode only 10% as much as the sinusoidal mode. Furthermore, distributions with uneven spacing between the peaks stabilize a slightly larger region than the evenly spaced distributions. Thus, compartmentalization of domains alone cannot account for the stabilization observed for heterogeneous substrates, and the more symmetric heterogeneities do not outperform more asymmetric configurations generally.

To test these numerical predictions, a flat substrate, a periodic substrate, and the optimal random substrate with the largest stabilizing effect were 3D-printed in a narrow box geometry, and the stability boundaries for each substrate was determined in the driving frequency–amplitude space, as shown in Fig. 6.4. Extracting the effective damping coefficient and box dimensions from the experimental data, the shifts in the instability tongues confirmed our numerical simulations. In particular, both the periodic and random substrates exhibited stable flat films in a large region of the parameter space corresponding to the band gap while the flat substrate

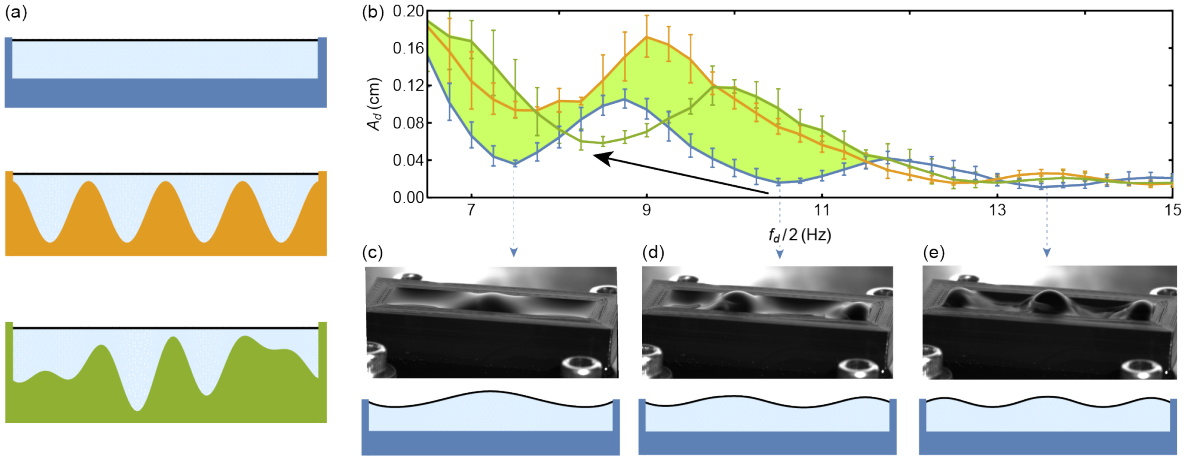

Figure 6.4. **Heterogeneity-stabilized homogeneous states in Faraday wave experiments.** **a**, Flat (blue), sinusoidal (orange), and random (green) substrate geometries, generated from simulations. **b**, Experimental instability boundaries in the driving amplitude vs. driving frequency space, with line color indicating corresponding substrate geometry in **a**. The instability mode for the three tongues in flat substrate are shown in **c**-**e**, as indicated by the blue dotted arrows. The error bars in **b** show the standard error from 4 measurements at each frequency. The solid black arrow in **b** illustrates that the mode in **d** is shifted to lower frequencies for the heterogeneous substrates, leading to the stabilization of the homogeneous film in the light-green highlighted area in **b**.

developed patterned waves in that region. Thus, we have clearly shown that the band-gap opening mechanism behind heterogeneity-induced stabilization of symmetric states is general and robust enough to observe in realistic systems.

6.5. Simulation and experimental methods

The inviscid fluid motion is described by a velocity potential ϕ which satisfies the Laplace equation with Neumann boundary conditions at solid surfaces (located at points in a set Ω) and Diriclet boundary conditions on the free surface (located at $z = h_0 + h$),

$$\nabla^2\phi = 0, \;\; \hat{\mathbf{n}} \cdot \nabla\phi|_{\mathbf{x}\in\Omega} = 0, \text{ and } \;\; \phi|_{z=h_0+h} = \zeta, \tag{6.4}$$

where $\hat{\mathbf{n}}$ is the outward pointing surface unit normal vector. The evolution of the surface potential ζ follows from the Bernoulli equation for inviscid flows,

$$\begin{aligned}\frac{\partial \zeta}{\partial t} &= \frac{\sigma}{\rho}\nabla\cdot\hat{\mathbf{n}} - (g + A_d\omega_d^2\sin(\omega_d t))h \\ &\quad - \left(\frac{1}{2}\left|\nabla\phi\right|^2 - \frac{\partial\phi}{\partial z}\frac{\partial h}{\partial t}\right)\Bigg|_{z=h_0+h,}\end{aligned} \tag{6.5}$$

while the evolution of the surface height h follows from the kinematic equation,

$$\frac{\partial h}{\partial t} = \left(\frac{\partial\phi}{\partial z} - \nabla\phi\cdot\nabla h - \nu_1 h + \nu_2\nabla^2 h\right)\Bigg|_{z=h_0+h.} \tag{6.6}$$

We include additional damping terms $-\nu_1 h + \nu_2\nabla^2 h$ in Eq. (6.6) in order to mimic the neglected viscosity and regularize the numerics, and we choose the values of ν_1 and ν_2 to fit the experimental instability boundaries. Equations (6.5)-(6.6) are integrated numerically in time, where ϕ is computed from moving mesh finite element solutions of Eq. (6.4) each time step using the FEniCS package in Python. The instability boundaries derived from the Mathieu equation in Eq. (6.2) for the flat substrates were used to validate our simulations. Two-dimensional rectangular geometries and three-dimensional box and cylindrical geometries were implemented with solid side walls.

For the Faraday wave experiments, we used the Vibration Test Systems mechanical shaker to drive the fluid. The fluid domain of the printed substrates measured 4cm long by 1cm wide by 0.5cm tall. The substrates were glued to an acrylic plate which was stacked over an accelerometer. The vessels were filled to the brim to minimize contact line pinning effects [**174, 175**]. The acceleration of the substrate was recorded with an Arduino and fit to a sinusoid curve to relate the signal generator voltage to acceleration. A camera was used to monitor fluid surface during

driving by synchronizing the camera frame rate with the driving frequency. The driving voltage was incrementally increased for each frequency until the flat fluid surface became unstable. Then, the acceleration was recorded for each critical frequency and used to define the instability boundary. This was repeated three times for each frequency to estimate the uncertainties.

6.6. Final comments

In summary, we have studied the impact of heterogeneous system parameters on parametric instabilities. We found that, counterintuitively, system heterogeneity can stabilize the symmetric base solution and lead to asymmetry-induced symmetry. We observed this phenomenon numerically in both fluid and elastic media and proposed a mechanism based on band-gap opening that can be applicable to a large array of systems. These observations complement the traditional view of pattern formation as a symmetry breaking phenomenon and demonstrate the importance of symmetric states in realistic, heterogeneous systems.

CHAPTER 7

Optimal asymmetry in engineered and botanical structures

Spontaneous symmetry breaking events occur when a system transitions to a new state that no longer reflects the symmetry of the forces acting on the system. These events underlie phenomena that occur at the length scales relevant to elementary particle physics, through the molecular organization of complex biomolecules, to the anisotropic distribution of matter across the universe, and, hence, have been a focal point of study throughout physics during the 20th century. Here, we explore how introducing asymmetry into the structure of classical columns can inhibit buckling of columns under load, and thus serve to, counter-intuitively, preserve the symmetric (unbuckled) state of the system. We demonstrate how the optimal shape of column cross sections are asymmetric under constrained conditions and how this may be realized in botanical structures. This work joins previous findings of scenarios in which asymmetry is required in order to stabilize symmetric systems states, such as in coupled oscillator networks, and supports new investigation into how natural and engineered systems may achieve robustness. This research was conducted in collaboration with Adilson E. Motter.

7.1. Motivation

One definition of physics is the study of the fundamental symmetries that exist in the universe. The importance of understanding symmetries is ubiquitous across the sub-fields of physics, from quantum and Newtonian mechanics to relativity. So, it was a paradigm shift when L. D. Landau became the first to frame many of the phenomena studied in statistical

physics as broken symmetries and, moreover, that a phase transition is a spontaneous symmetry breaking event [**37**]. A spontaneous symmetry breaking event occurs when a system suddenly transitions to a state that no longer reflects the symmetry of the laws that govern the system. Such events underlie the Standard Model of particle physics [**39**] and are manifest in familiar examples like the sudden magnetization of a metal when cooled below the Curie temperature or the sudden onset of convection in a fluid in the presence of a temperature gradient [**38**]. In these examples, the symmetric state of the systems loses stability as some parameter is quasistatically varied (e.g., temperature), even though the symmetries of the governing laws remain preserved.

Here, the classic example of spontaneous symmetry breaking we consider is column buckling. A column is a support structure that serves to withstand an axially applied load that originates from either an external source or its own weight. For an ideal, uniform cylindrical column, the stress imposed by the load is completely symmetric along the axis and the column has complete rotational symmetry. Given the elasticity of the material, the column is compressed by an amount proportional to the load. However, once the load reaches a critical value, the straight configuration of the column becomes unstable and any perturbation will cause the column to transition to a buckled state, which neither reflects the rotational symmetry of the column nor the symmetry of the loading forces [**42**]. Given the structural purpose of a column, it is no surprise that designing stronger columns has been a goal of architects and engineers since the time of the ancient Greeks. What is surprising, at least on first thought, is that designing a cylindrical column with round cross section and uniform radius produces one of the weakest column constructions.

7.2. Designing stronger columns

Determining the critical buckling load of a column is an old problem that was solved through contributions from Robert Hooke, James and Daniel Bernoulli, and Euler [**176**]. The problem of determining the ideal shape of a column, that is, the shape that would support the maximum load for a column of fixed volume and length, also has a rich history, extending from the the time of Lagrange (who arrived at an incorrect solution) to the 21st century. Even when considering ideal materials an array of mathematical subtleties make this a challenging optimization problem [**42, 177, 43, 178, 179**]. The majority of the literature is concerned with solving for the ideal distribution of mass along the axis of the column. For example, when the ends of a column are clamped to fixed positions, the column can support a larger load if the column is thicker in the middle and thinner near the end points [**42**].

Another way to optimize the column strength is by manipulating its cross-sectional shape. For a column of constant cross-section with length L and constructed from a material with modulus of elasticity E, the critical buckling load, according to Euler-Bernoulli beam theory, is

$$P_{\text{crit}} = \frac{\pi^2 EI}{(KL)^2}, \tag{7.1}$$

where K is a constant the depends on the boundary conditions and I is the second moment of area. In Fig. 7.1, we show the relative buckling load of columns with cross sections of different shape, but equal area. It is surprising, as first, that a column of triangular cross section has a substantially higher (greater than 20%) buckling load than a column with circular cross section [**42**]. This result is grounded in the dependence of P_{crit} on I, which is greater for a triangle (or any N-sided polygon) than a circle of equal area. The second moment of area is a geometrical property of an area which reflects how its points are distributed with regard to an arbitrary axis,

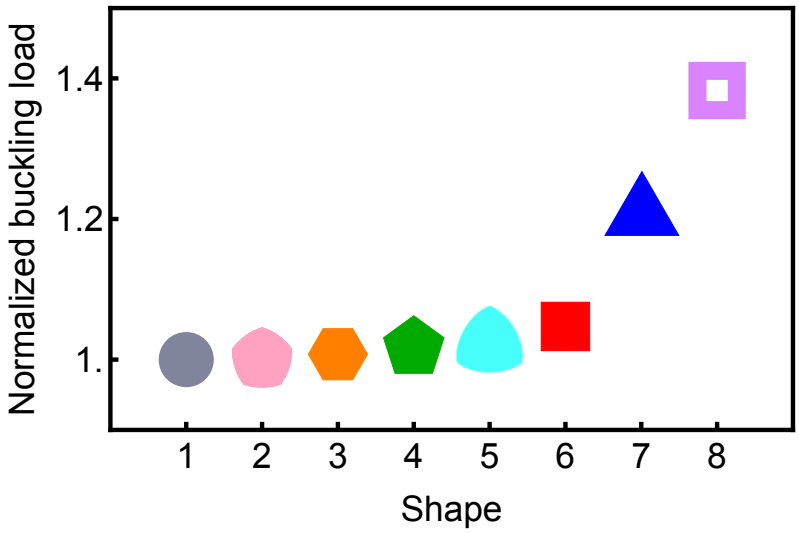

Figure 7.1. **Non-circular column cross-sections.** Comparison of critical buckling loads for columns with different cross-sectional shapes. Each column is assumed to have the same length and equal cross-sectional area. Buckling loads are normalized by the critical load of a column with circular cross section (Shape 1).

and is defined as

$$I_{xy} = \iint_R y^2 \, dx \, dy, \tag{7.2}$$

when the reference axis is the x-axis and where R is the domain of the shape. Thus, I is generally dependent on the chosen reference axis. The value of I used in equation (7.1) is the minimum I calculated for all possible axes that pass through the centroid of the cross section, as this identifies the weakest axis along which the column will buckle. One property of regular polygons is that I is equal for any axis that passes through the centroids, and thus a triangular column, for example, is equally likely to buckle in any direction.

In order to realize the increased buckling load of a polygonal cross section over a circular cross section, the overall radius of the cross section must be increased. Here, we define the radius of the cross section to be the radius of the smallest circle that circumscribes it. In Fig. 7.2, we show how P_{crit} scales for columns with cross sections of different geometries that are constrained to fit within a circle of variable radius. For each shape, there exists a limited range in the radius variable for which a column with the given cross section is both stronger than a column with a circular cross section of unit radius and for which the area of the shape does not exceed that of the circle. The latter is marked by the right end point of the curves in Fig. 7.2.

Perhaps the reason it was not appreciated until the 20th century that circular columns were suboptimal in regards to maximizing the buckling load was the appealing correspondence between the symmetry of the loading forces and the infinite rotational symmetry of a circular cross section [**42, 176**]. Indeed, there is a counter-intuitive nature to strengthening the column through progressively breaking the rotational symmetry of the cross sectional shape, as illustrated in Fig. 7.1. However, this phenomenon of breaking the symmetry of the system structure to preserve the symmetric state of the system is a recently recognized phenomenon deemed asymmetry-induced symmetry (AIS), first demonstrated in oscillator networks [**33, 34, 36, 35**]. Here, we extend the notion of AIS to the scenario of postponing a spontaneous symmetry breaking event by breaking part of the system symmetry up-front. Here, we do so in the context of delaying the buckling instability of column (i.e., increasing the critical buckling load) by changing the column cross-section to a less symmetric shape.

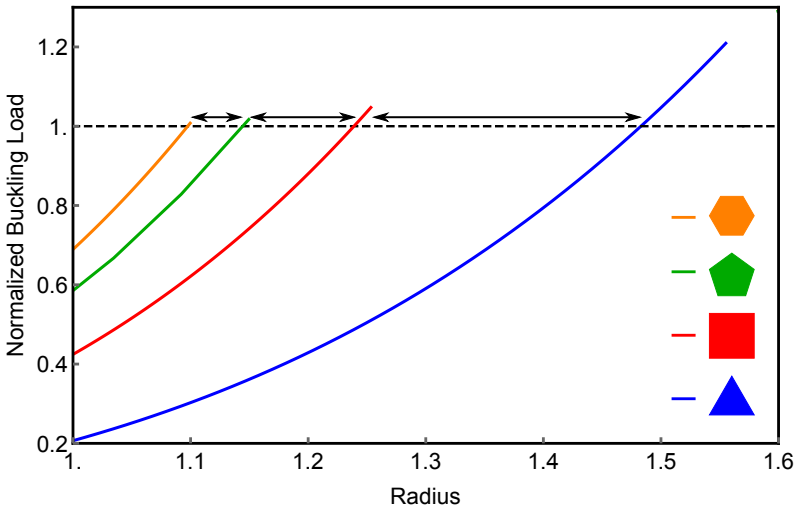

Figure 7.2. **Scaling of buckling load for columns with polygonal cross section** Buckling load of columns with cross section shapes of different regular polygons constrained to fit inside a circle of variable radius. The dashed line marks the buckling load for a column with circular cross section and unit radius. Crossing points of each curve with the dashed line indicate the radius at which columns of the respective shape have the same buckling load as the column with circular cross section. The right end points of the curves indicate the radius at which the area of the circumscribed shape is equal to the area of a circle with unit radius.

7.3. Optimized cross-sectional shapes

We present particularly striking examples of this phenomenon by considering cross-sectional shapes that maximize P_{crit}, but which are constrained to have maximum radii within the value range marked by the double-sided arrows in Fig. 7.2. Within these ranges, there exists scenarios in which a regular polygon with N or more sides may not reach a maximum radius without violating the fixed area constraint, and the area of an $(N-1)$-sided polygon with the specified radius would be smaller than the maximum allowed value. Thus, within these ranges, the optimal cross-sectional shape may not conform to a regular polygon.

We show in Fig. 7.3a such cross sections numerically optimized to maximize P_{crit}. The minimum second moment of area for each shape is larger than for any convex regular polygon constrained to have the same maximum radius. Remarkably, the minimum and maximum values of I are within $10^{-3}\%$ of each other, despite the shapes not possessing any rotational symmetry. Therefore, under these constrained conditions, cross sections of asymmetric shape stabilize unbuckled column configurations when a column of circular cross section would yield to buckling, which demonstrates a new instantiation of AIS. In Fig. 7.3b, we present the critical buckling load of each of the optimized cross sections shown in Fig. 7.3a compared with the critical loads of columns with regular polygon and (concave) six-pointed star cross sections. Concave star-shaped polygons, unlike regular polygons, do not have a maximum circumscribed radius for a fixed area. Thus, a constraint must be imposed in order to consider star-shaped polygons that maximize I, which we again choose to be a designated maximum radius. By calculating I for six-pointed stars of equal area with variable maximum radius in Fig. 7.3b, we see that, interestingly, our optimized, convex cross sections follow a similar scaling with maximum radius as the star-shaped cross sections.

7.4. Buckling instability in botanical structures

Hollow cross-sectional shapes, such as the square tube cross section in Fig. 7.1, also yield larger values of I. However, similar to the scenario of concave shapes, the maximum circumscribed radius is no longer constrained for a shape of fixed area. Simple calculations show that a thin-walled tube of large radius or an N-pointed star shape maximizes I. However, for both cases, other instabilities can make such columns fragile under bending stresses. In particular,

for hollow tubes, the Brazier instability can lead to column failure and for star-shaped cross sections the local stress at the points of the star induced by bending forces can exceed the material yield threshold. The latter arises as a result of local stresses scaling with the distance from the bending axis, and are thus amplified at the tips of a star [**180**].

While column construction is critical for engineering applications, strong columnar structures have immediate relevance in natural botanic structures. Stemmed plants undergo an array of mechanical stresses, including resisting bending stresses from wind and supporting their own weight [**180**]. Thus, important quantities for determining the structural stability of plants are the flexural rigidity, defined as EI, and the critical buckling height, which is the maximum height a column may reach before buckling under its own weight. For a column of uniform cross section, the critical buckling height, H_{crit} is proportional to $(EI/\rho g A)^{1/3}$, where ρ is the material density, g is the gravitational acceleration, and A is the cross sectional area [**181**]. We note the critical dependence of both of these structural properties on I. Increasing I allows a column to be taller and more resistant to bending forces, which are both beneficial for plants.

A particular allometric plant property studied in botany is the scaling between plant diameter and plant height [**182, 183, 184**]. The theoretical critical buckling height of a plant may be determined from its diameter (and material properties) since $(EI/\rho g A)^{1/3}$ is proportional to $(E/\rho g)^{1/3} D^{2/3}$, where D is the diameter of the convex cross section. Indeed, the scaling between plant height and diameter has been compared to the scaling predicted by H_{crit} [**181, 180**]. An interesting difference in the measurements of this scaling emerges between plants with and plants without substantial xylem tissues, which provide stronger support structures than other plant tissues [**185, 186, 187, 188**]. For woody plants (i.e., trees) the scaling between diameter and height is observed to closely follow the two-thirds law for H_{crit}. Moreover, the so-called

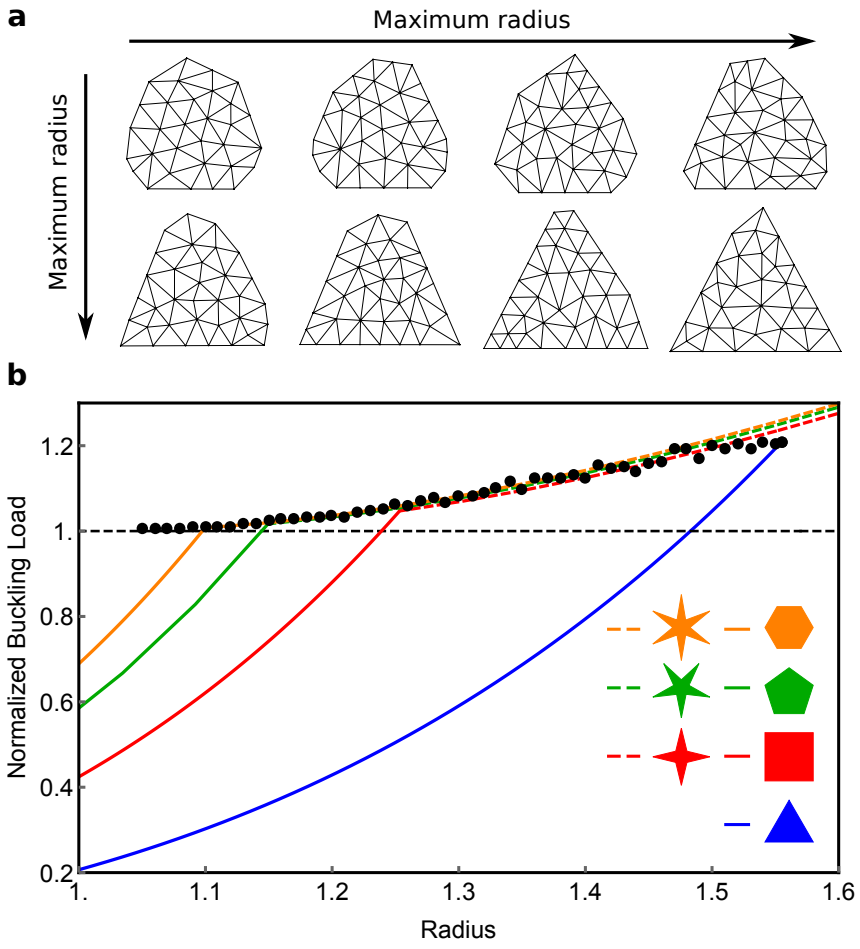

Figure 7.3. **Optimized cross-sectional shapes.** **a**, Cross-sections numerically optimized to maximize the critical buckling load of columns with equal length and material properties. All shapes have the same area, but were restricted to have different maximum radii (defined as the radius of the smallest circle that circumscribes the shape). **b**, Scaling of the critical buckling load of columns with different polygonal (solid lines), star-shaped (dashed lines), and optimized (black dots) cross sections.

safety factor (the ratio of H_{crit}/H, where H is the actual plant height), is typically near four, from which is can interpreted that, on average, trees could (in principle) be four times taller given their diameter. Thus, the buckling instability is likely not a primary mechanical failure mode for trees, which is in accordance with our common experience with trees.

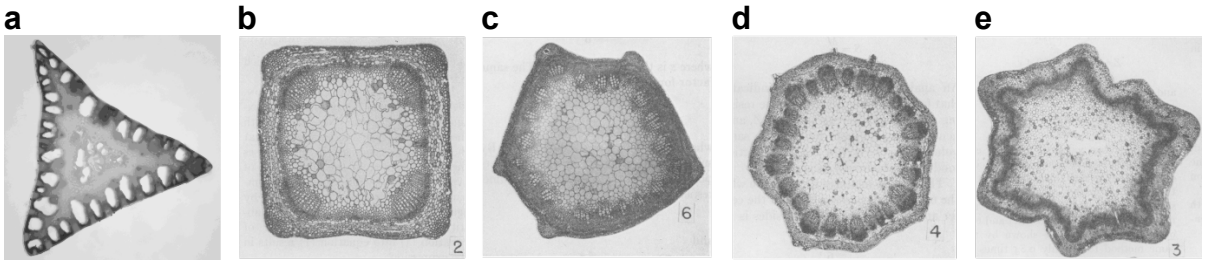

Figure 7.4. **Plant stem cross sections a-e**, Cross-sectional stem samples from *Carex pseudocyperus* (**a**), *Mentha piperita* (**b**), *Medicago sativa* (**c**), *Sericocarpus asteroides* (**d**), and *Dipsacus sylvestris* (**e**). The pictures in **b-e** are reproduced from Ref. [**189**].

On the other hand, the height of plants without substantial xylem tissues (i.e., herbaceous plants) are observed to scale with D to a power larger than two-thirds, and upperwards of four-thirds [**188**]. Therefore, the safety factor for herbaceous plants decreases with diameter and approaches (or in some cases falls below) one, which indicates that such plants approach or exceed their critical buckling height.

7.5. Numerical optimization scheme

We developed a numerical optimization scheme to determine the optimized shapes of cross-sections with constrained area and radius. During optimization, the area, maximum radius, and second moment of area were calculated for a given convex polygon. An objective function was then calculated using these quantities, and the shape of the polygon was iteratively adjusted to minimize the objective function. The specific steps of the algorithm are:

(1) Initialize m points on the boundary of a circle with radius R, and provide a maximum radius $r_{\max}$ and area $A_{\max}$.

(2) Determine the convex hull from the set of m points.

(3) Mesh the convex shape and calculate the area A, the two in-plane principal components of the second moment of area I_1 and I_2, and the radius r of the smallest circle that circumscribes the shape.

(4) Calculate the value of the objective function based on A, r, $\min(I_1, I_2)$, $r_{\max}$, and $A_{\max}$.

(5) Change the coordinates of one of the m points and repeat steps 2 through 4. If the change in coordinates reduces the objective function, keep the change, otherwise revert it.

(6) Repeat step 5 until convergence of the objective function.

The minimization of the objective function was implemented through the Nelder-Mead algorithm in Python, using the Scipy.optimize library. We chose m between 20 and 30 and R to be approximately 20% larger than $r_{\max}$. For all cases, $A_{\max}$ was set equal the the area of a circle with unit radius.

The objective function consisted of three additive components. One component was the negative of $\min(I_1, I_2)$. This ensured that optimization was performed on the smallest of the principal second moment of area components. The other two components consisted of Lennard-Jones potential functions of the form

$$\mathcal{L}(\sigma, d) = 4\epsilon\left[\left(\frac{\sigma}{2\sigma - d}\right)^{12} - 2\left(\frac{\sigma}{2\sigma - d}\right)^{6}\right]. \tag{7.3}$$

Specifically, we use $\mathcal{L}(A_{\max}, A)$ and $\mathcal{L}(r_{\max}, r)$, which are minimized at $A_{\max} = A$ and $r_{\max} = r$, respectively. Therefore, the objective function is minimized when the radius and area of the convex shape are near the maximum specified values.

7.6. Discussion

In light of this observation, it is natural to assume that plants would have evolved to be resilient against buckling and that it would be evident in their morphology. In Fig. 7.4 we show stem cross sections from several herbaceous plants, which, notably, take on various polygonal shapes. Many of these cross-sectional geometries (i.e., triangular or square) are persistent throughout species within the same family, indicating that the cross-sectional shape is an evolved trait. We posit that such cross-sections, which result in higher second moments of area than a circle, reduce the risk of buckling instabilities for plants that have dimensions for which the likelihood of self-buckling is non-negligible.

Here, we have shown a scenario in which a spontaneous symmetry breaking instability may be guarded against by systematically breaking symmetries in a system's structure. This is a surprising counter to patterns emerging in a homogenous system [**6**] and continues a recently introduced line of research (AIS) on how asymmetric properties of a system can induce symmetric dynamics among its components. One immediate application area of AIS, which we begin here, is in the study of natural system. Natural systems often exhibit robustness and stability under conditions far outside the stable ranges predicted by simple models. One reason could be that heterogeneities (sometimes referred to as noise or impurities) that are often neglected in models may serve to stabilize systems or suppress disturbances from perturbations. Here, we have examined one of the macroscopic properties of plants (i.e., the cross-sectional stem shape) and shown the potential roll of asymmetric shapes serving to stabilize plants against buckling. However, symmetries are also broken at finer scales. For example, the distribution of plant tissues within individual stems are known to effect the mechanical properties of plants and could be an immediate area of future research on this topic [**190, 191, 192**].

CHAPTER 8

Conclusions

In this thesis, we have demonstrated how nonlinearity and asymmetry may be systematically introduced into systems to induce targeted system-level behaviors. We first showed how developing built-in control mechanisms in microfluidic networks is possible by leveraging nonlinear fluid inertia effects. This approach marks a departure from the past twenty years of research in microfluidics, in which flow control was implemented via actuation from external devices or built-in flexible components. In addition, we presented a first demonstration of Braess's paradox in a fluid network, which joins the collection of previously discovered instantiations of the paradox in other classes of systems and further suggests that the paradox is a general network phenomenon. Next, we introduced a new form of levitation of heavy inertial particles in transient flows. Finally, we approached classically studied systems within the framework of asymmetry-induced symmetry and put forth new strategies of introducing physical system asymmetries that fortify against the emergence of instabilities.

An array of future lines of research naturally extend from the questions pursued here. In the context of microfluidic networks, we focused on designing networks that exhibit fundamental behaviors, such as switching and oscillations. One path forward would be to implement these dynamics into more complex networks that are capable of performing advanced processing schemes, similar to what has been done in systems that incorporate flexible valves [**21, 46**]. Alternatively, combining the nonlinear fluid inertia effects that underlie our results with nonlinear fluid-structure interactions previously exploited in microfluidics is likely to lead to entirely new

and rich flow dynamics. More generally, microfluidic networks serve as an excellent platform for investigating general network phenomena, since both the "network" is tangible (i.e., the physical structure of the flow channels) and, as we show, the degree of nonlinearity is tunable. Moreover, predictions of dynamics in microfluidic networks are amenable to experimental testing. Our demonstration of Braess's paradox exemplifies this idea and highlights how common phenomena exist across networks even when the underlying mechanisms that give rise to them are unique to particular systems.

Our work on levitation of inertial particles presents an entirely new phenomenon. Inertial particle dynamics in fluid flows have only been studied rigorously over the past thirty years, during which it has been found that surprisingly complex dynamics can emerge even in relatively simple laminar flows [**100, 101, 32**]. Thus, inertial particle advection is a young field with open questions that span the fields of fluid dynamics, nonlinear and complex systems, and chaos. Given the strong agreement between our analytic and simulation results, one natural extension of the work would be experimental verification of our predictions.

Finally, in this thesis we reframed and advanced the study of continuous systems in the context of asymmetry-induced symmetry. Given the recent establishment of this topic of research, many open questions have yet to be addressed. Primarily, a formalism or general conditions that give rise to AIS, similar to the formalism of amplitude equations for the emergence of pattern formation [**6**], has not been established. Here, we sought to broaden the class systems known to exhibit AIS to show generalizations of the phenomenon that further the establishment of such a formalism. We showed, in particular, two scenarios in which spontaneous symmetry breaking events can be delayed by reducing the symmetry of a system's structure. This is a new manifestation of AIS, with potentially far-reaching impact given the ubiquity of spontaneous symmetry

breaking phenomena across different areas of physics. Another particularly intriguing line of research is understanding to what extent AIS manifests in the robustness of natural systems, which rarely display exact symmetries.

The results and methods presented in this thesis provide a body of work in which systems are designed to exhibit properties specified *a priori*, with an emphasis on harnessing emergent dynamics. This research deviates from pursuits to understand existing systems and instead advances the effort of developing ways to build "smart" systems that remain stable or generally function in desired ways, even in the absence of central control capabilities. In this spirit, we sought to design systems with "built-in" control mechanisms. We believe the results presented here show how to take advantage of nonlinearity and asymmetry, which are often seen as design obstacles, and expect our findings to have implications for technological development in fluid and material systems.

References

[1] Strogatz, S. H. Exploring complex networks. *Nature* **410**, 268–276 (2001).

[2] Boccaletti, S., Latora, V., Moreno, Y., Chavez, M. & Hwang, D. U. Complex networks: Structure and dynamics. *Phys. Rep.* **424**, 175–308 (2006).

[3] Anderson, P. W. More is different. *Science* **177**, 393–396 (1972).

[4] Elliott, M., Golub, B. & Jackson, M. Financial Networks and Contagion. *Am. Econ. Rev.* **104**, 3115–3153 (2014).

[5] Strogatz, S. H. From Kuramoto to Crawford: Exploring the onset of synchronization in populations of coupled oscillators. *Physica D* **143**, 1–20 (2000).

[6] Cross, M. C. & Hohenberg, P. C. Pattern formation outside of equilibrium. *Rev. Mod. Phys.* **65**, 851–1112 (1993).

[7] Buldyrev, S. V., Parshani, R., Paul, G., Stanley, H. E. & Havlin, S. Catastrophic cascade of failures in interdependent networks. *Nature* **464**, 1025–1028 (2010).

[8] Yang, Y., Nishikawa, T. & Motter, A. E. Small vulnerable sets determine large network cascades in power grids. *Science* **358** (2017).

[9] Abrams, D. M. & Strogatz, S. H. Chimera states for coupled oscillators. *Phys. Rev. Lett.* **93**, 174102 (2004).

[10] Arenas, A., Díaz-Guilera, A., Kurths, J., Moreno, Y. & Zhou, C. Synchronization in complex networks. *Phys. Rep.* **469**, 93–153 (2008).

[11] Squires, T. M. & Quake, S. R. Microfluidics: Fluid physics at the nanoliter scale. *Rev. Mod. Phys.* **77**, 977–1026 (2005).

[12] Batchelor, C. K. & Batchelor, G. *An introduction to fluid dynamics* (Cambridge university press, 2000).

[13] Whitesides, G. M. The origins and the future of microfluidics. *Nature* **442**, 368–373 (2006).

[14] Mosadegh, B. *et al.* Integrated elastomeric components for autonomous regulation of sequential and oscillatory flow switching in microfluidic devices. *Nat. Phys.* **6**, 433–437 (2010).

[15] Volpatti, L. R. & Yetisen, A. K. Commercialization of microfluidic devices. *Trends Biotechnol.* **32**, 347–350 (2014).

[16] Sackmann, E. K., Fulton, A. L. & Beebe, D. J. The present and future role of microfluidics in biomedical research. *Nature* **507**, 181–189 (2014).

[17] Oh, K. W., Lee, K., Ahn, B. & Furlani, E. P. Design of pressure-driven microfluidic networks using electric circuit analogy. *Lab Chip* **12**, 515–545 (2012).

[18] Perdigones, F., Luque, A. & Quero, J. M. Correspondence between electronics and fluids in MEMS: Designing microfluidic systems using electronics. *IEEE Ind. Electron. Mag.* **8**, 6–17 (2014).

[19] Stone, H. A. Microfluidics: Tuned-in flow control. *Nat. Phys.* **5**, 178–179 (2009).

[20] Unger, M. A., Chou, H.-P., Thorsen, T., Scherer, A. & Quake, S. R. Monolithic microfabricated valves and pumps by multilayer soft lithography. *Science* **288**, 113–117 (2000).

[21] Thorsen, T., Maerkl, S. J. & Quake, S. R. Microfluidic large-scale integration. *Science* **298**, 580–584 (2002).

[22] Leslie, D. C. *et al.* Frequency-specific flow control in microfluidic circuits with passive elastomeric features. *Nat. Phys.* **5**, 231–235 (2009).

[23] Seker, E. *et al.* Nonlinear pressure-flow relationships for passive microfluidic valves. *Lab Chip* **9**, 2691–2697 (2009).

[24] Braess, D. Über ein Paradoxon aus der Verkehrsplanung. *Unternehmensforschung* **12**, 258–268 (1968).

[25] Braess, D., Nagurney, A. & Wakolbinger, T. On a paradox of traffic planning. *Transp. Sci.* **39**, 446–450 (2005).

[26] Cohen, J. E. & Horowitz, P. Paradoxical behavior of mechanical and electrical networks. *Nature* **352**, 699–701 (1991).

[27] Youn, H., Gastner, M. T. & Jeong, H. Price of anarchy in transportation networks: Efficiency and optimality control. *Phys. Rev. Lett.* **101**, 128701 (2008).

[28] Nicolaou, Z. G. & Motter, A. E. Mechanical metamaterials with negative compressibility transitions. *Nat. Mater.* **11**, 608–613 (2012).

[29] Pala, M. G. *et al.* Transport inefficiency in branched-out mesoscopic networks: An analog of the Braess paradox. *Phys. Rev. Lett.* **108**, 076802 (2012).

[30] Calvert, B. & Keady, G. Braess's paradox and power-law nonlinearities in networks. *J. Aust. Math. Soc. Ser. B* **35**, 1–22 (1993).

[31] Ayala H., L. F. & Blumsack, S. The Braess paradox and its impact on natural-gas-network performance. *Soc. Pet. Eng.* **2**, 52–64 (2013).

[32] Aref, H. *et al.* Frontiers of chaotic advection. *Rev. Mod. Phys.* **89**, 025007 (2017).

[33] Nishikawa, T. & Motter, A. E. Symmetric States Requiring System Asymmetry. *Phys. Rev. Lett.* **117**, 114101 (2016).

[34] Zhang, Y. & Motter, A. E. Identical synchronization of nonidentical oscillators: when only birds of different feathers flock together. *Nonlinearity* **31**, R1 (2018).

[35] Hart, J. D., Zhang, Y., Roy, R. & Motter, A. E. Topological Control of Synchronization Patterns: Trading Symmetry for Stability. *Phys. Rev. Lett.* **122**, 58301 (2019).

[36] Nicolaou, Z. G., Eroglu, D. & Motter, A. E. Multifaceted Dynamics of Janus Oscillator Networks. *Phys. Rev. X* **9**, 11017 (2019).

[37] Landau, L. On the theory of phase transitions. *Zh Eksp Teor Fiz* **7**, 19–32 (1937).

[38] Pearson, J. R. On convection cells induced by surface tension. *J. Fluid Mech.* **4**, 489–500 (1958).

[39] Bernstein, J. Spontaneous symmetry breaking, gauge theories, the Higgs mechanism and all that. *Rev. Mod. Phys.* **46**, 7–48 (1974).

[40] Faraday, M. Xvii. on a peculiar class of acoustical figures; and on certain forms assumed by groups of particles upon vibrating elastic surfaces. *Phil. Trans. R. Soc. London* 299–340 (1831).

[41] Benjamin, T. B. & Ursell, F. J. The stability of the plane free surface of a liquid in vertical periodic motion. *Proc. R. Soc. London Ser. A* **225**, 505–515 (1954).

[42] Keller, J. B. The shape of the strongest column. *Arch. Ration. Mech. Anal.* **5**, 275–285 (1960).

[43] Cox, S. J. The shape of the ideal column. *Math. Intell.* **14**, 16–24 (1992).

[44] Case, D. J., Liu, Y., Kiss, I. Z., Angilella, J.-R. & Motter, A. E. Braess's paradox and programmable behavior in microfluidic networks. *Nature* (accepted).

[45] Pennathur, S. Flow control in microfluidics: are the workhorse flows adequate? *Lab Chip* **8**, 383–387 (2008).

[46] Geertz, M., Shore, D. & Maerkl, S. J. Massively parallel measurements of molecular interaction kinetics on a microfluidic platform. *Proc. Natl. Acad. Sci. U.S.A.* **109**, 16540–16545 (2012).

[47] Weaver, J. A., Melin, J., Stark, D., Quake, S. R. & Horowitz, M. A. Static control logic for microfluidic devices using pressure-gain valves. *Nat. Phys.* **6**, 218–223 (2010).

[48] Tanyeri, M., Ranka, M., Sittipolkul, N. & Schroeder, C. M. Microfluidic Wheatstone bridge for rapid sample analysis. *Lab Chip* **11**, 4181–4186 (2011).

[49] Kim, S.-J., Lai, D., Park, J. Y., Yokokawa, R. & Takayama, S. Microfluidic automation using elastomeric valves and droplets: Reducing reliance on external controllers. *Small* **8**, 2925–2934 (2012).

[50] Li, L., Mo, J. & Li, Z. Nanofluidic diode for simple fluids without moving parts. *Phys. Rev. Lett.* **115**, 134503 (2015).

[51] Chin, C. D., Linder, V. & Sia, S. K. Commercialization of microfluidic point-of-care diagnostic devices. *Lab Chip* **12**, 2118–2134 (2012).

[52] Araci, I. E., Su, B., Quake, S. R. & Mandel, Y. An implantable microfluidic device for self-monitoring of intraocular pressure. *Nat. Med.* **20**, 1074–1079 (2014).

[53] Bhatia, S. N. & Ingber, D. E. Microfluidic organs-on-chips. *Nat. Biotechnol.* **32**, 760–772 (2014).

[54] Duncan, P. N., Nguyen, T. V. & Hui, E. E. Pneumatic oscillator circuits for timing and control of integrated microfluidics. *Proc. Natl. Acad. Sci. U.S.A.* **110**, 18104–18109 (2013).

[55] Duncan, P. N., Ahrar, S. & Hui, E. E. Scaling of pneumatic digital logic circuits. *Lab Chip* **15**, 1360–1365 (2015).

[56] Doh, I. & Cho, Y.-H. Passive flow-rate regulators using pressure-dependent autonomous deflection of parallel membrane valves. *Lab Chip* **9**, 2070–2075 (2009).

[57] Collino, R. R. *et al.* Flow switching in microfluidic networks using passive features and frequency tuning. *Lab Chip* **13**, 3668–3674 (2013).

[58] Stroock, A. D. *et al.* Chaotic mixer for microchannels. *Science* **295**, 647–651 (2002).

[59] Amini, H., Lee, W. & Di Carlo, D. Inertial microfluidic physics. *Lab Chip* **14**, 2739–2761 (2014).

[60] Zhang, J. *et al.* Fundamentals and applications of inertial microfluidics: a review. *Lab Chip* **16**, 10–34 (2016).

[61] Tesař, V. & Bandalusena, H. C. H. Bistable diverter valve in microfluidics. *Exp. Fluids* **50**, 1225–1233 (2011).

[62] Amini, H. *et al.* Engineering fluid flow using sequenced microstructures. *Nat. Commun.* **4**, 1826 (2013).

[63] Sudarsan, A. P. & Ugaz, V. M. Multivortex micromixing. *Proc. Natl. Acad. Sci. U.S.A.* **103**, 7228–7233 (2006).

[64] Di Carlo, D., Edd, J. F., Humphry, K. J., Stone, H. A. & Toner, M. Particle segregation and dynamics in confined flows. *Phys. Rev. Lett.* **102**, 094503 (2009).

[65] Wang, X. & Papautsky, I. Size-based microfluidic multimodal microparticle sorter. *Lab Chip* **15**, 1350–1359 (2015).

[66] Xia, H. M. *et al.* Analyzing the transition pressure and viscosity limit of a hydroelastic microfluidic oscillator. *Appl. Phys. Lett.* **104**, 024101 (2014).

[67] Zeitoun, R. I., Langelier, S. M. & Gill, R. T. Implications of variable fluid resistance caused by start-up flow in microfluidic networks. *Microfluid. Nanofluidics* **16**, 473–482 (2014).

[68] Zovatto, L. & Pedrizzetti, G. Flow about a circular cylinder between parallel walls. *J. Fluid Mech.* **440**, 1–25 (2001).

[69] Rojas, S. & Koplik, J. Nonlinear flow in porous media. *Phys. Rev. E* **58**, 4776–4782 (1998).

[70] Andrade Jr., J. S., Costa, U. M. S., Almeida, M. P., Makse, H. A. & Stanley, H. E. Inertial effects on fluid flow through disordered porous media. *Phys. Rev. Lett.* **82**, 5249–5252 (1999).

[71] Fourar, M., Radilla, G., Lenormand, R. & Moyne, C. On the non-linear behavior of a laminar single-phase flow through two and three-dimensional porous media. *Adv. Water Resour.* **27**, 669–677 (2004).

[72] Amstad, E., Datta, S. S. & Weitz, D. A. The microfluidic post-array device: high throughput production of single emulsion drops. *Lab Chip* **14**, 705–709 (2014).

[73] Haudin, F., Callewaert, M., De Malsche, W. & De Wit, A. Influence of nonideal mixing properties on viscous fingering in micropillar array columns. *Phys. Rev. Fluids* **1**, 074001 (2016).

[74] Zhao, H., Liu, Z., Zhang, C., Guan, N. & Zhao, H. Pressure drop and friction factor of a rectangular channel with staggered mini pin fins of different shapes. *Exp. Therm. Fluid Sci.* **71**, 57–69 (2016).

[75] Adams, M. L., Johnston, M. L., Scherer, A. & Quake, S. R. Polydimethylsiloxane based microfluidic diode. *J. Micromech. Microeng.* **15**, 1517–1521 (2005).

[76] Penchina, C. M. Braess's paradox and power-law nonlinearities in five-arc and six-arc two-terminal networks. *Open Transp. J.* **3**, 8–14 (2009).

[77] Motter, A. E. & Timme, M. Antagonistic Phenomena in Network Dynamics. *Annu. Rev. Condens. Matter Phys.* **9**, 463–484 (2018).

[78] Crane. *Flow of fluids through valves, fittings, and pipe: Technical paper No. 410* (Crane Co., 2010).

[79] Khodaparast, S., Borhani, N. & Thome, J. R. Sudden expansions in circular microchannels: flow dynamics and pressure drop. *Microfluid. Nanofluidics* **17**, 561–572 (2014).

[80] Gervais, T., El-ali, J., Gunther, A. & Jensen, K. F. Flow-induced deformation of shallow microfluidic channels. *Lab Chip* **6**, 500–507 (2006).

[81] Christov, I. C., Cognet, V., Shidhore, T. C. & Stone, H. A. Flow rate – pressure drop relation for deformable shallow microfluidic channels. *J. Fluid Mech.* **841**, 267–286 (2018).

[82] Bhargava, K. C., Thompson, B. & Malmstadt, N. Discrete elements for 3D microfluidics. *Proc. Natl. Acad. Sci. U.S.A.* **111**, 15013–15018 (2014).

[83] McKenna, B. K., Evans, J. G., Cheung, M. C. & Ehrlich, D. J. A parallel microfluidic flow cytometer for high-content screening. *Nat. Methods* **8**, 401–403 (2011).

[84] Katsikis, G., Cybulski, J. S. & Prakash, M. Synchronous universal droplet logic and control. *Nat. Phys.* **11**, 588–596 (2015).

[85] Stoecklein, D. & Di Carlo, D. Nonlinear Microfluidics. *Anal. Chem.* **91**, 296–314 (2019).

[86] Chen, K. K., Rowley, C. W. & Stone, H. A. Vortex dynamics in a pipe T-junction: Recirculation and sensitivity. *Phys. Fluids* **27**, 034107 (2015).

[87] Rafeie, M., Zhang, J., Asadnia, M., Li, W. & Warkiani, M. E. Multiplexing slanted spiral microchannels for ultra-fast blood plasma separation. *Lab Chip* **16**, 2791–2802 (2016).

[88] Bottausci, F., Cardonne, C., Meinhart, C. & Mezić, I. An ultrashort mixing length micromixer: The shear superposition micromixer. *Lab Chip* **7**, 396–398 (2007).

[89] Haward, S. J. *et al.* Tricritical spiral vortex instability in cross-slot flow. *Phys. Rev. E* **93**, 031101 (2016).

[90] Rhee, M. & Burns, M. A. Microfluidic pneumatic logic circuits and digital pneumatic microprocessors for integrated microfluidic systems. *Lab Chip* **9**, 3131–3143 (2009).

[91] Xia, H. M., Wu, J. W. & Wang, Z. P. The negative-differential-resistance (NDR) mechanism of a hydroelastic microfluidic oscillator. *J. Micromech. Microeng.* **27**, 075001 (2017).

[92] Gomez, M., Moulton, D. E. & Vella, D. Passive control of viscous flow via elastic snap-through. *Phys. Rev. Lett.* **119**, 144502 (2017).

[93] Khelfaoui, R., Colin, S., Orieux, S., Caen, R. & Baldas, L. Numerical and experimental analysis of monostable mini- and micro-oscillators. *Heat Transf. Eng.* **30**, 121–129 (2009).

[94] Storey, B. D., Hellen, D. V., Karst, N. J. & Geddes, J. B. Observations of spontaneous oscillations in simple two-fluid networks. *Phys. Rev. E* **91**, 023004 (2015).

[95] Van der Pol, B. On relaxation-oscillations. *Phil. Mag.* **2**, 978–992 (1926).

[96] Koper, M. T. M. Some simple bifurcations sets of an extended Van der Pol-type model and their relation to chemical oscillators. *J. Chem. Phys.* **102**, 5278–5287 (1995).

[97] Anbari, A. *et al.* Microfluidic model porous media: fabrication and applications. *Small* **14**, 1703575 (2018).

[98] Rabbani, H. S. *et al.* Suppressing viscous fingering in structured porous media. *Proc. Natl. Acad. Sci. U.S.A.* **115**, 4833–4838 (2018).

[99] Dhar, M. *et al.* Functional profiling of circulating tumor cells with an integrated vortex capture and single-cell protease activity assay. *Proc. Natl. Acad. Sci. U.S.A.* **115**, 9986–9991 (2018).

[100] Karolyi, G., Pentek, A., Scheuring, I., Tel, T. & Toroczkai, Z. Chaotic flow: The physics of species coexistence. *Proc. Natl. Acad. Sci. U.S.A.* **97**, 13661–13665 (2000).

[101] Benczik, I. J., Toroczkai, Z. & Tél, T. Advection of finite-size particles in open flows. *Phys. Rev. E* **67**, 036303 (2003).

[102] Gilpin, W. Cryptographic hashing using chaotic hydrodynamics. *Proc. Natl. Acad. Sci. U.S.A.* **115**, 4869–4874 (2018).

[103] Chen, D., Desmond, K. W. & Weeks, E. R. Experimental observation of local rearrangements in dense quasi-two-dimensional emulsion flow. *Phys. Rev. E* **91**, 062306 (2015).

[104] Desmond, K. W. & Weeks, E. R. Measurement of Stress Redistribution in Flowing Emulsions. *Phys. Rev. Lett.* **115**, 098302 (2015).

[105] Marchetti, M. C. *et al.* Hydrodynamics of soft active matter. *Rev. Mod. Phys.* **85**, 1143–1189 (2013).

[106] Woodhouse, F. G. & Dunkel, J. Active matter logic for autonomous microfluidics. *Nat. Commun.* **8**, 15169 (2017).

[107] Han, M., Whitmer, J. K. & Luijten, E. Dynamics and structure of colloidal aggregates under microchannel flow. *Soft Matter* **15**, 744–751 (2019).

[108] Shin, S., Ault, J. T., Warren, P. B. & Stone, H. A. Accumulation of colloidal particles in flow junctions induced by fluid flow and diffusiophoresis. *Phys. Rev. X* **7**, 041038 (2017).

[109] Angilella, J.-R., Case, D. J. & Motter, A. E. Levitation of heavy particles against gravity in asymptotically downward flows. *Chaos* **27**, 031103 (2017).

[110] Thiel, M., Kurths, J., Romano, M. C., Károlyi, G. & Moura, A. *Nonlinear dynamics and chaos: advances and perspectives* (Springer, 2010).

[111] Volk, R. *et al.* Acceleration of heavy and light particles in turbulence: comparison between experiments and direct numerical simulations. *Physica D* **237**, 2084–2089 (2008).

[112] Ouellette, N. T., O'Malley, P. & Gollub, J. P. Transport of finite-sized particles in chaotic flow. *Phys. Rev. Lett.* **101**, 174504 (2008).

[113] Pushkin, D., Melnikov, D. & Shevtsova, V. Ordering of small particles in one-dimensional coherent structures by time-periodic flows. *Phys. Rev. Lett.* **106**, 234501 (2011).

[114] Maxey, M. The motion of small spherical particles in a cellular flow field. *Phys. Fluids* **30**, 1915–1928 (1987).

[115] McLaughlin, J. B. Particle size effects on lagrangian turbulence. *Phys. Fluids* **31**, 2544–2553 (1988).

[116] Squires, K. D. & Eaton, J. K. Preferential concentration of particles by turbulence. *Phys. Fluids A* **3**, 1169–1178 (1991).

[117] Wang, L.-P., Maxey, M., Burton, T. & Stock, D. Chaotic dynamics of particle dispersion in fluids. *Phys. Fluids A* **4**, 1789–1804 (1992).

[118] Nishikawa, T., Toroczkai, Z., Grebogi, C. & Tél, T. Finite-size effects on active chaotic advection. *Phys. Rev. E* **65**, 026216 (2002).

[119] IJzermans, R. H. & Hagmeijer, R. Accumulation of heavy particles in n-vortex flow on a disk. *Phys. Fluids* **18**, 063601 (2006).

[120] Zahnow, J. C. & Feudel, U. Moving finite-size particles in a flow: A physical example of pitchfork bifurcations of tori. *Phys. Rev. E* **77**, 026215 (2008).

[121] Angilella, J.-R. Dust trapping in vortex pairs. *Physica D Nonlin. Phenom.* **239**, 1789–1797 (2010).

[122] Sapsis, T. & Haller, G. Clustering criterion for inertial particles in two-dimensional time-periodic and three-dimensional steady flows. *Chaos* **20**, 017515 (2010).

[123] Ravichandran, S., Perlekar, P. & Govindarajan, R. Attracting fixed points for heavy particles in the vicinity of a vortex pair. *Phys. Fluids* **26**, 013303 (2014).

[124] Nizkaya, T., Angilella, J.-R. & Buès, M. Note on dust trapping in point vortex pairs with unequal strengths. *Phys. Fluids* **22**, 113301 (2010).

[125] Benczik, I., Toroczkai, Z. & Tél, T. Selective sensitivity of open chaotic flows on inertial tracer advection: Catching particles with a stick. *Phys. Rev. Lett.* **89**, 164501 (2002).

[126] Benczik, I. J., Toroczkai, Z. & Tél, T. Advection of finite-size particles in open flows. *Phys. Rev. E* **67**, 036303 (2003).

[127] Vilela, R. D. & Motter, A. E. Can aerosols be trapped in open flows? *Phys. Rev. Lett.* **99**, 264101 (2007).

[128] Haller, G. & Sapsis, T. Where do inertial particles go in fluid flows? *Physica D* **237**, 573–583 (2008).

[129] Angilella, J.-R., Vilela, R. D. & Motter, A. E. Inertial particle trapping in an open vortical flow. *J. Fluid Mech.* **744**, 183–216 (2014).

[130] Annamalai, P., Subramanian, R. & Cole, R. Bubble migration in a rotating, liquid-filled sphere. *Phys. Fluids* **25**, 1121–1126 (1982).

[131] Annamalai, P. & Cole, R. Particle migration in rotating liquids. *Phys. Fluids* **29**, 647–649 (1986).

[132] Satti, J. & Peng, J. Leapfrogging of two thick-cored vortex rings. *Fluid Dyn. Res.* **45**, 035503 (2013).

[133] Lim, T. A note on the leapfrogging between two coaxial vortex rings at low reynolds numbers. *Phys. Fluids* **9**, 239–241 (1997).

[134] Aref, H. & Kambe, T. Report on the iutam symposium: fundamental aspects of vortex motion. *J. Fluid Mech.* **190**, 571–595 (1988).

[135] Yamada, H. & Matsui, T. Mutual slip-through of a pair of vortex rings. *Phys. Fluids* **22**, 1245–1249 (1979).

[136] Yamada, H. & Matsui, T. Preliminary study of mutual slip-through of a pair of vortices. *Phys. Fluids* **21**, 292–294 (1978).

[137] Meleshko, V., Konstantinov, M. Y., Gurzhi, A. & Konovaljuk, T. Advection of a vortex pair atmosphere in a velocity field of point vortices. *Phys. Fluids A* **4**, 2779–2797 (1992).

[138] Péntek, A., Tél, T. & Toroczkai, T. Chaotic advection in the velocity field of leapfrogging vortex pairs. *J. Phys. A* **28**, 2191 (1995).

[139] Govindarajan, R., Leonard, A. & Wiggins, S. *Lecture Notes in Physics* (Springer, 1998).

[140] Muralidharan, S., Sreenivas, K. & Govindarajan, R. Dynamical systems model of entrainment due to coherent structures. *Phys. Rev. E* **72**, 046308 (2005).

[141] Ottino, J. M. & Ottino, J. *The kinematics of mixing: stretching, chaos, and transport*, vol. 3 (Cambridge university press, 1989).

[142] Angilella, J.-R. Asymptotic properties of wall-induced chaotic mixing in point vortex pairs. *Phys. Fluids* **23**, 113602 (2011).

[143] Clift, R., Grace, J. R. & Weber, M. E. *Bubbles, drops, and particles* (Courier Corporation, 2005).

[144] Maxey, M. The gravitational settling of aerosol particles in homogeneous turbulence and random flow fields. *J. Fluid Mech.* **174**, 441–465 (1987).

[145] Stommel, H. Trajectories of small bodies sinking slowly through convection cells. *J. Mar. Res.* **8**, 24–29 (1949).

[146] Gelfreich, V. G. Melnikov method and exponentially small splitting of separatrices. *Physica D* **101**, 227–248 (1997).

[147] Chirikov, B. V. A universal instability of many-dimensional oscillator systems. *Phys. Rep.* **52**, 263–379 (1979).

[148] Kuznetsov, L. & Zaslavsky, G. M. Hidden renormalization group for the near-separatrix hamiltonian dynamics. *Phys. Rep.* **288**, 457–485 (1997).

[149] Acheson, D. Instability of vortex leapfrogging. *Euro. J. Phys.* **21**, 269 (2000).

[150] OpenFOAM. URL `http://openfoam.org`.

[151] Dickman, R. Rain, power laws, and advection. *Phys. Rev. Lett.* **90**, 108701 (2003).

[152] Iafrati, A., Babanin, A. & Onorato, M. Modulational instability, wave breaking, and formation of large-scale dipoles in the atmosphere. *Phys. Rev. Lett.* **110**, 184504 (2013).

[153] Kogan, Y. L., Mechem, D. B. & Choi, K. Effects of sea-salt aerosols on precipitation in simulations of shallow cumulus. *J. Atmos. Sci.* **69**, 463–483 (2012).

[154] Williams, J., Metje, N., Coates, L. & Atkins, P. Sand suspension by vortex pairing. *Geophys. Res. Lett.* **34** (2007).

[155] Escauriaza, C. & Sotiropoulos, F. Lagrangian model of bed-load transport in turbulent junction flows. *J. Fluid Mech.* **666**, 36–76 (2011).

[156] François, G. & P.-T., B. Fluid dynamic instabilities: theory and application to pattern forming in complex media. *Philos. Trans. R. Soc. A Math. Phys. Eng. Sci.* **375**, 20160155 (2017).

[157] Lagendijk, A., Van Tiggelen, B. & Wiersma, D. S. Fifty years of anderson localization. *Phys. Today* **62**, 24–29 (2009).

[158] Gavrielides, A., Kottos, T., Kovanis, V. & Tsironis, G. P. Spatiotemporal organization of coupled nonlinear pendula through impurities. *Phys. Rev. E* **58**, 5529–5534 (1998).

[159] Alexeeva, N. V., Barashenkov, I. V. & Tsironis, G. P. Impurity-induced stabilization of solitons in arrays of parametrically driven nonlinear oscillators. *Phys. Rev. Lett.* **84**, 3053–3056 (2000).

[160] Braiman, Y., Lindner, J. F. & Ditto, W. L. Taming spatiotemporal chaos with disorder. *Nature* **378**, 465–467 (1995).

[161] Huepe, C., Ding, Y., Umbanhowar, P. & Silber, M. Forcing function control of Faraday wave instabilities in viscous shallow fluids. *Phys. Rev. E* **73**, 016310 (2006).

[162] Howard, L. N. & Yu, J. Normal modes of a rectangular tank with corrugated bottom. *J. Fluid Mech.* **593**, 209–234 (2007).

[163] Weidman, P. D., Herczynski, A., Yu, J. & Howard, L. N. Experiments on standing waves in a rectangular tank with a corrugated bed. *J. Fluid Mech.* **777**, 122–150 (2015).

[164] Feng, J., Jacobi, I. & Stone, H. A. Experimental investigation of the faraday instability on a patterned surface. *Exp. Fluids* **57**, 86 (2016).

[165] Urra, H. *et al.* Localized faraday patterns under heterogeneous parametric excitation. *Phys. Rev. E* **99**, 033115 (2019).

[166] Wilczek, F. Quantum time crystals. *Phys. Rev. Lett.* **109**, 160401 (2012).

[167] Yao, N. Y., Nayak, C., Balents, L. & Zaletel, M. P. Classical discrete time crystals. *arXiv preprint arXiv:1801.02628* (2018).

[168] Chen, W., Lin, W. & Zhu, Y. Onset instability of a parametrically excited pendulum array. *Phys. Rev. E* **75**, 016606 (2007).

[169] Osipov, V. & García, N. Space-time parametric excitation of localized standing waves on a surface of a fluid in a vessel with corrugated bottom. *Phys. Lett. A* **283**, 209–215 (2001).

[170] Nash, L. M. *et al.* Topological mechanics of gyroscopic metamaterials. *Proc. Natl. Acad. Sci. U.S.A.* **112**, 14495–14500 (2015).

[171] Ponedel, B. C. & Knobloch, E. Forced snaking: Localized structures in the real ginzburg-landau equation with spatially periodic parametric forcing. *Euro. Phys. J. Spec. Top.* **225**, 2549–2561 (2016).

[172] Mitchell, N. P., Nash, L. M., Hexner, D., Turner, A. M. & Irvine, W. T. Amorphous topological insulators constructed from random point sets. *Nat. Phys.* **14**, 380 (2018).

[173] Kumar, K. & Tuckerman, L. S. Parametric instability of the interface between two fluids. *J. Fluid Mech.* **279**, 49–68 (1994).

[174] Douady, S. & Fauve, S. Pattern selection in faraday instability. *Europhys. Lett.* **6**, 221 (1988).

[175] Douady, S. Experimental study of the faraday instability. *J. Fluid Mech.* **221**, 383–409 (1990).

[176] Cox, S. J. & Overton, M. L. On the optimal design of columns against buckling. *SIAM J. Math. Anal.* **23**, 287–325 (1992).

[177] Olhoff, N. & Rasmussen, S. H. On single and bimodal optimum buckling loads of clamped columns. *Int. J. Solids Struct.* **13**, 605–614 (1977).

[178] Kirmser, P. G. & Hu, K. K. The shape of the ideal column reconsidered. *Math. Intell.* **15**, 62–67 (1993).

[179] Seyranian, A. P. & Privalova, O. G. The Lagrange problem on an optimal column: Old and new results. *Struct. Multidiscip. Optim.* **25**, 393–410 (2003).

[180] Niklas, K. J. *Plant biomechanics: an engineering approach to plant form and function* (University of Chicago press, 1992).

[181] McMahon, T. Size and shape in biology: elastic criteria impose limits on biological proportions, and consequently on metabolic rates. *Science* **179**, 1201–1204 (1973).

[182] Niklas, K. J. & Spatz, H.-C. Methods for calculating factors of safety for plant stems. *J. Exp. Biol.* **202**, 3273–80 (1999).

[183] Jaouen, G., Alméras, T., Coutand, C. & Fournier, M. How to determine sapling buckling risk with only a few measurements. *Am. J. Bot.* **94**, 1583–1593 (2007).

[184] Shah, D. U., Reynolds, T. P. & Ramage, M. H. The strength of plants: Theory and experimental methods to measure the mechanical properties of stems. *J. Exp. Bot.* **68**, 4497–4516 (2017).

[185] Niklas, K. J. The scaling of plant height: a comparison among major plant clades and anatomical grades. *Ann. Bot.* **72**, 165–172 (1993).

[186] Niklas, K. J. Influence of tissue density-specific mechanical properties on the scaling of plant height. *Ann. Bot.* **72**, 173–179 (1993).

[187] Niklas, K. J. Interspecific allometries of critical bucklinng height and actual plant height. *Am. J. Bot.* **81**, 1275–1279 (1994).

[188] Niklas, K. J. The allometry of saftey-factors for plant height. *Am. J. Bot.* **81**, 345–351 (1994).

[189] Press, C. The role of mechanics in the evolution of the herbaceous plant stem. *Bot. Gaz.* **111**, 262–286 (1950).

[190] Niklas, K. J. Plant height and the properties of some herbaceous stems. *Ann. Bot.* **75**, 133–142 (1995).

[191] Schulgasser, K. & Witztum, A. On the Strength of Herbaceous Vascular Plant Stems. *Ann. Bot.* **80**, 35–44 (1997).

[192] Mannan, S., Knox, J. P. & Basu, S. Correlations between axial stiffness and microstructure of a species of bamboo. *R. Soc. Open Sci.* **4**, 160412 (2017).

[193] Geuzaine, C. & Remacle, J.-F. Gmsh: a three-dimensional finite element mesh generator with built-in pre- and post-processing facilities. *Int. J. Numer. Methods Eng.* **79**, 1309–1331 (2009).

[194] Kim, M., Huang, Y., Choi, K. & Hidrovo, C. H. The improved resistance of PDMS to pressure-induced deformation and chemical solvent swelling for microfluidic devices. *Microelectron. Eng.* **124**, 66–75 (2014).

[195] Johnston, I. D., McCluskey, D. K., Tan, C. K. L. & Tracey, M. C. Mechanical characterization of bulk sylgard 184 for microfluidics and microengineering. *J. Micromech. Microeng.* **24**, 035017 (2014).

[196] Martin, R. S., Gawron, A. J., Lunte, S. M. & Henry, C. S. Dual-electrode electrochemical detection for poly(dimethylsiloxane)-fabricated capillary electrophoresis microchips. *Anal. Chem.* **72**, 3196–3202 (2000).

[197] Duffy, D. C., McDonald, J. C., Schueller, O. J. A. & Whitesides, G. M. Rapid prototyping of microfluidic systems in poly(dimethylsiloxane). *Anal. Chem.* **70**, 4974–4984 (1998).

[198] Lachaux, J. *et al.* Thermoplastic elastomer with advanced hydrophilization and bonding performances for rapid (30 s) and easy molding of microfluidic devices. *Lab Chip* **17**, 2581–2594 (2017).

APPENDIX A

Experimental and simulation methods for determining Braess's paradox in microfluidic networks

Navier-Stokes simulations. The numerical simulations were performed using OpenFOAM-version 4.1 [**150**]. We used meshes with an average cell area ranging from $10\,\mu\text{m}^2$ to $340\,\mu\text{m}^2$, where the finer meshing was applied near the obstacles. All meshes were generated using Gmsh [**193**]. The two-dimensional solutions were found using the simpleFoam solver within OpenFOAM, employing second-order numerical schemes, where a fixed static pressure of zero was set for the boundary conditions at the outlets. At the inlets, the static (total) pressure was fixed for the static (total) pressure controlled cases. For simulations of the multiswitch network in Fig. 2.6, the same geometry and dimensions were used as for the model predictions, provided in Table 3.1, and equal driving pressures were applied at each of the six inlets.

Reynolds numbers. The characteristic length scale used in defining the Reynolds number of the flow is the hydraulic diameter of the channels, defined as $4A/P$, where A is the area and P is the perimeter of the channel cross section (common to all segments). The hydraulic diameter in two and three dimensions is $2w$ and $2wh/(w+h)$, respectively, where h is the height of the channels in the three-dimensional case. The characteristic velocity used in two and three dimension is Q/w and Q/wh, respectively. Therefore, we define $Re = 2\rho Q/\mu$ for our simulations in two dimensions and $Re = 2\rho Q/\mu(w+h)$ for our experiments in three dimensions. The undeclared

ranges of Re for the channel segment with obstacles considered in the presented data are: 21–385 (Fig. 2.3), 12–121 (Fig. 2.4), 4–111 (Fig. 2.5), 1–220 (Fig. 2.6), 1–380 (Fig. 3.2), 40–385 (Fig. 3.4), 20–400 (Fig. 3.5), 2–10 (Fig. 3.9b), 75–85 (Fig. 3.9c), 76–89 (Fig. 3.10), 10–20 (Fig. 3.12b), and 110–120 (Fig. 3.12c).

PDMS channel fabrication. The flow channels were assembled by sealing a patterned PDMS chip against a glass slide. The PDMS chip was made by pouring a mixture of PDMS oligomer and cross-linking curing agent (Sylgard 184) at a weight ratio of 10:1 into a mold after being degassed under vacuum. The mixture was cured at 74 °C for 1 h and then peeled off from the mold to yield the microchannel design. The dimensions of the channels in Figs. 2.2 and 2.4 were 200 μm (width) $\times$ 185 μm (height), and the diameter of the obstacles was 97 μm. After punching the holes for inlet and outlet connections, the PDMS chip was thermally aged at 200 °C for 12 h to reduce pressure-induced deformation [**194**], yielding a chip with a Young's modulus of approximately 3 MPa [**195**]. Both the PDMS chip and the glass substrate were cleaned with isopropanol and treated by plasma for 90 s before bringing them into contact. Once the PDMS chip was sealed against the glass slide, the device was placed in an oven for 30 min at 74 °C to improve bonding quality.

The mold used was a silicon wafer containing microchannel patterns created by soft photolithography using a negative photoresist [**196, 197**]. A 4-inch silicon wafer (test grade, University Wafer, Boston, MA) was cleaned with acetone and isopropanol and dried with nitrogen gas. The wafer was then coated with SU-8 50 negative photoresist (MicroChem Corp., Newton, MA) on a spin coater (Laurell Technologies Corp., North Wales, PA) operating at 600 rpm for 30 s. After a pre-exposure bake at 65 °C and subsequently at 95 °C, each for 60 min, the coated wafer was exposed to UV light (Autoflood 1000, Optical Associates, Milpitas, CA)

through a negative transparent photomask that contained the desired channel design. Following a post-exposure bake at $95\,°C$, the wafer was developed in SU-8 developer (MicroChem Corp., Newton, MA) for 60 min to obtain the pattern.

Flexdym channel fabrication. Flexdym (Blackholelab Inc., Paris) is a thermoplastic elastomer (Young's modulus of 1.18 MPa) with a rapid and easy molding process for microfluidic devices [**198**]. After fabrication of the silicon wafer mold containing the channel designs, a sheet of Flexdym (6 cm $\times$ 4 cm) was placed directly above the mold with another sheet of unpatterned PDMS (about 1 mm thick) placed above the Flexdym for protection. The whole set was then placed on a heat press between two Teflon sheets. The plate on the heat press was heated to $175\,°C$ before starting to mold the Flexdym. Once the target temperature was reached, the lever on the heat plate was locked down with a timer set for 5 min. After the process was finished, the lever was released and the Flexdym sheet was inspected visually to make sure that no bubbles were trapped around the channel. The chip was allowed to cool down for 5 min before unfolding the layers. The Flexdym was permanently sealed with a glass slide by following the same sealing procedure used for the PDMS channels. The dimensions of the cross-section of the channels were $201\,\mu$m (width) $\times$ $166\,\mu$m (height), and the diameter of the obstacles was $99\,\mu$m.

SU-8 photoresist channel fabrication. To make microfluidic channels directly from SU-8 photoresist, an inverse mask was designed and printed on transparency. The desired channel was printed on the inverse mask in black with transparent dots marking the obstacles, and the rest of the mask was left transparent. The same procedure to make the silicon wafer master as described in "PDMS channel fabrication" was followed to fabricate the channels on glass slides. The chip was then sealed by 3M VHB tape to another glass slide with holes for connections.

The dimensions of the cross-section of the channels were $209\,\mu$m (width) $\times$ $196\,\mu$m (height), and the diameter of the obstacles was $90\,\mu$m. The Young's modulus of SU-8 photoresist is 2 GPa (from table of properties for SU-8 permanent photoresists, MicroChem Corp., Newton, MA).

Flow rate measurement. Experimental measurements in Figs. 2.2 and 2.4 were made with the system shown in Fig. 2.4a. When measuring the relation between pressure and flow rate, the linking channel valve was closed to allow separate measurement of the channel with and the channel without obstacles. Deionized (DI) water was pumped through each channel and a pressure scan from 0 to 100 kPa was performed using an Elveflow OB1 pressure controller. The flow rate was measured by an Elveflow MFS5 flow sensor (0.2 - 5 mL/min). To verify Braess's paradox, the same instruments were used and the pressure was set constant while recording the flow rate at each outlet. Red (3 g/L, FD&C Red #40, Flavors & Colors) and blue (1.5 g/L, FD&C Blue #1, Flavors & Colors) dyes were added into DI water to demonstrate the switching behavior. The concentrations of the dyes were adjusted for similar flow rate under the same pressure. The flow rate measurements in Fig. 3.8 were performed using isolated channels constructed from Flexdym and SU-8 photoresist, respectively.

Fluorescence imaging. Fluorescent polyethylene microspheres (10-$20\,\mu$m) were suspended in Tween 80 solution (Cospheric LLC, Santa Barbara, CA) and pumped through a single microfluidic channel with obstacles by an Elveflow OB1 pressure controller. Two different pressures were applied, 3 kPa and 100 kPa, to demonstrate different flow profiles around the obstacles. Fluorescence images were captured with an Olympus BX51 microscope equipped with a NIBA filter through an Infinity 3 CCD camera.

Measured flow rate data and statistics. Savitsky-Golay filtering was applied to all flow rate data collected through experiments, using a window length of 11 data points and a second-order polynomial. For each of the fixed pressures presented in Fig. 2.4b-d, a 60 s time series of flow rate data was collected at each of the outlets with a sampling rate of 10 Hz. Over the 60 s interval, the linking channel valve was sequentially opened/closed every 15 s. For each time series, the 15 s intervals in which the valve was open (closed) were averaged to create a single 15 s time series for each outlet. The total flow rate ($Q_4 + Q_5$) was calculated when the valve is open and closed, respectively, by summing the 15 s time series for the two outlets point-by-point. The statistics presented in Fig. 2.4 are the average and standard deviation of the resulting series. For Fig. 3.10, the flow rate at each of the two outlets was measured experimentally at a sampling rate of 100 Hz over a 180 s interval, during which the linking channel was sequentially opened/closed every 30 s. The total flow rate in panel c was calculated by summing, point-by-point, the data in panels a and b.

Parameters in simulations and experiments. In the simulations, we set $\rho = 10^3\,\text{kg/m}^3$, $\mu = 10^{-3}\,\text{Pa·s}$, $\nu = \mu/\rho = 10^{-6}\,\text{m}^2\text{/s}$, $w = 500\,\mu\text{m}$ for the width of all channels, and $r = 100\,\mu\text{m}$ for the radius of all obstacles, unless otherwise noted. In all experiments, DI water was used as the working fluid. The other undeclared dimensions were as follows. In Fig. 2.2a,b, the length of the (partially shown) channel was $1.25\,\text{cm}$. In Fig. 2.2c-e, the channel length was $4.3\,\text{cm}$, and in Fig. 2.2f the channel length was $2.0\,\text{cm}$ (see PDMS channel fabrication for the remaining dimensions). In Fig. 2.3, $L_1 = 0.17\,\text{cm}$, $L_2 = 1.0\,\text{cm}$, $L_3 = 0.1\,\text{cm}$, $L_4 = 1.25\,\text{cm}$, and $L_5 = 1.0\,\text{cm}$. In Fig. 2.4, $L_1 = 0.6\,\text{cm}$, $L_2 = 2.9\,\text{cm}$, $L_4 = 1.4\,\text{cm}$, and $L_5 = 1.4\,\text{cm}$. For the linking channel, the switch valve was connected to the two parallel channels through $15\,\text{cm}$ of round tubing and $0.7\,\text{cm}$ of microchannel on each side. Each inlet was connected to the

pressurized vials through 62 cm of tubing, and each outlet was attached to 50 cm of tubing. The inner diameter of all tubing was 0.79 mm. In Fig. 2.5, $L_2 = 3.0$ cm, $L_3 = 0.1$ cm, $L_4 = 1.25$ cm, $L_5 = 1.4$ cm, and $L^* = 0.995$ cm (calculated using the value for α found in Fig. 3.6b).